ABSTRACT

Title of Dissertation: QUANTUM DOTS IN PHOTONIC CRYSTALS FOR HYBRID INTEGRATED SILICON PHOTONICS

Mohammad Habibur Rahaman
Doctor of Philosophy, 2024

Dissertation Directed by: Professor Edo Waks
Department of Electrical and Computer Engineering

Quantum dots are excellent sources of on-demand single photons and can function as stable quantum memories. Additionally, advanced fabrication techniques of III-V materials and various hybrid integration methods make quantum dots an ideal candidate for integration into fiber- and silicon-based photonic circuits. However, efficiently extracting and integrating quantum dot emissions into fiber- and silicon-based photonic circuits, particularly with high efficiency and low power consumption, presents a continued challenge. This dissertation addresses this challenge by utilizing photonic crystals to couple quantum dot emissions into fiber- and silicon-based photonic circuits.

In this dissertation, we first demonstrate an efficient fiber-coupled single photon source at the telecom C-band using InAs/InP quantum dots coupled to a nanobeam photonic crystal. The tapered nanobeam structure facilitates directional emission that is mode-matched to a lensed fiber, resulting in a collection efficiency of up to 65% from the nanobeam to a single-mode fiber. Using this approach, we demonstrate a bright single photon source with a 575 ± 5 Kcps count

rate. Additionally, we observe a single photon purity of 0.015 ± 0.03 and Hong-Ou Mandel interference from emitted photons with a visibility of 0.84 ± 0.06. A high-quality factor photonic crystal cavity is needed to further improve the brightness of the single-photon source through Purcell enhancement. However, photonic crystal cavities often suffer from low-quality factors due to fabrication imperfections that create surface states and optical absorption. To address this challenge, we employed atomic layer deposition-based surface passivation of the InP photonic crystal nanobeam cavities to improve the quality factor. We demonstrated up to 140% higher quality factors by applying a coating of Al_2O_3 via atomic layer deposition to terminate dangling bonds and reduce surface absorption. Additionally, changing the deposition thickness enabled precise tuning of the cavity mode wavelength without compromising the quality factor. This Al_2O_3 atomic layer deposition approach holds great promise for optimizing nanobeam cavities, which are well-suited for integration with a wide range of photonic applications.

Finally, we propose a hybrid Si-GaAs photonic crystal cavity design that operates at telecom wavelengths and can be fabricated without the need for careful alignment. The hybrid cavity consists of a patterned silicon waveguide that is coupled to a wider GaAs slab featuring InAs quantum dots. We show that by changing the width of the silicon cavity waveguide, we can engineer hybrid modes and control the degree of coupling to the active material in the GaAs slab. This provides the ability to tune the cavity quality factor while balancing the device's optical gain and nonlinearity. With this design, we demonstrate cavity mode confinement in the GaAs slab without directly patterning it, enabling strong interaction with the embedded quantum dots for applications such as low-power-threshold lasing and optical bistability (156 nW and 18.1 μW, respectively). In addition to classical applications, this cavity is promising for alignment-free, large-scale integration of single photon sources in a silicon chip.

QUANTUM DOTS IN PHOTONIC CRYSTALS FOR HYBRID INTEGRATED SILICON PHOTONICS

by

Mohammad Habibur Rahaman

Dissertation submitted to the Faculty of the Graduate School of the
University of Maryland, College Park in partial fulfillment
of the requirements for the degree of
Doctor of Philosophy
2024

Advisory Committee:
Professor Edo Waks, Chair/Advisor
Professor Agis Iliadis
Assistant Professor Cheng Gong
Professor Julius Goldhar
Professor Loudes Salamanca-Riba, Dean's Representative

© Copyright by
Mohammad Habibur Rahaman
2024

Dedication

To my daughter, Vaneeza Rahaman.

Acknowledgments

The completion of this thesis is indebted to my supervisor, colleagues, and my family members for their invaluable support. Firstly, I want to express my thanks to my advisor, Edo Waks, for providing me with the opportunity to undertake challenging projects within his group. His flexibility and patience were essential for me to acquire new skills, and his guidance and diverse perspectives have been instrumental in making this thesis possible.

I am also sincerely grateful to my committee members, Professors Agis Iliadis, Cheng Gong, Julius Goldhar, and Lourdes G. Salamanca-Riba, whose insights and guidance have greatly enriched my work. Additionally, I thank my collaborators, Professors Dirk Englund, Hugo Larouque, Carlos Errando-Herranz, and Dr. Mike Fanto, for their insightful discussions during joint meetings, leading to many enlightening insights.

Throughout this journey, I have closely collaborated with postdocs and doctoral students within the group, and I have enjoyed working alongside Dr. Changmin Lee, Dr. Mustafa Atabey Buyukkaya, and Sam Harper. I extend my appreciation to all members of the quantum photonics group, including Dr. Harjot Singh, Fariba Islam, Purbita Purkayastha, Yuqi Zhao, Yuxi Ziang, and Abhijit Biswas, for their friendship and support. The unwavering support of the UMD Nanocenter staff, including John Abrahams, Jonathan A. Hummel, Tom Loughran, Mark Lecates, Dr. Wen-An Chiou, and Dr. Jiancun Rao, has been indispensable in maintaining equipment performance. I am also grateful to the dedicated ECE and IREAP staff, especially Vivian Lu, Bill Churma,

Maria Hoo, Nolan Ballew, Nancy Boone, Dorothea Brosius, Meredith Pettit, Judi Gorski, and Leslie Delabar, as well as Melanie Prange and Emily Irwin, for their assistance during challenging circumstances. Special thanks are due to Alexander Brozena for her assistance in writing journals and the dissertation.

Finally, my deepest appreciation goes to my beloved wife, Sara Aktar, for her unwavering support at every moment and her patience during times of struggle. I am also grateful to my parents, siblings, and extended family for their dedicated support. Furthermore, I am indebted to my friends in College Park; life would not be easy without them. Additionally, I acknowledge the financial support from the Air Force Office of Scientific Research (AFOSR), Maryland-ARL Quantum Partnership, National Science Foundation (NSF), and U.S. Department of Defense, which made the projects discussed herein possible.

Table of Contents

Dedication ii

Acknowledgements iii

Table of Contents v

List of Tables vii

List of Figures vii

List of Abbreviations xi

Chapter 1: Introduction 1
- 1.1 Overview . . . 1
- 1.2 Photonic crystals . . . 4
- 1.3 Nanobeam photonic crystals . . . 5
- 1.4 Hybrid integration of nanobeam photonic crystals . . . 6
- 1.5 Thesis outline . . . 9

Chapter 2: Efficient, indistinguishable telecom C-band photons 10
- 2.1 Introduction . . . 10
- 2.2 Nanobeam design and fabrication . . . 11
- 2.3 Results and discussion . . . 13
- 2.4 Summary and discussion . . . 19

Chapter 3: Atomic layer deposition based surface passivation of InP nanobeam cavity 21
- 3.1 Introduction . . . 21
- 3.2 Nanobeam cavity design . . . 22
- 3.3 Nanobeam cavity fabrication . . . 24
- 3.4 Nanobeam cavity characterization . . . 26
- 3.5 Summary and discussion . . . 31

Chapter 4: Hybrid Si-GaAs photonic crystal cavity 33
- 4.1 Introduction . . . 33
- 4.2 Proposed hybrid Si-GaAs cavity design . . . 36
- 4.3 Lasing simulation . . . 39
- 4.4 Bistability simulation . . . 41

4.5 Summary and discussion 44

Chapter 5: Conclusions and future directions 45

Appendix A: 48
A.1 Tapered Nanobeam design at 1550 nm 48
A.2 Reflectance measurement 50
A.3 Lifetime calculation 50
A.4 Second-order autocorrelation using pulsed laser excitation 51
A.5 Photon budget and source efficiency 52
A.6 Hong-Ou-Mandel interferometer setup 53

Appendix B: 55
B.1 Nanobeam cavity design 55
B.2 FDTD simulation of nanobeam taper at 1300 nm 56
B.3 Coupling efficiency before and after ALD 57
B.4 Quality factor fitting equation 58
B.5 Quality factor analysis 58
B.6 Resonance wavelength change of nanobeam cavity 59
B.7 Coupled mode theory 61

Appendix C: 63
C.1 GaAs and spacer thickness selection 63
C.2 Purcell factor 64
C.3 Lasing Pump-Probe Simulation 64
C.4 Lasing rate equation 66
C.5 Bistability theory 67
C.6 Wavelength tuning of the hybrid Si-GaAs cavity 68
C.7 Lasing and bistability performance for different device dimensions 69

Appendix D: List of Publications and Conference Talks 71

Bibliography 73

List of Figures

1.1 (a) Top and (b) cross-sectional views of photonic crystals employing Bragg reflection through refractive index modulation. Here, n_1, n_2, and n_3 correspond to the refractive indices in different materials denoted in gray, blue, and light gray, respectively. 4
1.2 (a) Nanobeam photonic crystal mirror and (b) Nanobeam photonic crystal cavity. 5
1.3 Schematic representation of the transfer-printing pick-and-place technique utilizing a polydimethylsiloxane (PDMS) stamp. 8

2.1 Schematic diagram of InAs/InP quantum dots wafer. 11
2.2 (a) Schematic diagram of the top view photonic crystal mirror nanobeam with width w, length L, and taper tip width of b. Here, QD: quantum dots; LF: lensed fiber. (b) The far-field mode profile was calculated at 500 nm from the tapered nanobeam tip edge. (c) SEM image of the fabricated nanobeam arrays after PDMS stamp transfer printing. The inset shows a zoomed-in image of a nanobeam mirror. 12
2.3 (a) Schematic diagram of the optical measurement setup. LF: lensed fiber, FF: fiber filter, NB: nanobeam, HWP: half waveplate, BS: beam splitter, PBS: polarizing beam splitter, OBJ: objective lens, PM: power meter, PC: polarization controller, and SNSPD: superconducting nanowire single photon detector. (b) Time-resolved photoluminescent spectra of quantum dot emission for an above-band excitation of 780 nm at a power 5 μW. The inset shows the zoomed-in spectrum of the QD emission filtered by a 0.2 nm bandwidth tunable fiber spectral filter. Here, the blue circles show the data, and the red solid line represents the Lorentzian fits. . . 13
2.4 (a) Normalized autocorrelation histograms measured at 780 nm under above-band excitation with power levels of 350 nW and 1.5 μW. The black lines represent the measured data, while the red dashed lines depict curves fitted to the double-sided exponential decay function. (b) Detected count rates (red circles) and $g^{(2)}(0)$-corrected count rates (blue circles) as a function of the pump power. The blue line corresponds to a fit to the blue circles with fitting parameters $P_{sat} = 1.19\mu$W and $I_{sat} = 575 \pm 5$ Kcps. (c) $g^{(2)}(0)$ as a function of the pump power. 15
2.5 Two-photon interference for (a) indistinguishable photons with parallel polarization and (b) distinguishable photons with orthogonal polarization at 1.5 μW pump power using a continuous wave laser at 780 nm, with respective fit functions represented by red dashed lines. (c) A zoomed-in view of panel (a). 18

3.1 (a) The tapered nanobeam InP photonic crystal cavity design with width w, lattice parameter a, and hole radius r. The cavity region is realized by tapering and shifting 4 pairs of holes by a factor of 0.935, towards the center. NL and NR are the total number of holes (including the tapered 4 holes) on the left and right sides of the nanobeam, respectively. (b) The 3D-FDTD simulated fundamental mode profile ($|E|^2$) of the nanobeam cavity, and (c) the far-field mode profile calculated from the nanobeam taper edge with width b. The white dashed line in the far-field profile corresponds to a numerical aperture of 0.5 of the objective lens. 23
3.2 InP nanobeam cavity fabrication steps using SiN hard mask. Here, CPD: critical point drier. 24
3.3 (a, b) SEM images of an array of nanobeam cavities after (a) wet etching and (b) transfer printing. (c) Zoomed-in view of a nanobeam cavity after transfer printing and 2 nm atomic layer deposition of Al_2O_3. (d) Schematic diagram of the reflectance spectra measurement setup for the InP nanobeam cavity (NBC) array; BS: Beam splitter. 25
3.4 (a) Normalized reflectance spectra of a nanobeam cavity with NR = 7 for different thicknesses of Al_2O_3 using atomic layer deposition. The black curve, representing spectra without ALD, is blue-shifted by 1 nm to prevent overlap. (b) Average quality factors of 30 nanobeam cavities with NR = 7 for different atomic layer deposition thicknesses, with the average quality factor indicated by the red horizontal line, and (c) Average wavelength shifts from the cavity resonance wavelength. . 27
3.5 Normalized reflectance measurements spectra along with Lorentzian fits for a range cavity hole numbers of out-coupling mirror (NR) from 5 to 8 (a) Before ALD and (b) After ALD. The measurements are in blue circles, while the red dashed curve represents the Lorentzian fit. (c) the corresponding measured quality factor for the same nanobeam cavities for different NR before (blue) and after (red) atomic layer deposition (ALD) of a 6 nm coating of Al_2O_3. (d) Calculated $Q_{||}$ and $Q_{\perp}$ from Equation (1) values before (blue) and after (red) the atomic layer deposition treatment. (e) Average percentage change in the quality factor (Q) across 20 samples for NR values ranging from 5 to 8. Purple, green, and gray color schemes correspond to the respective over-coupled, critically coupled, and under-coupled regions. 30

4.1 (a) 3D schematic illustration of the Si-GaAs hybrid cavity, and (b) the corresponding 2D cross-section. (c) The transverse mode profile ($|E|$) of the hybrid mode (TE polarized) for different silicon waveguide widths (W_{Si}) of 200 nm, 580 nm, and 1200 nm at a fixed GaAs slab width of 2 μm at an incident light wavelength of 1516.53 nm. The solid white lines represent the boundaries of the silicon waveguide and GaAs slab. (d) The silicon waveguide width controls the relative confinement of the hybrid mode in the silicon waveguide and GaAs slab region, where positions I, II, and III correspond to the different silicon waveguide widths marked in (c). 35

4.2 (a) Schematic diagram of the silicon waveguide cavity design, which features a total of 16 cavity pairs, including $N = 11$ ellipsoidal cavities on both sides and 5 centered pairs of tapered ellipsoids as defects. (b) The FDTD calculated band structure of the hybrid Si-GaAs device. The grey shaded area is the photonic bandgap (PBG), which corresponds to the difference between the calculated air bands (red curves) and dielectric bands of the silicon and GaAs (blue curves marked I and II, respectively). Here, k_x is related to wavevector $k = k_x(2\pi/a)$, which is a function of the reciprocal lattice parameter a specified by the Bloch boundary condition. The black line denotes the SiO_2 light line, and the horizontal black dashed line in PBG indicates the cavity resonance frequency at 197.68 THz. (c) The fundamental mode field ($|E|$) profile in the hybrid Si-GaAs cavity obtained using the 3D FDTD method. The white dashed lines denote the silicon and GaAs layers (220 nm and 200 nm thick, respectively), which are separated by a 60 nm spacer. 37

4.3 Using 3D FDTD, we calculate the input power versus output power (log-log L-L curve) of the hybrid Si-GaAs cavity nanolaser (black circles) and fit the results using a rate equation model (Equation 1) as shown by the orange curve, which corresponds to a spontaneous emission coupling ratio of $\beta = 0.65$. The blue and yellow solid curves are also plotted using the rate equation with spontaneous emission coupling ratios of $\beta = 0.3$ and 1, respectively. The vertical dashed line is the lasing threshold obtained from the rate equation fit to the FDTD data. . . . 41

4.4 Output power vs. input power at the resonance wavelength 1516.53 nm of the hybrid Si-GaAs cavity, featuring quantum dots as saturable absorbers in the GaAs slab. The blue and red curves are the forward and reverse sweeps of the input power, respectively, while the black circles represent the theoretical bistability curve. The purple dashed line is the bistability threshold. 43

A.1 (a) A schematic diagram illustrating the design of the InAs/InP nanobeam mirror with an adiabatic taper, where yellow dashed lines labeled as I-III indicate the positions of cross sections along the nanobeam taper. (b) A white rectangular box depicts the electric field intensity ($|E|$) profile for various cross sections (I-III) of the InAs/InP nanobeam taper. (c) The 3D far-field ($|E|$) profile 500 nm away from the nanobeam taper edge. Here, the black dots represent the far-field profile of the nanobeam, and the color-coded surface map represents the Gaussian mode of the single-mode fiber. 48

A.2 Schematic diagram of the reflectivity measurement setup. Here, NB: nanobeam, LF: lensed fiber, BS: beam splitter, PM: power meter, and PC: polarization controller. 50

A.3 (a, b) Autocorrelation histograms measured at 780 nm under above-band excitation with power levels of (a) 3 μW and (b) 5 μW. The black lines represent the measured data, while the red dashed lines depict curves fitted to the double-sided exponential decay function. (c) The decay rate constant γ_1 at different pump powers obtained from the $g^{(2)}(\tau)$ histogram fits in (a) and (b) and Figure 3a of the main manuscript. The solid blue line is a fit to a linear function. 51

A.4 (a, b) Autocorrelation histogram measurements using at 780 nm laser under above-band pulsed laser excitation with power levels of (a) 250 nW and (b) 5 μW. The black lines represent the measured data, while the red dashed lines depict curves fitted to the double-sided exponential decay function. (c) Detected count rates (red squares) and $g^{(2)}(0)$-corrected count rates (blue squares) as a function of the pump power. The blue line corresponds to a fit with fitting parameters Psat = 1.6 μW and $I_{sat} = 452 \pm 4$ Kcps. (d) $g^{(2)}(0)$ as a function of the pump power. 52
A.5 Hong-Ou-Mandel interferometer setup. The components include LF: lensed fiber, FF: fiber filter, HWP: half waveplate, PBS: polarizing beam splitter, OBJ: objective lens, and SNSPD: superconducting nanowire single-photon detector. Here, L and S represent the long and short fiber paths introduced to create a time difference of 4.36 ns. 53

B.1 FDTD calculated quality factor (Q) for different outcoupling mirrors (NR). Here, the vertical dashed line corresponds to NR = 13. 55
B.2 FDTD calculated quality factor (Q) for different outcoupling mirrors (NR). Here, the vertical dashed line corresponds to NR = 13. 56
B.3 Coupling efficiency as a function of the number of out-coupler mirrors (NR), ranging from 5 to 8, both before (blue circle) and after (red circle) atomic layer deposition. 57
B.4 (a) 3D FDTD simulated quality factors (Q) of the nanobeam cavity for cavity hole radius decrease. (b) The experimental quality factor and (c) reflection coefficient (R) for different atomic layer deposition thicknesses correspond to Figure 3.4a. . 59
B.5 Wavelength change from the cavity resonance wavelength (a) 3D-FDTD simulation of expected wavelength shifts and (b) experimental wavelength change for two different cavities for different atomic layer deposition thicknesses. 60
B.6 The reflection coefficient of cavity at resonance as a function of the number of out-coupler holes (NR), ranging from 5 to 8, both before and after atomic layer deposition. 62

C.1 (a) illustrating the relative confinement between the GaAs slab and Si waveguide for different GaAs slab thicknesses, and (b) Spacer thickness vs. confinement in GaAs slab with thickness 200 nm. Here, in both cases, the Si waveguide has a thickness of 220 nm and a width of 580 nm. 63
C.2 (a) Four-level system with decay time constants between levels 3 to 2 and 1 to 0 of $\tau_{32} = \tau_{10} = 100$ fs, and 2 to 1 and 3 to 0 of $\tau_{21} = \tau_{30} = 300$ ps. (b) The pump and probe time signal (normalized). (c) Electron population density probability vs. time (ps) and inversion between levels 1 and 2. 65
C.3 Average number of photons in the cavity vs. input power for different spontaneous emission coupling ratios β = 0.3, 0.65, and 1. 68
C.4 (a) The quality factor, (b) Wavelength, (c) Lasing threshold power, and (b) Bistability threshold power for silicon waveguide widths of 540 nm, 560 nm, 580 nm, and 600 nm. 69

List of Abbreviations

PIC	Photonic integrated circuit
CMOS	Complementary metal oxide semiconductor
SOI	Silicon-on-insulator
GaAs	Gallium Arsenide
FDTD	Finite Difference Time Domain
Si	Silicon
InP	Indium Phosphide
PDMS	Polydimethylsiloxane
ICP-RIE	Inductively Coupled Plasma-Reactive
MBE	Molecular Beam Epitaxy
NA	Numerical Aperture
PECVD	Plasma Enhanced Chemical Vapor Deposition
PL	Photoluminescence
QD	Quantum Dot
MZI	Mach Zehnder Interferometer
SiN	Silicon Nitride
SEM	Scanning Electron Microscope
AlInAs	Aluminum Indium Arsenide
CCD	Charged Coupled Device
SNSPD	Superconducting Nanowire Single-Photon Detector

Chapter 1: Introduction

1.1 Overview

Single photons are ideal carriers of quantum information over long distances for quantum communication and distributed quantum information processing [1, 2]. However, to function as effective carriers at the optimal telecom wavelength (1260 – 1625 nm), single photon sources must emit with high efficiency and exhibit high photon purity and indistinguishability. Semiconductor quantum dots based on indium arsenide (InAs) exhibit many of these desired qualities, including high brightness, high purity, and indistinguishability, making them an excellent choice as a single-photon source. Another advantage of InAs quantum dots is that their emission in the telecom wavelengths aligns with the compatibility requirements of fiber optic networks. For these reasons, this doctoral dissertation focuses on InAs quantum dots hosted in indium phosphide (InP) as bright, pure, and indistinguishable sources of single photons within the telecom wavelengths. Methods to measure these properties will be discussed in Chapter 2.

A high-quality factor photonic crystal cavity is needed to further improve the brightness of single photon sources through Purcell enhancement [3]. However, fabrication imperfections cause surface roughness, often leading to quality factor degradation in the photonic crystal cavity. Surface passivation is a method to minimize unwanted surface recombination and enhance the performance and reliability of photonic devices. Various passivation techniques have been developed

and employed across semiconductor materials and device structures. One commonly used method is the thermal oxidation of silicon, where a thin layer of silicon dioxide (SiO_2) forms on the silicon surface [4]. This layer acts as a protective barrier against surface contamination and reduces interface states. Similarly, silicon nitride (Si_3N_4) deposition via chemical vapor deposition (CVD) or plasma-enhanced chemical vapor deposition (PECVD) creates a dense layer that effectively passivates the surface, preventing carrier recombination [5]. Another technique involves the use of organic materials such as polymers or self-assembled monolayers (SAMs) [6]. These materials can be deposited via spin coating or solution processing and serve as insulating coatings, passivating the surface by blocking charge carrier traps and reducing surface states. Furthermore, compound semiconductors benefit from specific passivation techniques, such as sulfur passivation of III-V materials [7]. Finally, atomic layer deposition (ALD) enables precise control over thin film deposition, allowing for the formation of ultra-thin passivation layers with excellent uniformity and coverage. In Chapter 3, we optimize atomic layer deposition to improve the quality factor of InP nanobeam cavities featuring InAs quantum dots for high-quality single photon extraction.

Integrating quantum dots with silicon photonics is crucial for achieving efficient and compact photonic integrated circuits (PICs) for quantum information processing. Silicon photonics represents an ideal platform that is compatible with standard CMOS fabrication methods, enabling the seamless integration of photonic devices on a large scale [8]. Its large refractive index enables numerous photonic components within a compact device size, making it an appealing choice for photonic integrated circuits. Other critical advancements in silicon photonics include the development of efficient passive devices and integration with novel materials to address challenges such as light source generation and loss reduction [9]. Furthermore, incorporating single-photon sources in silicon photonics enhances compatibility with existing telecommunications infrastructure,

accelerating the deployment of quantum technologies in real-world applications. As a result, silicon photonics extends its reach into communication [10], computing [11], sensing [12], and beyond.

Silicon photonics represents an ideal platform with standard CMOS fabrication methods, enabling the seamless integration of photonic devices on a large scale [8]. Its large refractive index enables numerous photonic components within a compact device size, making it an appealing choice for photonic integrated circuits. Other critical advancements in silicon photonics include the development of efficient passive devices and integration with novel materials to address challenges such as light source generation and loss reduction [9]. Furthermore, incorporating single-photon sources in silicon photonics enhances compatibility with existing telecommunications infrastructure, accelerating the deployment of quantum technologies in real-world applications. With ongoing research efforts to improve device performance, silicon photonics extends its reach into communication [10], computing [11], sensing [12], and beyond.

In this dissertation, we initially demonstrate an efficient fiber-coupled single photon source at the telecom C-band using InAs/InP quantum dots coupled to a nanobeam photonic crystal for long- distance quantum networks. The tapered nanobeam structure facilitates directional emission that is mode-matched to a lensed fiber, resulting in a collection efficiency of up to 65% from the nanobeam to a single-mode fiber. To further enhance the emission of InAs quantum dots, we utilize atomic layer deposition-based surface passivation of the InP photonic crystal nanobeam cavity to improve the quality factor. These single photon sources based on tapered nanobeam structures can be integrated into a silicon waveguide for hybrid integration. Finally, we propose an alignment-free hybrid Si-GaAs photonic crystal cavity design for hybrid integration in a silicon chip, which can be fabricated without careful alignment. This hybrid cavity holds

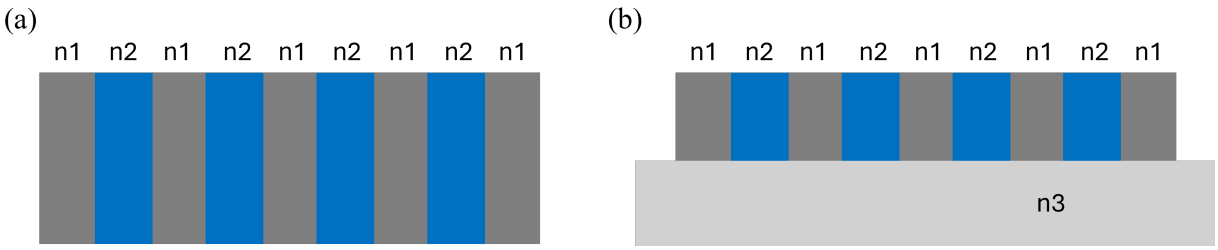


Figure 1.1: (a) Top and (b) cross-sectional views of photonic crystals employing Bragg reflection through refractive index modulation. Here, n_1, n_2, and n_3 correspond to the refractive indices in different materials denoted in gray, blue, and light gray, respectively.

promise for on-chip generation and integrating many single-photon sources into a silicon chip.

1.2 Photonic crystals

Photonic crystals are optical nanostructures characterized by periodic changes in refractive index, finding diverse applications in telecommunications [13], sensing [14], and computing [15]. In telecommunications, they play an essential role in the development of compact and efficient optical waveguides [16], filters [17], and switches [18], facilitating high-speed data transmission and processing. By confining light within these photonic structures, researchers have engineered miniature optical cavities, enabling enhanced light-matter interactions for applications such as lasers [19], modulators [20], and detectors [21]. Photonic crystal structures come in various types, including 1D, 2D, and 3D configurations. Recent advancements in photonic technologies and high-resolution lithography have facilitated the development of 1D photonic crystals with increased integration density and enhanced device performance.

One of the fundamental characteristics of photonic crystals is their capacity to manifest photonic bandgaps, similar to electronic bandgaps observed in semiconductors [22]. To make such photonic crystals, we can use the concept of Bragg interference induced by periodic modulation

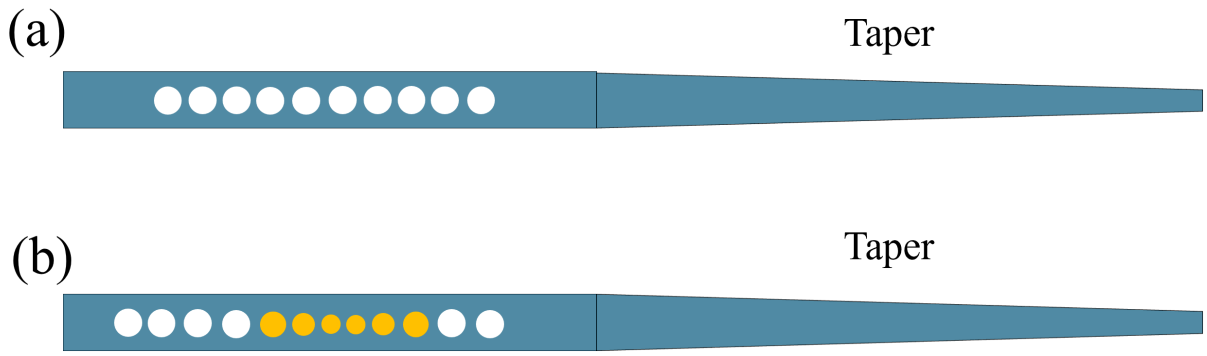


Figure 1.2: (a) Nanobeam photonic crystal mirror and (b) Nanobeam photonic crystal cavity.

of the refractive index, as shown in Figure 1.1. At each interface between media with different refractive index, denoted as n_1 and n_2, occurs partial reflection and transmission of light. Depending on the periodicity of the modulation, reflections at various interfaces constructively interfere only at specific wavelengths, resulting in a photonic bandgap. As a result, the illustrated photonic crystal functions as a mirror for those wavelengths. The width and positioning of these bandgaps rely on the geometry, dimensions, and refractive indexes of the materials.

1.3 Nanobeam photonic crystals

In this dissertation we employ nanobeam crystal structures to enable directional coupling in a single-mode fiber. Figure 1.2a illustrates the design of the nanobeam photonic crystal mirror, which is comprised of a one-dimensional photonic crystal mirror region with periodic arrays of holes in a nanobeam waveguide and a linear taper region. The primary objective of this design is to work as a Bragg mirror and effectively direct photons generated within the nanobeam towards the linear taper, which is subsequently coupled into fiber optics or silicon waveguides.

One approach to further explore the capabilities of photonic crystal structures involves introducing defects into the photonic crystal mirror to form cavities [23]. Figure 1.2b displays

the nanobeam photonic crystal cavity design, where the defect region is composed of 3 pairs of holes with decreasing radius and period within the photonic crystal mirror. The optical mode of the cavity is confined to the area of the defect. Similar to a photonic crystal mirror, the cavity has a nanobeam waveguide region and a linear taper for adiabatically coupling light into fiber optics or silicon waveguides. To direct light from the cavity towards the linear taper, the cavity is made one-sided by reducing the number of holes on the right side. The nanobeam and nanobeam cavity fabrication process will be discussed and outlined in Chapters 2 and 3.

1.4 Hybrid integration of nanobeam photonic crystals

One material cannot fulfill all the properties required in a photonic integrated circuit, necessitating combining two or more different material systems to leverage their respective advantages [24]. For example, silicon photonics is an excellent mature platform for photon routing and propagation. However, the ability to generate classical and non-classical light in silicon is limited. Conversely, quantum dots in III-V materials offer high-quality single photons and lasing capabilities. Yet, the maturity level of photonic components based on III-V materials is less than that of silicon photonics. Thus, an ideal quantum photonic circuit requires integrating III-V materials with silicon. Numerous applications have been demonstrated using hybrid integration techniques, including hybrid light-emitting diodes [25], vertical-cavity surface-emitting lasers [26], photodetectors [27], and sensors [12].

Several approaches have been developed for integrating III-V materials with silicon photonics. One approach involves the straightforward dispersion of quantum emitters hosted in nanoparticles onto a pre-patterned photonic structure, such as the deterministic positioning of colloidal quantum

dots [28]. Alternatively, different materials can be directly grown on top of each other using epitaxial techniques, although film qualities may be compromised due to lattice mismatch [29]. Another method, wafer bonding, offers another approach for fabricating large-scale devices composed of various layers [30]. This technique involves coating two dissimilar wafers with thin layers acting as adhesive agents and applying pressure to the stack of wafers to form a permanent bond between them. Conversely, pick-and-place methods offer the unique ability to separately fabricate and process each chip before integration, which is crucial when processing steps for one chip are incompatible [31]. Epitaxial hetero-growth and wafer bonding offer precise positioning for hybrid integration; however, they remain challenging and necessitate significant expertise to engineer the entire fabrication process. In Chapter 4 of this dissertation, we propose a hybrid photonic crystal cavity for integration into a silicon chip, which can be fabricated using the pick-and-place method. Additionally, we employ the pick-and-place method, particularly transfer printing, as the primary technique for positioning InP nanobeam photonic structures on a silicon chip to enable efficient fiber coupling.

Figure 1.3 illustrates the transfer printing method for an InP nanobeam array onto a silicon chip using a polydimethylsiloxane (PDMS) stamp used in Chapter 2 and Chapter 3. Each process step is monitored using a zoom-lens microscope system from the top, observing through the transparent PDMS stamp with dimensions of $30\times30\times40\ \mu m^2$. The nanobeams are fabricated with a rectangular pad, and the pickup process involves attaching a PDMS stamp to the pad. Subsequently, the PDMS stamp carrying the nanobeam arrays is moved to the desired silicon carrier chip and carefully positioned for placement. These PDMS stamps can be commercially purchased with customizable sizes and adhesion properties, allowing for the transfer of multiple pads with nanobeams. However, this method necessitates using an accurate microscope system

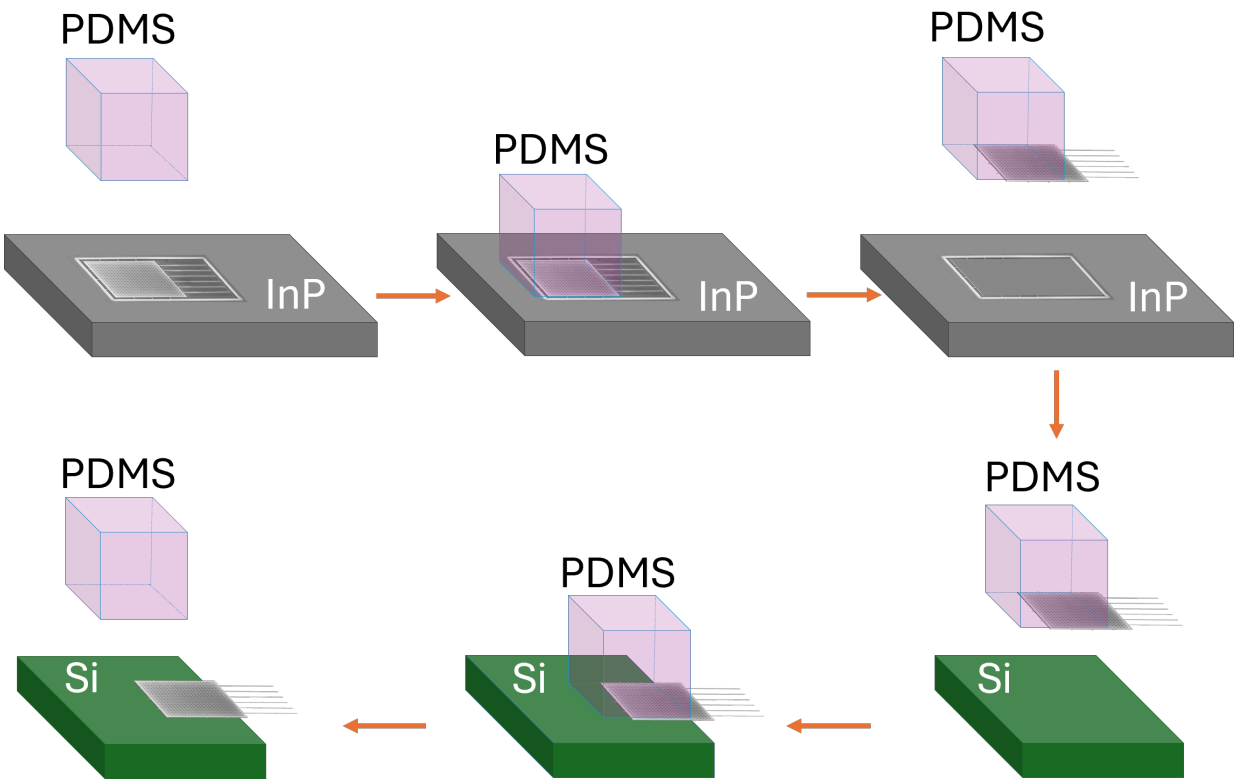


Figure 1.3: Schematic representation of the transfer-printing pick-and-place technique utilizing a polydimethylsiloxane (PDMS) stamp.

to precisely align the nanobeams with other photonic structures.

1.5 Thesis outline

Chapter 2 will discuss the efficient integration of InAs/InP quantum dot emission in single-mode fibers using a tapered nanobeam, as well as single photon generation of C-band single photons with high purity and indistinguishability. In Chapter 3, we will discuss the surface passivation of an InP nanobeam cavity using atomic layer deposition, including optimizing the surface passivation thickness and the importance of outcoupling mirror number for improving the quality factor of the nanobeam cavity. Chapter 4 will discuss the simulation of a hybrid Si-GaAs cavity for hybrid integration in silicon photonics. We will also report our simulation methods for low threshold optical bistability and lasing. Finally, in Chapter 5, we will discuss our current works, simulation, and future directions. Parts of this dissertation have been previously published in the following articles.

Chapter 2 : Rahaman, Mohammad Habibur, et al. "Efficient fiber-coupled telecom C-band indistinguishable photons using a tapered nanobeam." Manuscript in preparation (2024).

Chapter 3 : Rahaman, Mohammad Habibur, et al. "Optimizing the quality factor of InP nanobeam cavities using atomic layer deposition." arXiv preprint arXiv:2312.05967 (2023).

Chapter 4 : Rahaman, Mohammad Habibur, et al. "Hybrid Si-GaAs photonic crystal cavity for lasing and bistability." Optics Express 31.23 (2023): 37574-37582.

Chapter 2: Efficient, indistinguishable telecom C-band photons

2.1 Introduction

A telecom single-photon source operating around 1,550 nm (C-band) is essential for fiber-based quantum communication networks [32] to minimize transmission loss in the silica fiber. Various approaches have been explored to realize single-photon sources within this spectral window, including spontaneous parametric down-conversion [33, 34], as well as materials such as carbon nanotubes [35], and semiconductor quantum dots [36, 37]. Among these methods, single photon sources based on semiconductor quantum dots are considered most promising due to their high brightness [38, 39], high purity [38, 40], and indistinguishability [41–43]. For example, InAs/InP quantum dots emit single photons in the telecom C-band spectrum [40,42–49], which have been extracted utilizing various device structures, such as mesa structures [43], planar cavities [48], nanowires [50], and photonic crystal cavities [39]. However, more efficient coupling to the optical fiber is needed to collect the telecom C-band single photon emission with high efficiency for long-distance quantum networks.

In this chapter, we demonstrate an efficient fiber-coupled single-photon source operating at the telecom C-band using InAs/InP quantum dots integrated in a tapered nanobeam waveguide. The nanobeam efficiently mode-matches the emission of the quantum dots into a lensed fiber, enabling the collection of the emitted light into a single-mode fiber with an efficiency of up to

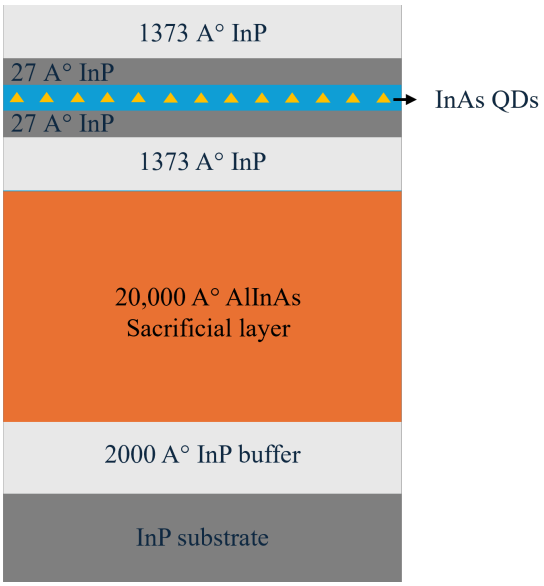


Figure 2.1: Schematic diagram of InAs/InP quantum dots wafer.

65%. Using this device, we report bright single photon emission with a count rate exceeding 575 ± 5 Kcps. From second-order correlation measurements, we determine the photon purity to be $g^{(2)}(0)$ = 0.015 ± 0.003 at 350 nW. We also demonstrate the indistinguishability of the photon emission using Hong-Ou-Mandel two-photon interference measurements with a visibility of 0.84 ± 0.06 and a photon coherence time of 450 ± 20 ps. These results pave the way for efficient fiber collection of single photons at optimal C-band wavelengths for long-distance quantum networks using a tapered nanobeam.

2.2 Nanobeam design and fabrication

The sample is grown on a (100)-oriented Fe-doped InP substrate using molecular beam epitaxy [51, 52]. The wafer consists of a 280 nm thick InP membrane featuring InAs quantum dots at the center, grown on top of a 2 µm thick AlInAs sacrificial layer (Figure 2.1). The quantum dots were formed by first growing a 1.1 monolayer of InAs at a growth temperature of 510 °C.

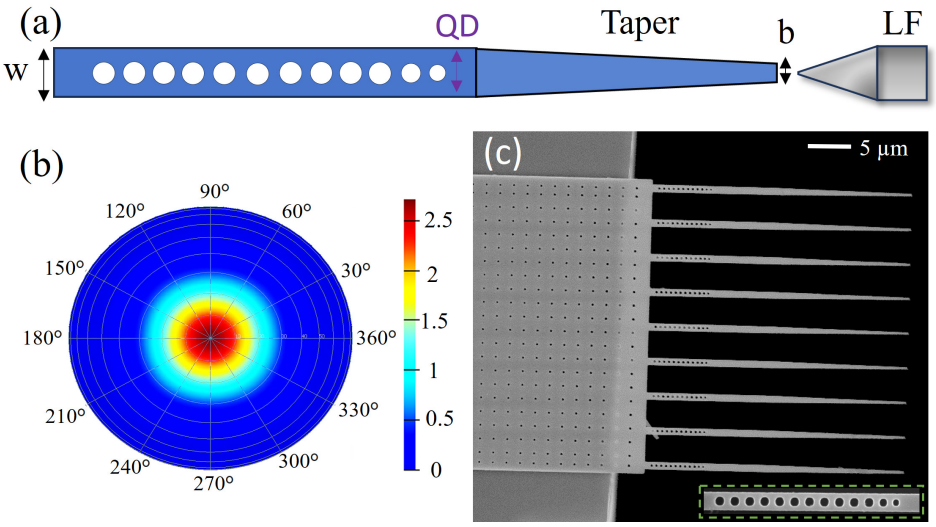


Figure 2.2: (a) Schematic diagram of the top view photonic crystal mirror nanobeam with width w, length L, and taper tip width of b. Here, QD: quantum dots; LF: lensed fiber. (b) The far-field mode profile was calculated at 500 nm from the tapered nanobeam tip edge. (c) SEM image of the fabricated nanobeam arrays after PDMS stamp transfer printing. The inset shows a zoomed-in image of a nanobeam mirror.

This layer was then annealed at the growth temperature for 120 seconds to facilitate the ripening technique [39, 51], enabling control over the density and emission wavelength around 1550 nm. This process resulted in a quantum dot layer with densities between 10 and 50 μm^{-2}. We capped the quantum dots with InP using a double-layer capping configuration [53].

To efficiently collect emission from the quantum dots, we employed a tapered nanobeam structure [54, 55] featuring a periodic array of air holes, which serves as a Bragg mirror to ensure that quantum dot emission is directed towards the tapered end (Figure 2.2a) (see details in Appendix A.1). The width of the nanobeam was adiabatically reduced from 560 nm to 150 nm over a 15 μm long taper to efficiently mode-match to a lensed fiber with a numerical aperture of 0.50. Figure 2.2b displays the 3D-FDTD simulated far-field mode profile of the tapered nanobeam, illustrating the directional emission from the edge of the adiabatic linear taper. Furthermore, using 3D-FDTD, we calculated an 88% coupling efficiency into the lensed fiber,

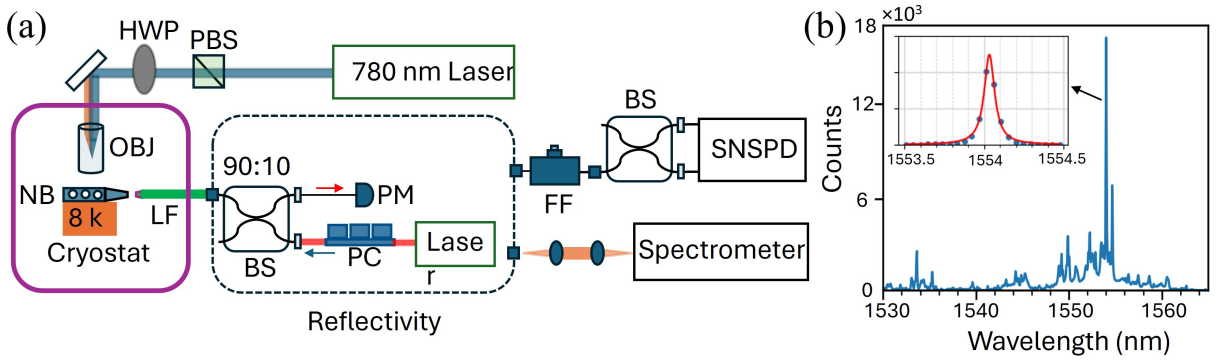


Figure 2.3: (a) Schematic diagram of the optical measurement setup. LF: lensed fiber, FF: fiber filter, NB: nanobeam, HWP: half waveplate, BS: beam splitter, PBS: polarizing beam splitter, OBJ: objective lens, PM: power meter, PC: polarization controller, and SNSPD: superconducting nanowire single photon detector. (b) Time-resolved photoluminescent spectra of quantum dot emission for an above-band excitation of 780 nm at a power 5 μW. The inset shows the zoomed-in spectrum of the QD emission filtered by a 0.2 nm bandwidth tunable fiber spectral filter. Here, the blue circles show the data, and the red solid line represents the Lorentzian fits.

based on the overlap of the far-field emission of the nanobeam taper with a Gaussian function of the fiber mode [56] (see details in Appendix A.1).

To fabricate the designed nanobeam waveguide, we used a combination of electron beam lithography and transfer print lithography using previously reported techniques for nanobeams [54, 57] and nanobeam cavities [58]; details are in Chapter 3. Figure 2.2c shows the transferred structure with the nanobeam array fully suspended from the edge of a cleaved silicon chip. The inset provides a closer view of the photonic crystal nanobeam mirror.

2.3 Results and discussion

Figure 2.3a shows the experimental setup we used to characterize the quantum dot emission. The sample was placed in a closed-cycle cryostat and cooled to 8 K. We aligned the tapered nanobeam to the lensed fiber using a low-temperature 3-axis nanopositioner array within the vacuum chamber. We excite the nanobeam using an above-band laser at an excitation wavelength

of 780 nm, focused through an objective lens. After collection from the lensed fiber, we filtered the light using a 0.2 nm bandwidth tunable fiber spectral filter for single photon counting and measurements. The filtered light was detected using a superconducting nanowire single-photon detector (SNSPD).

We first characterized the coupling efficiency of the nanobeam to the lensed fiber by measuring the direct reflectivity. We injected a tunable external cavity diode laser emitting at 1550 nm into the lensed fiber using a 90:10 fiber coupler and measured the amount of light back-reflected into the fiber with a power meter, as depicted in the dashed box in Figure 2.3a. Assuming that the input coupling and output coupling efficiencies are the same, we determined a 65% coupling efficiency into and out of the device (see details in Appendix A.2). We attribute the discrepancy between the simulated and observed efficiency to fabrication imperfections, angular misalignment between the fiber and nanobeam, and the fact that the photonic crystal mirror may introduce scattering losses.

Next, we characterized the quantum dot emission through photoluminescence. The quantum dots in the nanobeam were excited using the 780 nm laser in continuous wave mode at a power of 5 μW. We detected the emitted light using a spectrometer connected through the lensed fiber. Figure 2.3b shows the collected photoluminescence spectrum from a nanobeam in the telecom C-band window. The spectrum exhibits a series of sharp resonances, which we attribute to individual quantum dots. The inset provides a close-up view of an isolated quantum dot emission line at a wavelength of 1554.05 nm, filtered by a 0.2 nm bandwidth tunable fiber spectral filter. A Lorentzian fit of this emission indicates a line width of 0.067 nm, which is near the spectrometer resolution limit of 0.055 nm. We focused all subsequent experimental measurements on this specific quantum dot.

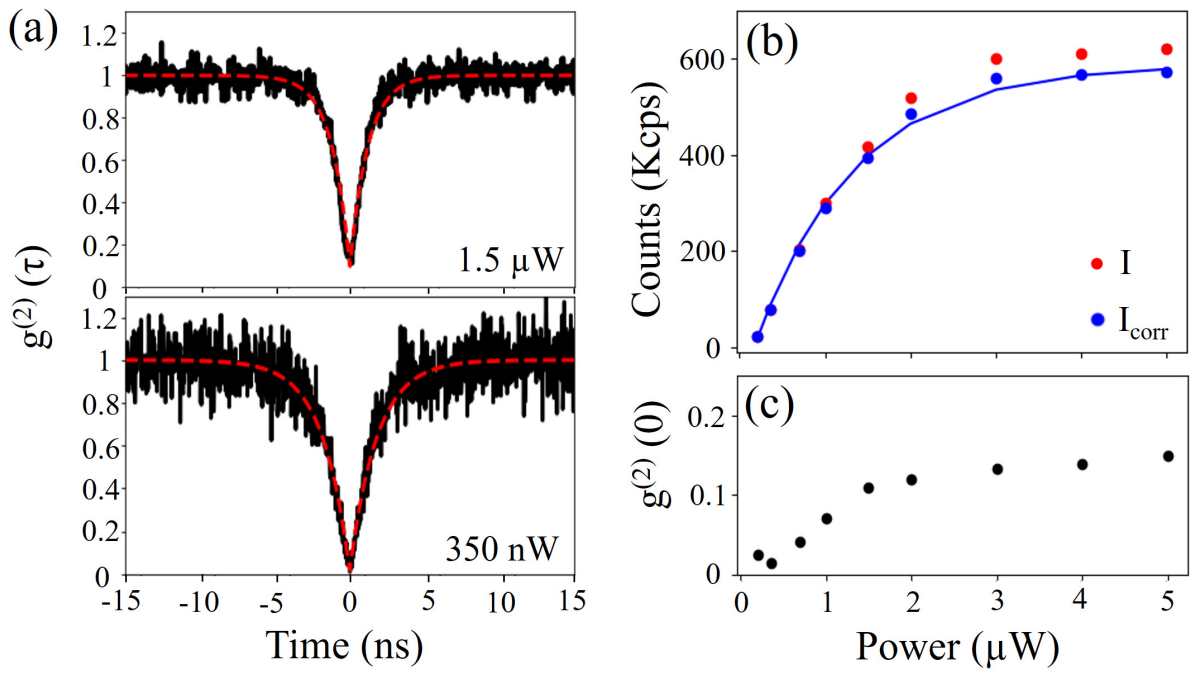


Figure 2.4: (a) Normalized autocorrelation histograms measured at 780 nm under above-band excitation with power levels of 350 nW and 1.5 μW. The black lines represent the measured data, while the red dashed lines depict curves fitted to the double-sided exponential decay function. (b) Detected count rates (red circles) and $g^{(2)}(0)$-corrected count rates (blue circles) as a function of the pump power. The blue line corresponds to a fit to the blue circles with fitting parameters $P_{sat} = 1.19\mu$W and $I_{sat} = 575 \pm 5$ Kcps. (c) $g^{(2)}(0)$ as a function of the pump power.

To verify that the isolated emitter is a single photon source, we performed a second-order autocorrelation measurement. We excited the quantum dot within the nanobeam with the same continuous wave laser operating at 780 nm. In the collection path of the measurement setup, we used a fiber-type 50:50 beam splitter after the fiber filter and two superconducting nanowire single-photon detectors (Figure 2.3a). Figure 2.4a shows the measured second-order correlation for an excitation power of both 350 nW and 1.5 μW. The second-order autocorrelation shows clear anti-bunching, indicating that the emission corresponds to a single quantum dot. By numerically fitting the data to a double-sided exponential function, we determined $g^{(2)}(0)$ = 0.015 ± 0.003 at 350 nW and $g^{(2)}(0)$ = 0.109 ± 0.004 at 1.5 μW, which is exceptional for above-

band excitation and could be further improved using quasi-resonant excitation [44]. From the fit to the second-order correlation, we also calculated the lifetime of the emitter as a function of the pump power-dependent antibunching decay rate constant [59, 60] and extracted a natural radiative lifetime of τ_{rad} = 1.87 ± 0.03 ns (see details in Appendix A.3). This lifetime aligns with previously reported values for InAs/InP quantum dots at the telecom C-band [40].

To quantify the brightness of the quantum dot, we measured the emission intensity as a function of the pump power (Figure 2.4b). The red data points represent the detected count rates (I), which include both the quantum dot emission and background light sources, such as detector dark counts, background light, and broadband Raman emission from other quantum dots in the sample. It thus overestimates the brightness of the emitter. To properly extract the true count rate of the emitter, we also measured the single photon purity $g^{(2)}(0)$ for each pump power, as shown in Figure 2.4c. Using this value, we can calculate the count rate from the emitter only using the equation $I_{corr} = \sqrt{1 - g^{(2)}(0)}$ [61], as shown by the blue data points in Figure 2.4b.

We numerically fit the corrected count rates to the saturation function $I(P) = I_0 + I_{sat}(1 - e^{-P/P_{sat}})$ [61], where P is the pump power, P_{sat} is the saturation power, I_{sat} is the saturation intensity, and I_0 is the dark count, as shown by the blue curve in Figure 2.4b. The emission from the quantum dot exhibits a clear saturation behavior. At low powers, the emission rises linearly, but at high powers, the dot saturates and cannot produce a higher photon rate. From this fit, we determined the quantum dot saturation count rates to be 575 ± 5 Kcps (cps: counts per second). The count rates could be improved by incorporating the dot into a cavity and using the Purcell effect to radiatively enhance the emission [38, 39].

To measure the source efficiency, we measured the second-order autocorrelation using a pulsed laser operating at 780 nm with a pulse duration of 300 ps and a repetition rate of 40 MHz

(see Appendix A.4). We determined the saturation count rate under pulsed excitation to be Isat = 452 ± 4 Kcps, which corresponds to a total end-to-end efficiency of 1.13 ± 0.01%. To assess the source efficiency, we performed a full photon budget of losses in the collection optics and detectors (see details in Appendix A.5). By accounting for these losses, we determined a source efficiency of 12.41 ± 0.09%. This efficiency is influenced by factors such as the non-radiative decay mechanisms of the quantum dot. Additionaly, loss occurs as only the transverse electric (TE) polarizations of the emitter are efficiently coupled to the nanobeam waveguide mode [59]. This inefficiency can be mitigated by using direct resonant π-pulse excitation [62].

To determine the indistinguishability of the source, we performed a two-photon Hong-Ou-Mandel measurement using an unbalanced fiber-based Mach-Zender Interferometer in the collection path (see details in (see details in Appendix A.6). The quantum dot within the nanobeam was once again excited with 1.5 μW pump power, employing the same continuous-wave laser operating at 780 nm. The single photon generated experiences a time delay $\Delta\tau_2$ of 4.36 ns at the first fiber-type beam splitter before eventually colliding at the second fiber-type beam splitter of the unbalanced Mach-Zender Interferometer, allowing us to determine indistinguishability.

Figures 2.5a and 2.5b show the measurement results of the Hong-Ou-Mandel experiment for co-polarized (indistinguishable) and cross-polarized (distinguishable) photons, respectively. The central dip corresponds to the two-photon interference at the second fiber-type beam splitter. In the case of indistinguishable photons, the central dip at zero-time delay falls below the classical limit of 0.5 [63], as indicated by the blue dashed horizontal line (Figure 2.5a). Additionally, in both cases, two dips near 0.75 at ± 4.36 ns are due to the delay introduced by the interferometer. The red dashed lines in Figure 2.5 represent correlation functions for the cross-polarized $g_{\perp}^{(2)}(\tau)$ and co-polarized $g_{||}^{(2)}(\tau)$ cases for a continuous-wave Hong-Ou-Mandel experiment provided by

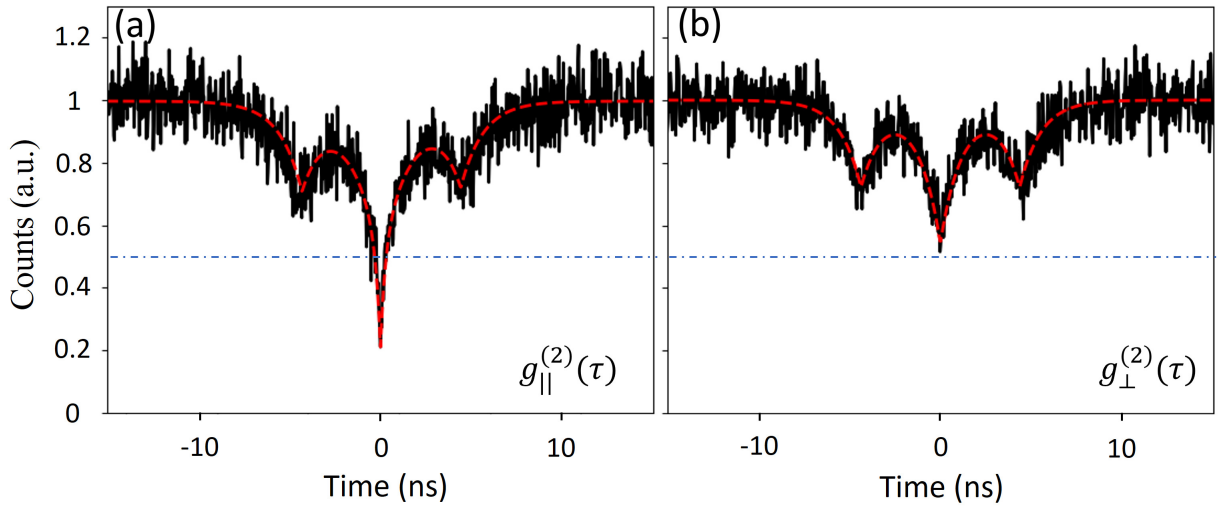


Figure 2.5: Two-photon interference for (a) indistinguishable photons with parallel polarization and (b) distinguishable photons with orthogonal polarization at 1.5 μW pump power using a continuous wave laser at 780 nm, with respective fit functions represented by red dashed lines. (c) A zoomed-in view of panel (a).

[63, 64].

$$g_{\perp}^{(2)}(\tau) = 4(T_1^2 + R_1^2)R_2T_2g^{(2)}(\tau) + 4R_1T_1[T_2^2g^{(2)}(\tau - \Delta\tau_2) + R_2^2g^{(2)}(\tau + \Delta\tau_2)] \tag{2.1}$$

$$g_{||}^{(2)}(\tau) = 4(T_1^2+R_1^2)R_2T_2g^{(2)}(\tau)+4R_1T_1[T_2^2g^{(2)}(\tau-\Delta\tau_2)+R_2^2g^{(2)}(\tau+\Delta\tau_2)]\times(1-Ve^{(-2|\tau|/\tau_c)}) \tag{2.2}$$

Where $R_{1,2}$ and $T_{1,2}$ denote the reflection and transmission probabilities of the two beam-splitters within the interferometer and $g^{(2)}(\tau)$ represents the second-order autocorrelation. In the co-polarized case, the additional terms include τ_c, which stands for the coherence time of the single-photon source, and V, which represents the overlap of wave functions at the second beam splitter. From equation 3, we determined the coherence time was τ_c= 450 ± 20 ps. This value is similar to the best reported results for C-band single photon sources under non-resonant and resonant excitation (440 ± 45 ps and 447 ± 15 ps) [48, 49]. A high coherence value could

enable high fidelity quantum information processing and increase the efficiency in repeater-based quantum communication systems at telecom C-band wavelengths [65].

We also evaluated the visibility of the indistinguishable photons based on coincidence counts for the co-polarized and cross-polarized photons. The degree of indistinguishability or visibility is defined as $V_{HOM} = 1 - \frac{g_{\perp}^{(2)}(0)}{g_{||}^{(2)}(0)}$, derived from the zero-delay autocorrelation values of the cross-polarized and co-polarized cases. From the Equation 2 and 3, the raw visibility was determined to be $V_{HOM} = 0.64 \pm 0.04$. However, visibility is constrained by the nonzero $g^{(2)}(0) = 0.109 \pm 0.004$ value at 1.5 μW pump power, as shown in Figure 2.4a. We corrected the visibility based on this $g^{(2)}(0)$ value, providing the upper bound of visibility as $M_S = \frac{V_{HOM}+g^{(2)}(0)}{1-g^{(2)}(0)}$ [66, 67]. Following the $g^{(2)}(0)$ correction, the visibility of indistinguishable photons reached $M_s = 0.84 \pm 0.06$. The observed experimental visibility is lower than the ideal value (M_s= 1), primarily due to the finite time resolution of the detector, the timing jitter of our detector, and dark counts.

2.4 Summary and discussion

In conclusion, we have demonstrated efficient fiber-coupled C-band indistinguishable photons using an InAs/InP quantum dot coupled to a tapered nanobeam. We achieved C-band single photons with a count rate of 575 ± 5 Kcps, $g^{(2)}(0)$ = 0.015 ± 0.003, two-photon interference visibility of 0.84 ± 0.06, and a photon coherence time of 450 ± 20 ps using above-band excitation. The efficiency of the device could be further improved by employing resonant cavities that increase radiative efficiency through the Purcell effect [39]. Moreover, utilizing resonant excitation [68], quasi-resonant excitation [69], and nanoscale focus pinspot [70] techniques could further

reduce the $g^{(2)}(0)$ value and improve indistinguishability by suppressing the time jitter induced by relaxation to the exciton ground state. In addition to reducing fiber losses, the current device structure can be coupled to integrated photonic circuits to serve as an on-chip single-photon source [71–73]. Ultimately, this tapered nanobeam design could enable new devices for quantum communication and distributed quantum computing by enabling the direct emission of telecom C-band photons without quantum frequency conversion [74].

Chapter 3: Atomic layer deposition based surface passivation of InP nanobeam cavity

3.1 Introduction

Due to their compact size, nanobeam photonic crystal cavities have a remarkable ability to confine light both spatially and temporally, which makes them valuable for ultra-small lasers [75, 76], nonlinear optics [77, 78], sensing [79, 80], quantum optics [81, 82], and photonic integrated circuits [83, 84]. For example, nanobeam cavities utilizing III-V materials, such as InP, are extensively used for active nanophotonic devices that incorporate quantum dots and quantum wells [85, 86]. However, due to fabrication imperfections, nanobeam cavities often feature low quality factors. These imperfections are mainly due to dry-etching techniques that create surface roughness and absorption caused by the formation of surface states that act as recombination sites for free carriers [87–90]. Such challenges emphasize the ongoing need for innovative approaches and techniques to address the complications of fabricating and preserving high quality factor nanobeam cavities.

Atomic layer deposition is a versatile thin-film deposition technique that features precise thickness control, uniformity along the surface normal [91], and the ability to modify material properties at the nanoscale [92]. These properties have been harnessed in various applications,

including refractive index sensing [93], microlens arrays [94], and resonance tuning of 2D photonic crystals [95, 96]. Additionally, the conformal film reduces surface roughness. As a result, atomic layer deposited films like Al_2O_3 have been shown to decrease propagation losses in waveguides [97], improve the performance of lasers [98], and provide surface passivation of III-V semiconductors [99] and photodetectors [100], as well as improve the quality factor of silicon nanobeam cavities [101]. These findings suggest it would be a promising direction to explore atomic layer deposition as a passivation technique to enhance the quality factor of InP nanobeam cavities, though there has been a lack of experimental reports.

In this chapter, we demonstrate improved quality factors for an InP nanobeam cavity operating at telecom wavelengths through surface passivation by atomic layer deposition of Al_2O_3. We optimize the atomic layer deposition by sequentially adding 2-nm-thick coatings of Al_2O_3 at 150 °C on top of the InP nanobeam cavity. From this process, we determine the optimized layer thickness to be 6 nm, which improves the average quality factor by up to 140%. This enhancement is attributed to the reduction of out-of-plane scattering loss and surface absorption following the atomic layer deposition. In addition to improving the quality factor, we show the Al_2O_3 coating can tune the resonant wavelength of the InP nanobeam cavity. This atomic layer deposition approach can improve the performance of InP nanobeam cavities for applications in both classical optoelectronics and quantum optics.

3.2 Nanobeam cavity design

Figure 3.1a illustrates the nanobeam cavity used in this work. The nanobeam is designed to be an air-clad structure. We numerically optimized the design to achieve a cavity resonance

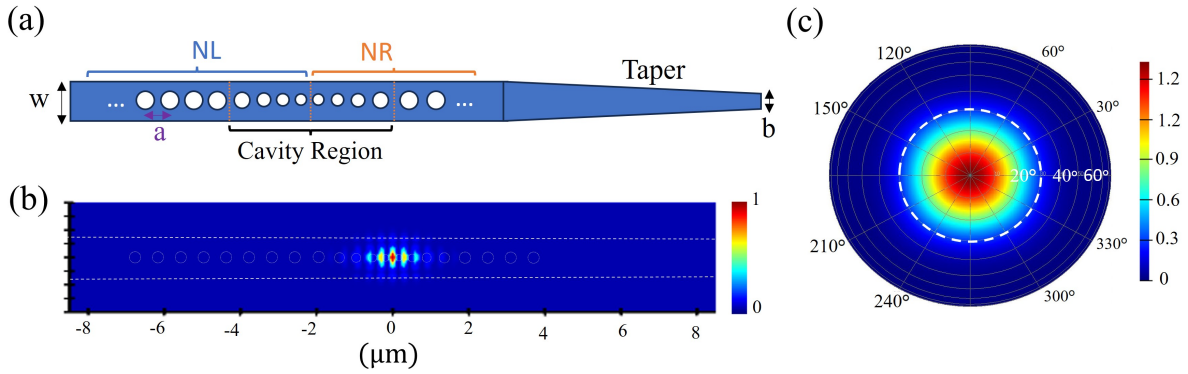


Figure 3.1: (a) The tapered nanobeam InP photonic crystal cavity design with width w, lattice parameter a, and hole radius r. The cavity region is realized by tapering and shifting 4 pairs of holes by a factor of 0.935, towards the center. NL and NR are the total number of holes (including the tapered 4 holes) on the left and right sides of the nanobeam, respectively. (b) The 3D-FDTD simulated fundamental mode profile ($|E|^2$) of the nanobeam cavity, and (c) the far-field mode profile calculated from the nanobeam taper edge with width b. The white dashed line in the far-field profile corresponds to a numerical aperture of 0.5 of the objective lens.

at the telecom O-band with an optimal value of width w = 475 nm, lattice parameter a = 350 nm and radius r = 92 nm. The cavity region is realized by gradually reducing the radius and lattice parameter of the 4 pairs of holes toward the center by a factor of 0.935. The left side (NL) consists of 13 holes that are fully reflective, and we varied the number of holes of the right side (NR) from 5 to 8 holes that are partially reflective, which allows us to control the coupling strength of the cavity into the nanobeam waveguide [77] (see details in Appendix B.1). We use 3D finite-difference time-domain (FDTD) simulations to calculate the theoretical quality factor to be 3.65×10^4, and the mode volume $V \approx 0.55(\lambda/n)^3$ for NR = 8. Figure fig:ald1b presents the fundamental mode profile ($|E|^2$) of the optimized nanobeam cavity at a wavelength of 1310 nm. The width of the nanobeam waveguide is adiabatically reduced from $w = 475$ nm to $b = 150$ nm over a 15 μm-long linear taper to enable outcoupling to the lensed fiber (see details in Appendix B.2). In Figure fig:ald1c, the 3D-FDTD calculated Gaussian far-field mode profile from the edge of the linear taper displays the directionality of the emission. The white dashed line within the

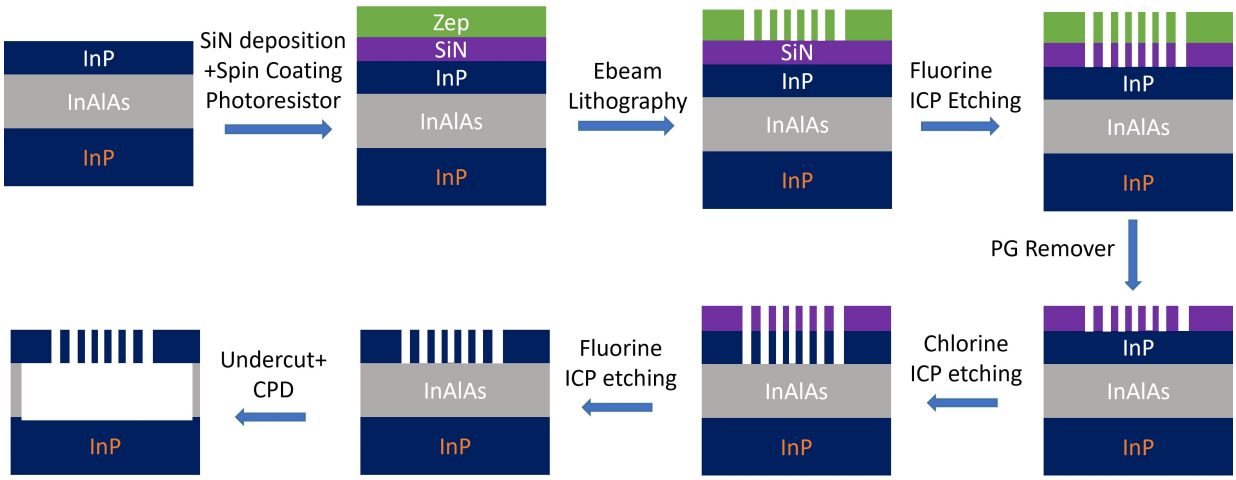


Figure 3.2: InP nanobeam cavity fabrication steps using SiN hard mask. Here, CPD: critical point drier.

far-field profile corresponds to a numerical aperture of 0.5, which represents a coupling efficiency of 90% to a lensed fiber.

3.3 Nanobeam cavity fabrication

To fabricate the nanobeam cavity, we utilized a two-layer etching process [54, 102], as depicted in the steps outlined in Figure 3.2. Initially, we applied a 170 nm silicon nitride film on a 280 nm thick InP membrane with InAs quantum dots as an etching mask using plasma−enhanced chemical vapor deposition. Subsequently, we employed electron beam lithography with fluorine−based reactive ion etching to pattern the nanobeam cavities onto the silicon nitride layer. Next, a chlorine−based reactive ion etching process was employed to transfer this pattern onto the InP layer. Finally, to make the nanobeam cavities suspended from a 30×30 μm^2 square pad, as shown in Figure 3.3a, we use chemical wet etching of a $2-\mu$m$-$thick InAlAs sacrificial layer utilizing a mixture of H_2O, HCl (37%), and H_2O_2 (30%) in a 3:1:2 ratio. To ensure that the nanobeam structures do not bend or collapse on the substrate, they were immersed in isopropyl

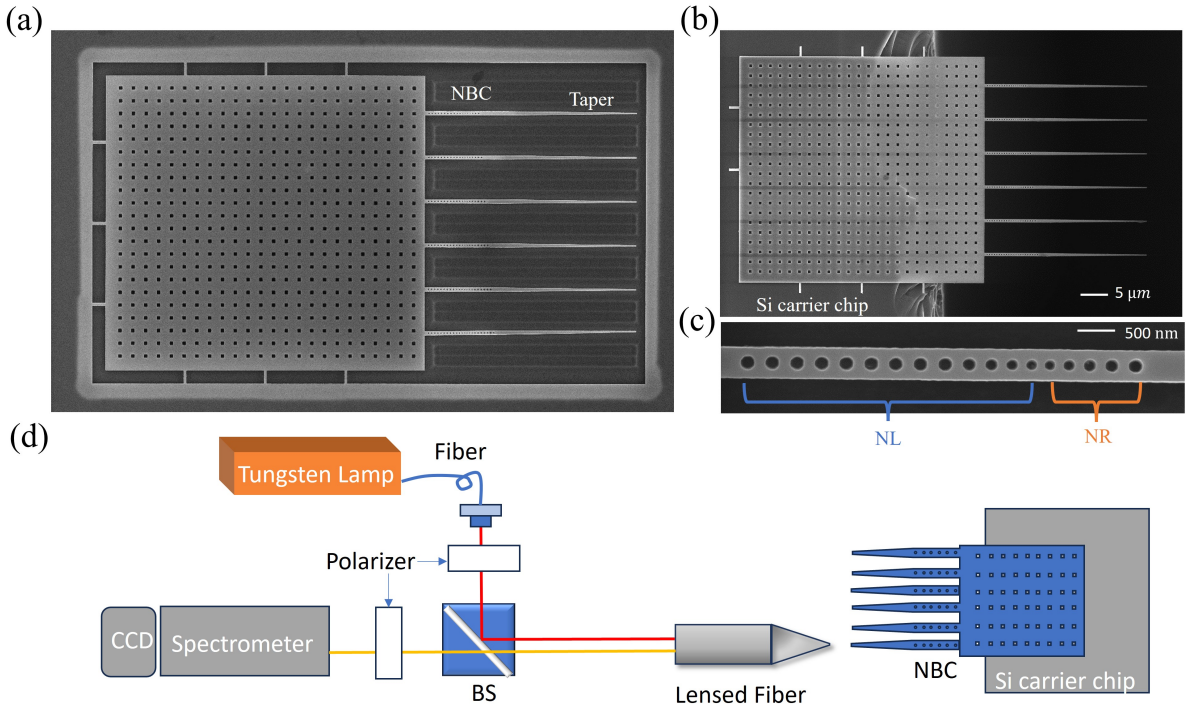


Figure 3.3: (a, b) SEM images of an array of nanobeam cavities after (a) wet etching and (b) transfer printing. (c) Zoomed-in view of a nanobeam cavity after transfer printing and 2 nm atomic layer deposition of Al_2O_3. (d) Schematic diagram of the reflectance spectra measurement setup for the InP nanobeam cavity (NBC) array; BS: Beam splitter.

alcohol and dried using a critical point drier after the wet etching process. We note that the InAs quantum dots has a low density of 10 μm^{-2}, which may contribute additional losses beyond the native losses of the InP substrate.

In order to achieve suspended nanobeam cavities with direct access to lensed fiber coupling, we used transfer print lithography to transfer the nanobeam cavity array to the edge of a silicon carrier wafer. This transfer was performed using a polydimethylsiloxane stamp with dimensions of $30 \times 30 \times 40$ μm^3. Figure 3.3b displays a scanning electron microscopy (SEM) image illustrating the transferred nanobeam cavity arrays with the square pad positioned on the edge of the silicon carrier chip. Figure 3.3c shows the zoomed-in nanobeam cavity array after transfer printing and 2 nm atomic layer deposition.

3.4 Nanobeam cavity characterization

We first characterized the fabricated nanobeams prior to Al_2O_3 deposition using the experimental setup illustrated in Figure 3.3d. In this arrangement, we employed a broadband stabilized tungsten-halogen lamp, which we directed into the tapered side of the suspended nanobeams using a lensed fiber with an objective lens of 0.5 numerical aperture. The reflected light from the nanobeam cavities was collected using a 90:10 beam splitter and directed toward a monochromator equipped with an InGaAs detector array. We determined the coupling efficiency by calculating the ratio of the total reflected and injected optical power between the nanobeam cavity and the objective lens, yielding a value of 55%, which is lower than the FDTD simulated coupling efficiency of 90% (see details in Appendix B.3). The disparity between the measured and simulated efficiencies can be attributed to factors such as imperfect angular alignment of the transferred nanobeams with the optical axis of the objective lens, scattering losses due to surface roughness of the tapered out-coupler, and mismatch of the numerical aperture between the nanobeam taper and the lensed fiber.

We employed atomic layer deposition to passivate the surface of the fabricated InP nanobeam cavities. This process initiates chemical reactions at the sample surface and is designed to be self-limiting, which means the film thickness can be accurately controlled by counting the number of deposition cycles [91]. In our study, we employed an Al_2O_3 atomic layer deposition process, utilizing trimethylaluminum ($Al_2(CH_3)_6$) and water (H_2O) as precursors for each cycle [103]. We performed 20 cycles for each deposition step, resulting in an Al_2O_3 thickness of 2 nm. The atomic layer deposition process was conducted at an operating temperature of 150 °C to ensure uniform deposition. The use of Al_2O_3, characterized by its low refractive index (1.75 at 1.31

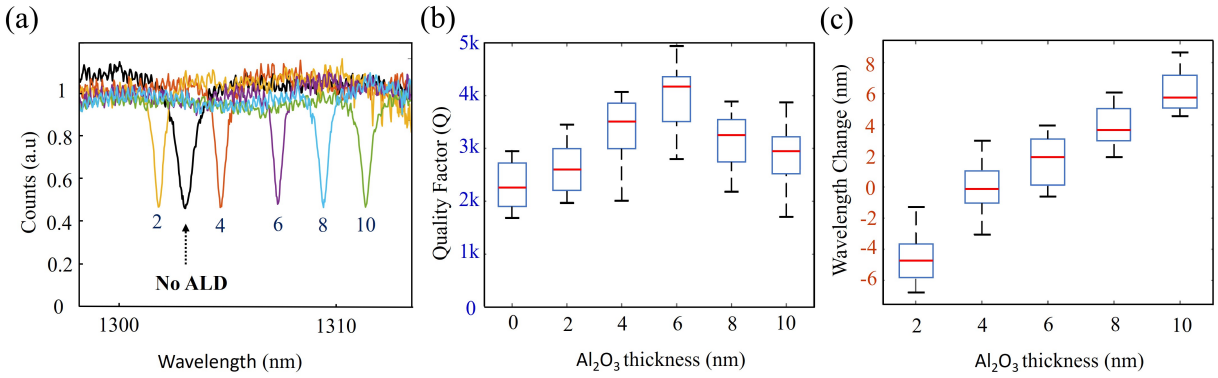


Figure 3.4: (a) Normalized reflectance spectra of a nanobeam cavity with NR = 7 for different thicknesses of Al_2O_3 using atomic layer deposition. The black curve, representing spectra without ALD, is blue-shifted by 1 nm to prevent overlap. (b) Average quality factors of 30 nanobeam cavities with NR = 7 for different atomic layer deposition thicknesses, with the average quality factor indicated by the red horizontal line, and (c) Average wavelength shifts from the cavity resonance wavelength.

μm), makes it a valuable tool for tailoring the optical properties of photonic devices [101].

We measured the reflectance spectra of a nanobeam cavity with NR = 7 after increasing steps of atomic layer deposition, as shown in Figure 3.4a. The normalized reflectance spectra demonstrate a reduction in linewidth for Al_2O_3 thicknesses of 2, 4, 6, 8, and 10 nm compared to the nanobeam cavity prior to atomic layer deposition. We calculated the quality factor values by fitting the reflection spectra using the Lorentzian function (see details in Appendix B.4). Applying a similar quality factor analysis to 30 cavities as a function of the Al_2O_3 thickness, we plotted the average quality factor in Figure 3.4b. The quality factor initially increases, reaching an average maximum quality factor of 4235 when the Al_2O_3 thickness is 6 nm. However, thicker Al_2O_3 layers lead to a reduced quality factor, with a significant decrease observed for thicknesses exceeding 10 nm. This trend is similar to the FDTD simulations, where the quality factor is highly dependent on the hole radius and decreases as the radius decreases (see details in Appendix B.5). Additionally, the resonance wavelength of the cavity is also impacted by the Al_2O_3 thickness,

which is a consistent increase in wavelength (Figure 3.4c). We believe the initial decrease in the cavity wavelength is due to the removal of native oxide [104, 105] in the atomic layer deposition chamber, resulting in an average reduction of 7 ± 2.6 nm (see details in Appendix B.6). From these measurements, we show that atomic layer deposition can tune the cavity over a 10.5 nm wavelength range without degradation to the cavity quality factor.

We next measure the reflectance spectra of the nanobeam cavities as a function of the number of holes in the output coupling mirror (NR), which controls the output coupling strength. Figure 3.5a, b displays the normalized reflectance spectra before (Figure 3.5a) and after (Figure 3.5b) deposition of a 6 nm thick Al_2O_3 coating for different values of NR, ranging from 5 to 8. As expected, after atomic layer deposition, we observed decreased linewidth in the full width at half maximum ($\Delta\lambda$), as shown in Figure 3.5b. Additionally, we find the cavity reflectance minima strongly depends on NR, both with and without Al_2O_3 deposition. At NR = 6, the reflectance dip drops to nearly zero, indicating a near-critical coupling condition [106]. We also observe a clear transition between the over- and under-coupled regimes at NR = 5 and NR $\geq$ 7, respectively. Different coupling regions are of interest for various applications; the under-coupling region is particularly significant for characterizing low power optical frequency microcombs [107, 108], while critically coupled cavities are essential in nonlinear optics and optical sensing [106]. We also note that the reflectance minima for NR = 6 increases after atomic layer deposition, indicating that the device was brought even closer to the critical coupling regime, likely due to reduced cavity loss by the surface passivation process.

We also investigate the cavity quality factor as a function of NR, as shown in Figure 3.5c. The measured quality factor is defined as $Q = \frac{\lambda}{\Delta\lambda}$, where the resonance wavelength λ and linewidth $\Delta\lambda$ are determined from the Lorentzian fit to the reflection spectra in Figure 3.5a,

b. The blue curve in Figure 3.5c illustrates the experimentally calculated quality factor before the atomic layer deposition process, while the red curve shows the quality factor after the deposition of 6 nm of Al_2O_3. From this curve, we observe an enhancement in the quality factor for all NR values. This enhancement is also more prominent in the under-coupled regions (NR $\geq$ 7) than in the over-coupled (NR = 5) and critically coupled regions (NR = 6). For example, the most significant improvement in quality factor after the atomic layer deposition treatment is observed for NR = 8, with a 155% increase.

To gain a better understanding of why the quality factor exhibits greater improvement with higher NR (under-coupled regime), we perform numerical modeling. The quality factor of the cavity is given by Equation (1) [109, 110].

$$\frac{1}{Q} = \frac{1}{Q_{||}} + \frac{1}{Q_{\perp}} \tag{3.1}$$

where $Q_{||}$ is the quality factor for the decay rate into the nanobeam, and $Q_{\perp}$ is the quality factor for the out-of-nanobeam decay rate. We assume that reducing the number of holes in the output-coupling mirror decreases $Q_{||}$, but does not significantly affect $Q_{\perp}$, which is dominated by scattering and material losses [110, 111]. Therefore, we first compute $Q_{\perp}$ utilizing reflection (R) at the cavity resonance before and after atomic layer deposition for NR = 8, which can be expressed as $R = (Q/Q_{\perp})^2$ using coupled-mode theory [111] (see details in Appendix B.7). Then we determine $Q_{||}$ using Equation 1. The graphical representation in Figure 3.5d illustrates the calculated values of $Q_{||}$ and $Q_{\perp}$ with respect to NR. As anticipated, the plot reveals an upward trend in $Q_{||}$ as NR increases. $Q_{||}$ is high in regions characterized by under-coupling, indicating that the overall Q factor is approximately ($Q \approx Q_{\perp}$) [110–112]. Consequently, after atomic layer

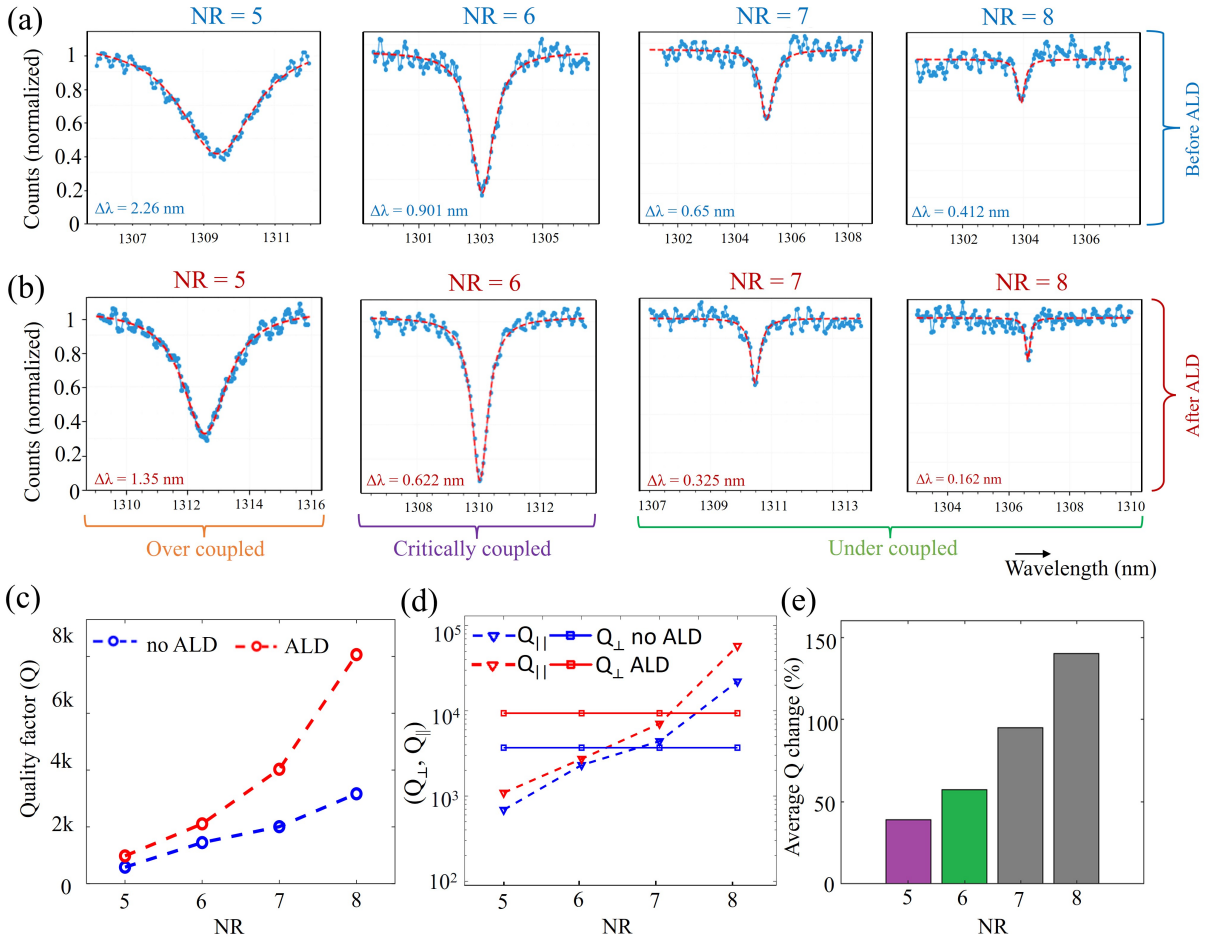


Figure 3.5: Normalized reflectance measurements spectra along with Lorentzian fits for a range cavity hole numbers of out-coupling mirror (NR) from 5 to 8 (a) Before ALD and (b) After ALD. The measurements are in blue circles, while the red dashed curve represents the Lorentzian fit. (c) the corresponding measured quality factor for the same nanobeam cavities for different NR before (blue) and after (red) atomic layer deposition (ALD) of a 6 nm coating of Al_2O_3. (d) Calculated $Q_{||}$ and $Q_{\perp}$ from Equation (1) values before (blue) and after (red) the atomic layer deposition treatment. (e) Average percentage change in the quality factor (Q) across 20 samples for NR values ranging from 5 to 8. Purple, green, and gray color schemes correspond to the respective over-coupled, critically coupled, and under-coupled regions.

deposition, the total quality factor (Q) is higher, particularly in the under-coupled regions.

We perform a similar analysis for 20 samples for each value of NR before and after 6 nm atomic layer deposition. Figure 3.5e plots the average change in total quality factor after atomic layer deposition as a function of the output coupling mirror (NR). The different colors purple, green, and gray correspond to coupling regions that are over-coupled, critically coupled, and under-coupled, respectively. As expected, the lowest average improvement in quality factor is 40% for NR = 5, while the most significant enhancement is observed for NR = 8, with an average increase of 140%.

3.5 Summary and discussion

In conclusion, we have demonstrated atomic layer deposition of Al_2O_3 as a valuable technique for significantly enhancing the quality factors of InP nanobeam cavities and tuning the wavelength. We also investigated the impact of coupling regions on quality factor improvements, revealing a 140% average increase in the under-coupling region. Furthermore, we demonstrated that atomic layer deposition can tune the wavelength of the cavity by over 10.5 nm without any degradation to the quality factor. Despite the potential of atomic layer deposition-based passivation to decrease surface roughness and minimize scattering losses at the Al_2O_3–air interface, a considerable loss may persist after Al_2O_3 deposition. A deeper exploration of the quality factor improvement through atomic layer deposition, considering various designs and material systems, will provide valuable insights. Additionally, surface treatment of nanobeam cavities using sulfur passivation [89] before atomic layer deposition could further improve the quality factor. Our findings hold promise to improve the light-matter interaction of InP nanobeam cavities with individual emitters

and tune the cavity wavelength to match that of the emitters. Atomic layer deposition passivated cavities could also enable low-threshold laser by reducing the nonradiative surface recombination rate [113].

Chapter 4: Hybrid Si-GaAs photonic crystal cavity

4.1 Introduction

Silicon is a promising candidate for photonic integrated circuits due to its low power consumption, low cost, and high integration density. [114] Additionally, silicon on an insulator provides a high index contrast platform [115, 116] that enables the fabrication of extremely compact passive optical devices, such as low loss waveguides, [117, 118] grating couplers, [119, 120] mode converters, [121] multiplexers, [122] and more. However, silicon lacks active optical properties due to its indirect bandgap, which has impeded the development of silicon-based photonic integrated circuits. As an alternative, direct bandgap III-V semiconductors (e.g., GaAs) offer significant active optical properties such as light emission and absorption at telecom wavelengths. In particular, III-V nanophotonic devices can implement low threshold lasers, [123] amplifiers, [124] modulators, [125] and highly nonlinear devices [77]. The integration of III-V nanophotonic devices with silicon could pave the way towards ultra-compact low energy nanophotonic and optoelectronic devices. Researchers have increasingly explored the heterogeneous integration of III-V materials with silicon to utilize the advantages of both systems [115, 126].

A commonly used method for this heterogeneous integration is achieved by placing a III-V nanophotonic device in close proximity to a silicon waveguide and relying on evanescent coupling between the two structures. Based on this technique, several nanophotonic designs (e.g.,

nanolasers) have been proposed and demonstrated. [85,127–130] However, this approach requires careful placement and alignment of the nanophotonic cavity patterned in the III-V material with the evanescent field of the waveguide to achieve efficient coupling. Such active alignment can significantly complicate the design and fabrication of integrated photonic devices. [131] An alternative approach is the use of hybrid photonic modes to couple silicon and III-V semiconductors without the need for precise alignment. In this approach, the mode of a silicon waveguide is carefully engineered to hybridize with a III-V semiconductor layer that serves as the active material. [132] Such hybrid modes have been used to engineer laser sources, [132,133] amplifiers, [134] and modulators. [135] However, their use in other nanophotonic devices, such as hybrid cavities, remains unexplored.

In this chapter, we propose and analyze a hybrid mode approach for engineering a Si-GaAs nanophotonic cavity that enables low-power-threshold lasing and optical bistability at telecom wavelengths without the need for careful alignment. Unlike previous hybrid integration approaches, we utilize a patterned silicon cavity structure coupled to a wider, symmetric GaAs slab embedded with InAs quantum dots. This approach alleviates the need for careful alignment between the silicon photonic waveguide and III-V semiconductor material. We numerically design and characterize the structure using the 3D finite-difference time-domain (FDTD) method coupled to a Maxwell-Bloch equation model that accounts for the active material in the GaAs slab. [136, 137] The proposed design provides a low lasing threshold of just 156 nW, which we attribute to the high spontaneous emission coupling ratio enabled by the low mode volume of the active media in the hybrid cavity. [75] Additionally, under continuous wave operation, we found this hybrid cavity has a low optical bistability threshold of 18.1 μW. This hybrid Si-GaAs cavity design can be optimized for different operating frequencies and integration with other active

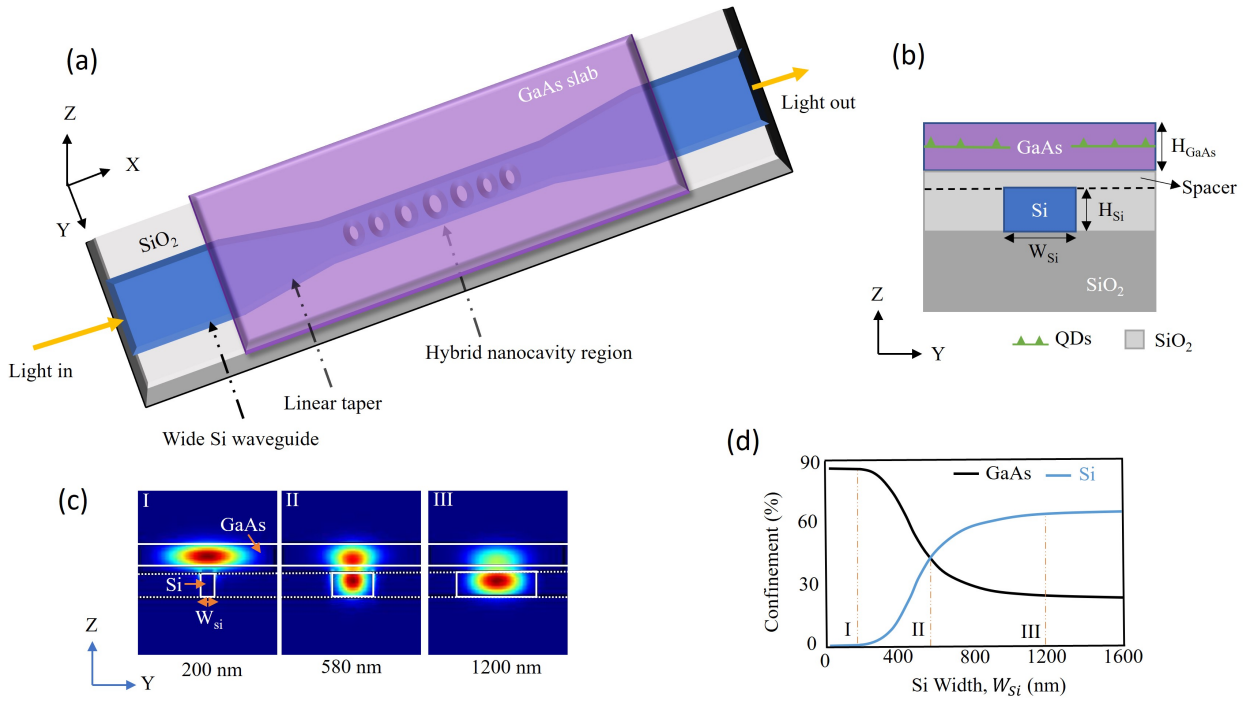


Figure 4.1: (a) 3D schematic illustration of the Si-GaAs hybrid cavity, and (b) the corresponding 2D cross-section. (c) The transverse mode profile ($|E|$) of the hybrid mode (TE polarized) for different silicon waveguide widths (W_{Si}) of 200 nm, 580 nm, and 1200 nm at a fixed GaAs slab width of 2 μm at an incident light wavelength of 1516.53 nm. The solid white lines represent the boundaries of the silicon waveguide and GaAs slab. (d) The silicon waveguide width controls the relative confinement of the hybrid mode in the silicon waveguide and GaAs slab region, where positions I, II, and III correspond to the different silicon waveguide widths marked in (c).

materials beyond quantum dots, such as Kerr nonlinear media. [138] This work could enable a simpler and more scalable approach for the heterogeneous integration of III-V materials with silicon nanophotonics.

4.2 Proposed hybrid Si-GaAs cavity design

Figure 4.1a illustrates the 3D structure of the hybrid device, which features a wide silicon waveguide with a 920 nm width that couples light and narrows down through a 3.25 μm linear taper. The narrower silicon waveguide with the cavity pattern couples to the GaAs slab, forming the hybrid nanocavity region. An additional linear taper enables efficient light transmission from the cavity through the wide silicon waveguide on the other side of the device. Figure 4.1b shows the cross-section of the hybrid structure without the cavity pattern, which consists of a silicon waveguide coupled to a GaAs slab containing InAs quantum dots. The waveguide is embedded in a SiO_2 cladding, and a spacer layer with thickness t separates it from the GaAs slab. We define the silicon waveguide's height and width are H_{Si} and W_{Si}, respectively, while the height of the GaAs slab is H_{GaAs}.

We first analyze the hybrid mode structure of the silicon waveguide without a patterned cavity coupled to the GaAs slab. We simulate the mode structure of the waveguide by direct eigenmode expansion (ANSYS MODE solutions) for the case where t = 60 nm, H_{Si} = 220 nm [139] and H_{GaAs} = 200 nm [77, 140] (see Appendix C.1). Figure 4.1c shows the transverse mode profile of the waveguide modes for different values of W_{Si} (200 nm, 580, and 1200 nm). Consistent with previous work on hybrid modes, [115] as the width of the waveguide increases from 200 nm to 1200 nm, the mode continuously shifts from being predominantly confined in the

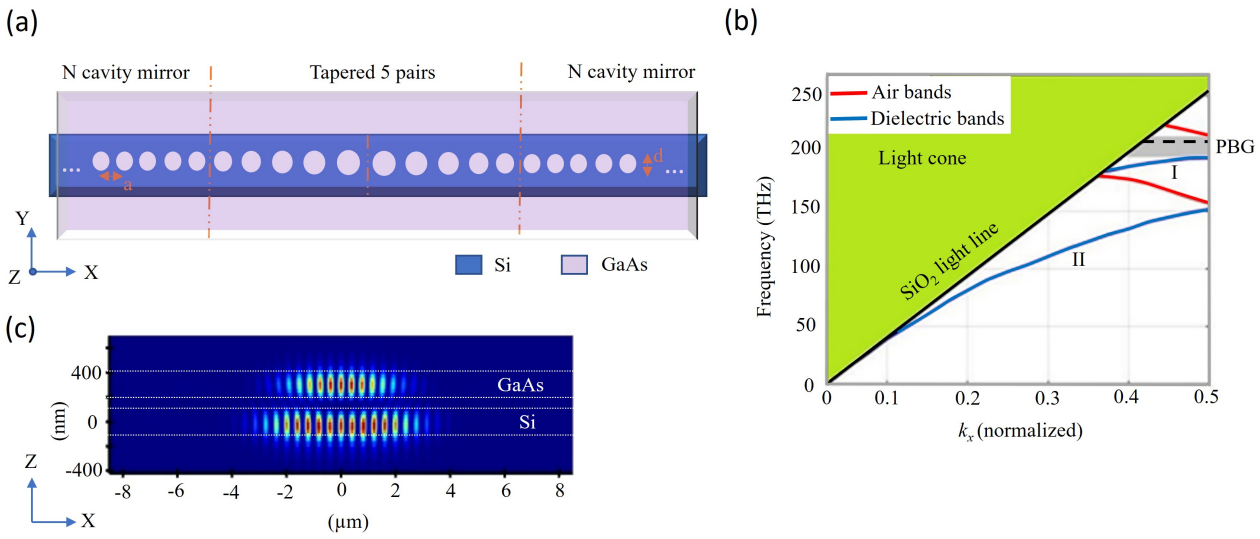


Figure 4.2: (a) Schematic diagram of the silicon waveguide cavity design, which features a total of 16 cavity pairs, including $N = 11$ ellipsoidal cavities on both sides and 5 centered pairs of tapered ellipsoids as defects. (b) The FDTD calculated band structure of the hybrid Si-GaAs device. The grey shaded area is the photonic bandgap (PBG), which corresponds to the difference between the calculated air bands (red curves) and dielectric bands of the silicon and GaAs (blue curves marked I and II, respectively). Here, k_x is related to wavevector $k = k_x(2\pi/a)$, which is a function of the reciprocal lattice parameter a specified by the Bloch boundary condition. The black line denotes the SiO_2 light line, and the horizontal black dashed line in PBG indicates the cavity resonance frequency at 197.68 THz. (c) The fundamental mode field ($|E|$) profile in the hybrid Si-GaAs cavity obtained using the 3D FDTD method. The white dashed lines denote the silicon and GaAs layers (220 nm and 200 nm thick, respectively), which are separated by a 60 nm spacer.

GaAs slab to being confined in the silicon waveguide. Figure 4.1d shows the confinement factor in the silicon or GaAs region, defined as $\frac{\int_{Si\ or\ GaAs}|E|^2dA}{\int_{total}|E|^2dA}$, which shows the gradual shift between the two materials. The three vertical dashed lines labeled I, II, and III, correspond to the widths plotted in Fig. 4.1c.

Without the GaAs layer, this device structure would lead to a highly localized mode within the silicon waveguide. But adding the GaAs layer causes the mode to hybridize. The key to designing a cavity mode for the hybrid Si-GaAs device is to carefully select the width W_{Si}. If this width is too large, most of the mode will be confined in the silicon, leading to strong optical confinement but poor overlap with the GaAs active material. In contrast, if W_{Si} is smaller, the majority of the hybrid mode will be confined to the GaAs active material where it can experience large gain and nonlinearity. But in this latter case, the effective index contrast of the hybrid Si-GaAs photonic crystal will be low, which will result in poor optical confinement and low quality factors. To balance these conflicting requirements, we set the width of the waveguide to be 580 nm, as it enables a hybrid mode that is nearly equally confined in both the silicon and GaAs (label II in Figure 4.1c, d).

Next, to design the cavity, we first analyze a periodic photonic crystal in the silicon waveguide, specifically the mirror region of Figure 4.2a. We choose an ellipsoidal cavity for the mirror with a lattice period a of 380 nm and radii of 140 nm and 130 nm for the major and minor ellipsoidal axes, respectively. We then calculate the photonic band structure by performing three-dimensional Finite Difference Time Domain simulations (ANSYS FDTD solution) with Bloch boundary conditions. Figure 4.2b shows the photonic band structure, which features a sufficiently wide photonic bandgap of 8.5 THz that spans within a telecom range of 192 THz to 200.5 THz (grey-shaded region).

In order to create a cavity mode, we start with a photonic crystal waveguide featuring 16 pairs of ellipses to which we introduce a defect. As shown in Figure 4.2a, the defect is composed of a taper where the major and minor axes of the five centered pairs of ellipses linearly increase from 140 nm to 150 nm and 130 nm to 140 nm, respectively, toward the center of the waveguide. This design results in a cavity resonance wavelength of 1516.53 nm, which is depicted as the black dashed line in the photonic bandgap plot in Figure 4.2b. Figure 4.2c plots the electric field profile $|E|$ of this hybrid Si-GaAs cavity design at the resonance wavelength, which reveals a fundamental cavity mode that extends in both the silicon waveguide and GaAs slab. The mode is highly localized in the cavity region and has a substantial overlap with both the silicon and GaAs, thus achieving a hybrid localized photonic crystal cavity mode. From the 3D-FDTD simulations, we calculate the mode volume to be $V_m \approx 2(\lambda/n)3$ and the quality factor to be $Q = 1.53 \times 10^4$. Based on this quality factor and mode volume, the theoretically predicted maximum Purcell factor is 794.17 (see Appendix C.2), which suggests the hybrid cavity design is a promising candidate for the enhancement of spontaneous emission. [141] This hybrid cavity mode should facilitate the interaction with the quantum dots embedded in the GaAs, which can be used to achieve nanolasing and optical bistability in silicon, as we discuss in the following sections.

4.3 Lasing simulation

To numerically simulate lasing from the hybrid cavity, we incorporate four layers of InAs quantum dots at a planar density of $4\times10^{10}/cm^2$, with each layer separated by 50 nm intervals in the GaAs slab. [142] The quantum dots can be described as a gain material using a four-level atom model [136, 137] (see Appendix C.3). To investigate the lasing capabilities of the

hybrid Si-GaAs cavity, we use 3D-FDTD to calculate the cavity output power as a function of the input pump power (L-L curve) using a pump-probe technique. In our numerical simulation, we employ a 750 nm wavelength pump to excite the active material with a pulse width of 4.5 ps and a broadband probe of two orders of magnitude smaller than the pump amplitude centered at the hybrid cavity resonance wavelength of 1516.53 nm to observe the lasing. Figure 4.3 plots the resulting FDTD calculations of the hybrid cavity's output lasing power (black circles), which we then fit using the cavity laser rate-equation model (see Appendix C.4) given by [143]

$$P_{in} = \frac{\hbar\omega\gamma}{\beta\eta_{in}}\left[\frac{p}{1+p}\left(1+\zeta\right)\left(1+\beta p\right)-\zeta\beta p\right] \tag{4.1}$$

Here, P_{in} is the input pump power, ω is the cavity resonance frequency, $\gamma = \omega/Q$ is the cavity decay rate, and β is the spontaneous emission coupling ratio. We define the cavity photon number as $p = P_{out}/\hbar\omega\gamma\eta_{out}$, where η_{out} is the output collection efficiency of the laser. Additionally, η_{in} is the pumping efficiency, and ζ is the cavity photon number at transparency.

From Equation 1, we calculate several log-log L-L curves (solid curves in Figure 4.3) corresponding to different spontaneous emission coupling ratios (0.3, 0.65, and 1) and find the FDTD lasing data is best fit by a coupling ratio of 0.65 (orange curve). We then calculate the lasing threshold power from the condition when there is an average of one photon in the cavity ($p = 1$). Using this value of p in Equation 1, we obtain a threshold power of $P_{th} = 156$ nW, which is shown by the vertical dashed line in Figure 4.3. We also observe an increase in the slope of the log-log curve near the lasing threshold in the FDTD data (black circles), which is a hallmark feature of lasing. [144, 145] Our simulation demonstrates a lower lasing threshold compared to other devices using hybrid Si-III/V materials, [85, 127–130] which have previously reported a

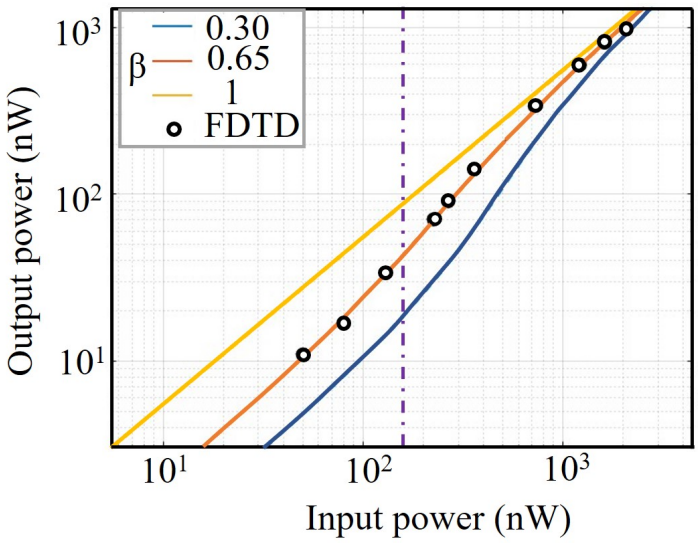


Figure 4.3: Using 3D FDTD, we calculate the input power versus output power (log-log L-L curve) of the hybrid Si-GaAs cavity nanolaser (black circles) and fit the results using a rate equation model (Equation 1) as shown by the orange curve, which corresponds to a spontaneous emission coupling ratio of $\beta = 0.65$. The blue and yellow solid curves are also plotted using the rate equation with spontaneous emission coupling ratios of $\beta = 0.3$ and 1, respectively. The vertical dashed line is the lasing threshold obtained from the rate equation fit to the FDTD data.

lasing threshold power as low as 1 μW. [130]

4.4 Bistability simulation

Optical bistability, a nonlinear optical phenomenon, can be defined as an optical system possessing two different output states corresponding to the same input intensity. Such bistability has been demonstrated for a wide range of applications, including all-optical switches, [146] memories, [147] optical logic gates, [148] and optical transistors. [149] Our hybrid cavity can operate as a low-power bistable device by employing optical nonlinearity such as the saturable absorption of quantum dots. As saturable absorption does not require a gain material, we can simulate the bistability response of the quantum dots in the hybrid Si-GaAs cavity using a two-level one electron numerical model [150, 151], which also enables faster device simulation.

To simulate the optical response of the InAs quantum dots in the GaAs region of the hybrid cavity, we incorporate the Maxwell-Bloch equations into numerical FDTD simulations using the method described by Shih-Hui Chang and Allen Taflove. [136] The Maxwell-Bloch equations describe the response of saturable absorbers to an incident electric field.

$$\frac{dN_{11}}{dt} = -i\frac{\Omega}{2}(\chi^*_{SA} - \chi_{SA}) + \gamma N_{22} \tag{4.2}$$

$$\frac{dN_{22}}{dt} = i\frac{\Omega}{2}(\chi^*_{SA} - \chi_{SA}) - \gamma N_{22} \tag{4.3}$$

$$\frac{d\chi_{SA}}{dt} = -(\beta + i\Delta)\chi_{SA} - i\frac{\Omega}{2}(N_{22} - N_{11}) \tag{4.4}$$

Here, N_{11} and N_{22} are the population densities of the two-level atoms for the ground and excited states, $\Omega = \mu E/\hbar$ is the optical Rabi frequency, and μ is the transition matrix elements of the two-level atom. We define the detuning frequency as $\Delta = \omega_0 - \omega$, while ω_0 and ω are the resonant frequency and incident light frequency. We also describe the atomic decay rate as $\gamma = \gamma_{non} + \gamma_{rad}$, where γ_{non} is the nonradiative decay rate and $\gamma_{rad} = \frac{\mu^2\omega^3}{3\pi\hbar\epsilon_0(1+\chi_D)c^3}$ is the radiative decay rate. Finally, $\beta = \gamma/2 + 1/T_2$, while T_2 is the dipole dephasing time.

For the simulation parameters, we set a layer of InAs quantum dots in the GaAs region of the hybrid cavity at a planar quantum dot density of $N = 7 \times 10^{10}/cm^2$. [152] We set the decay rates of the quantum dots to their room temperature values of γ_{rad} = 1 GHz [153] and γ_{non} = 1 GHz, [154] and the dephasing time to $T_2 = 300$ fs. [155] In order to observe the bistability effect in the FDTD simulations, we specify a continuous wave (CW) input source at the cavity resonant wavelength of 1516.53 nm at one end of the hybrid cavity. Here, we define the source input power as a function of time such that the input power increases and decreases for the same

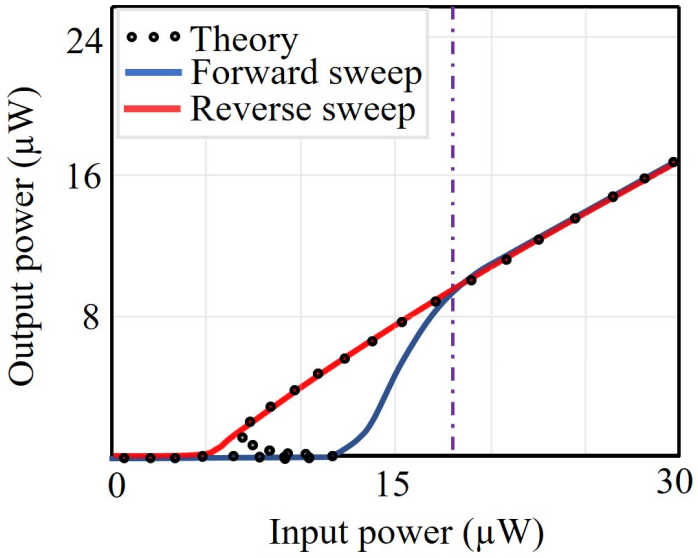


Figure 4.4: Output power vs. input power at the resonance wavelength 1516.53 nm of the hybrid Si-GaAs cavity, featuring quantum dots as saturable absorbers in the GaAs slab. The blue and red curves are the forward and reverse sweeps of the input power, respectively, while the black circles represent the theoretical bistability curve. The purple dashed line is the bistability threshold.

period. [156] Finally, we calculate the output power at the other end of the hybrid cavity to observe the difference in the nonlinear behavior for increasing and decreasing source powers.

Figure 4.4 plots the simulated optical response of the saturable absorbers in the hybrid Si-GaAs cavity, which demonstrates hysteresis in the output power depending on whether the input power increases or decreases (blue and red curves, respectively). This behavior indicates bistability, in which the cavity exhibits two stable states of operation. The FDTD simulations also demonstrate good agreement with the theoretical bistability curve (black data points in Figure 4.4), where the output power is a bistable function of the cavity input at a steady state [157, 158] (see Appendix C.5). The threshold power of the optical bistability corresponds to the transition of the output power between the two stable states in the hysteresis loop, which occurs at 18.1 μW (vertical purple dashed line). Our design provides a comparable threshold as observed in silicon photonic crystal cavities [147, 159, 160] and ring cavities. [161–163] The low bistability

threshold of this hybrid cavity design is promising for various silicon photonic applications at telecom wavelengths requiring low-power optical nonlinearity.

4.5 Summary and discussion

In summary, we have shown that low power threshold lasing and optical bistability can be achieved using a new Si-GaAs hybrid cavity design. In this approach, the cavity is patterned in the silicon waveguide while the GaAs slab features quantum dots that are optically active at telecom wavelengths. This hybrid device does not require careful alignment and could be fabricated using the simple pick-and-place transfer printing method. [164, 165] Moreover, the integration of Quantum Dots (QDs) within a hybrid cavity in III-V semiconductor materials holds great promise in quantum photonics. This technique could enable large-scale efficient integration of quantum emitters onto a silicon chip, offering exciting prospects for on-chip quantum applications such as quantum communication, computing, and information processing. Additionally, the device can operate at different frequencies by changing the cavity design parameters, with optimization enabling further improved performance (see Appendix C.6 and C.7). Our work represents a critical step toward the efficient heterogeneous integration of silicon and III-V materials for future low-power silicon nanophotonics.

Chapter 5: Conclusions and future directions

In this thesis, we have demonstrated several photonic components for hybrid integration with silicon photonics. In Chapter 2, an efficient fiber-coupled single-photon source at the telecom C-band using InAs/InP quantum dots in a tapered nanobeam was demonstrated [166]. We utilized PDMS transfer printing lithography to transfer our tapered nanobeam arrays onto a silicon chip, enabling direct access of photons to a lensed fiber. TThe tapered nanobeam structure featured a near Gaussian far-field emission, which was mode-matched to a lensed fiber, resulting in a collection efficiency of up to 65% to a single-mode fiber. Using this approach, single-photon count rates of 575 $\pm$ 5 Kcps and single-photon purity g (2) (0) = 0.015 $\pm$ 0.003 were demonstrated. Additionally, Hong-Ou Mandel interference from emitted photons was demonstrated with a visibility of 0.84 $\pm$ 0.06. From these measurements, a photon coherence time of 450 $\pm$ 20 ps was determined, only 7.9 times away from the lifetime limit. This work represents an important step towards developing telecom C-band single-photon sources emitting bright, pure, and indistinguishable photons, indispensable for realizing long-distance fiber-based quantum networks. Future studies may focus on integrating these C-band indistinguishable photons into silicon waveguides for hybrid integration.

In Chapter 3, we investigated atomic layer-based surface passivation of InP photonic crystal cavities to improve the brightness of the embedded InAs quantum dots [58, 167]. Using Al_2O_3

atomic layer deposition the quality factor of the InP nanobeam cavities was significantly improved by terminating surface states and dangling bonds. Additionally, by changing the deposition thickness, precise tuning of the cavity mode wavelength was achieved without compromising the quality factor. This Al_2O_3 atomic layer deposition approach holds great promise for improving the quality factor of nanobeam cavities that are well-suited for integration with silicon photonics. Ongoing and future research aims to utilize surface-passivated cavities to enhance the brightness of the quantum dots further.

Finally, Chapter 4 proposed a new hybrid integration technique of III-V materials with silicon photonics. Using 3D finite-difference time-domain simulations, we proposed a hybrid Si-GaAs photonic crystal cavity design operating at telecom wavelengths, which could be fabricated without the need for careful alignment [78, 168]. The hybrid cavity consists of a patterned silicon waveguide coupled to a wider GaAs slab featuring InAs quantum dots. By changing the width of the silicon cavity waveguide, the hybrid modes could be engineered, as well as the degree of coupling to the active material in the GaAs slab. This provided the ability to tune the cavity quality factor while balancing the device's optical gain and nonlinearity. This design demonstrated cavity mode confinement in the GaAs slab without directly patterning, enabling strong interaction with the embedded quantum dots for applications such as low-power-threshold lasing and optical bistability (156 nW and 18.1 μW, respectively). This heterogeneous integration of an active III-V material with silicon via a hybrid cavity design suggests a promising approach for achieving on-chip light generation and low-power nonlinear platforms. Future directions could include experimental realization by transfer printing of the GaAs slab using PDMS stamp onto a pre-patterned silicon waveguide for low-power lasing and nonlinearity. Additionally, the hybrid cavity could be helpful for large-scale integration of single-photon sources in silicon

photonics.

The results presented in this dissertation represent advancements in integrating quantum dot emission in fiber optics. Furthermore, our research marks a promising stride towards the alignment-free hybrid integration of III-V materials with quantum dots into silicon photonics. These findings pave the way for developing highly efficient and versatile photonic devices for quantum information processing and other applications.

Appendix A:

A.1 Tapered Nanobeam design at 1550 nm

Figure A.1a illustrates the nanobeam design featuring an adiabatic taper with a thickness of 280 nm. Based on 3D finite-difference time-domain (FDTD) simulations, we designed the nanobeam mirror with dimensions of 560 nm width and 12 air holes with a periodicity of 440 nm. The nanobeam features varying hole radii, with the first 10 holes at 110 nm and the last two at 95 nm and 80 nm, respectively. To design the nanobeam taper, we utilize 3D finite-

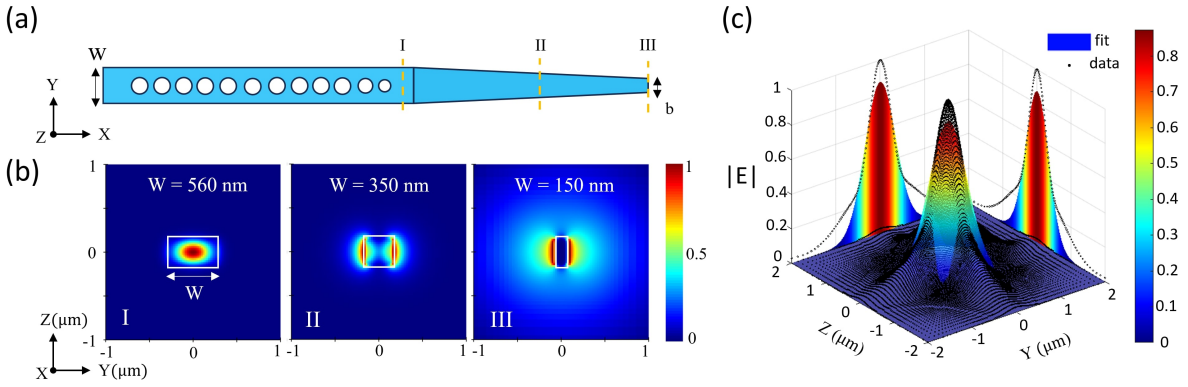


Figure A.1: (a) A schematic diagram illustrating the design of the InAs/InP nanobeam mirror with an adiabatic taper, where yellow dashed lines labeled as I-III indicate the positions of cross sections along the nanobeam taper. (b) A white rectangular box depicts the electric field intensity ($|E|$) profile for various cross sections (I-III) of the InAs/InP nanobeam taper. (c) The 3D far-field ($|E|$) profile 500 nm away from the nanobeam taper edge. Here, the black dots represent the far-field profile of the nanobeam, and the color-coded surface map represents the Gaussian mode of the single-mode fiber.

difference time-domain (FDTD) simulations to analyze the electric field intensity profiles and far-field emission patterns of the nanobeam taper at 1550 nm, as shown in Figure A.1b and c. In Figure A.1b, the electric field intensity ($|E|$) is depicted for various cross sections labeled as I-III along the nanobeam taper. The taper width decreases linearly from 560 nm to 150 nm while maintaining a fixed nanobeam thickness of 280 nm over a length of 15 μm. As the taper width decreases, the waveguide mode gradually decays evanescently towards the outside of the waveguide, as observed at position III when the taper width is 150 nm.

The tapered structure expands the propagation mode and results in directional Gaussian-shaped emission from the tapered edge, as demonstrated in the 3D FDTD simulation represented by black points in Figure A.1c. The efficiency of collecting single photons depends on the overlap between the emission from the nanobeam taper and the Gaussian mode profile of the single-mode optical fiber. We utilized nonlinear least-squares fitting to approximate the nanobeam taper field profiles with Gaussian functions, as shown by the color-coded surface map of Figure A.1c. To estimate the fiber coupling efficiency, we calculated the Gaussian overlap, using the following equation [54]

$$\eta_{fiber} = \frac{|\int\int E_{nb}E_f^* dxdy|^2}{\int\int |E_{nb}|^2 dxdy \int\int |E_f|^2 dxdy} \tag{A.1}$$

where Enb and Ef represent the field intensity of the nanobeam emission taper and fiber mode, respectively. Based on this equation, we calculate an 88% overlap between the field emission from the nanobeam taper and the fiber mode.

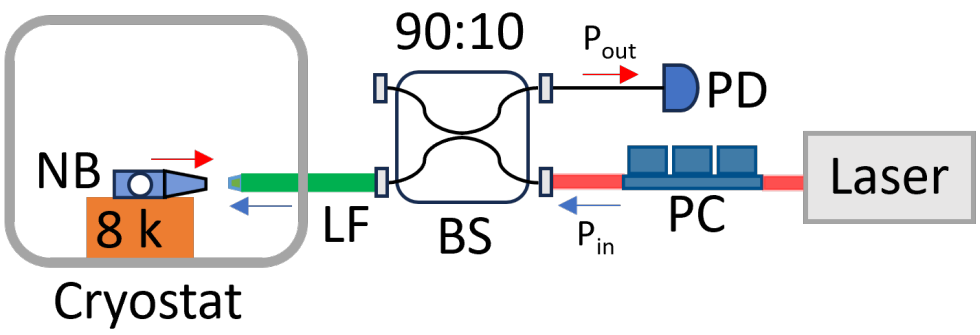


Figure A.2: Schematic diagram of the reflectivity measurement setup. Here, NB: nanobeam, LF: lensed fiber, BS: beam splitter, PM: power meter, and PC: polarization controller.

A.2 Reflectance measurement

Figure A.2 illustrates the setup for measuring reflectivity to determine the coupling efficiency from the nanobeam to the lensed fiber. We assumed equal coupling-in and coupling-out efficiencies between the nanobeam and the lensed fiber. A laser with a power P_{in} was injected into the lensed fiber, and the back-reflected light was measured as P_{out} using a power meter. This measurement was performed with a 90:10 beam splitter having a transmission of T = 83%. The coupling efficiency (η) is defined as

$$\eta = \sqrt{\frac{P_{out}}{TP_{in}}} \tag{A.2}$$

A.3 Lifetime calculation

We determined the emitter's lifetime by calculating the decay rate of the antibunching dip observed in Figure 2.4a and Supplementary Figure A.3a, b. Supplementary Figure A.3a, b exhibit autocorrelation values of $g^{(2)}(0) = 0.133 \pm 0.004$ and $g^{(2)}(0) = 0.149 \pm 0.005$ at pump powers of 3 μW and 5 μW, respectively. The measured $g^{(2)}(\tau)$ was fitted to a two-level emitter second-order

autocorrelation in the form of $g^{(2)}(\tau) = 1 - (1 - g^{(2)}(0))e^{(-\gamma_1|\tau|)}$. The decay rate constant γ_1 depends on the excited state lifetime τ_{rad} at pump power P, given by $\gamma_1 = 1/\tau_{rad}(1+\alpha P)$, where τ_{rad} is the excited state lifetime, P is the excitation power, and α is a fitting parameter [59, 60]. As the pump power increased, the decay rate constant also increased, as illustrated in Figure S3c. Fitting the data to a linear function, we obtained the excited state lifetime $\tau_{rad} = 1.870.03$ ns at zero power.

A.4 Second-order autocorrelation using pulsed laser excitation

In addition to continuous wave excitation, we conducted second-order autocorrelation measurements for an above-band 780 nm pulsed laser with a 40 MHz repetition rate and a 300 ps pulse width. Autocorrelation histograms were measured at power levels of 250 nW and 5 μW, resulting in $g^{(2)}(0) = 0.135 \pm 0.01$ at 250 nW and $g^{(2)}(0) = 0.270.02$ at 5 μW, as illustrated in Figure A.4a, b. Figure A.4c depicts the count rate from the emitter as a function of the pump intensity. The raw counts vs. power and the corrected fit of $g^{(2)}(0)$ (shown in Figure A.4d) are presented with

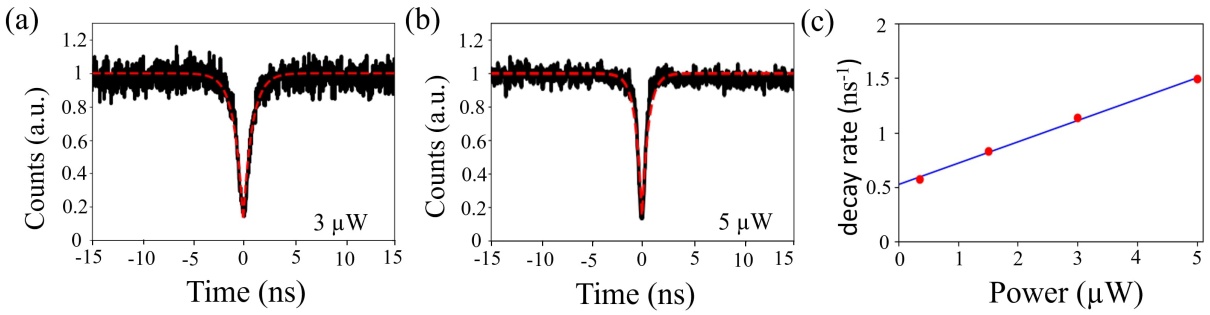


Figure A.3: (a, b) Autocorrelation histograms measured at 780 nm under above-band excitation with power levels of (a) 3 μW and (b) 5 μW. The black lines represent the measured data, while the red dashed lines depict curves fitted to the double-sided exponential decay function. (c) The decay rate constant γ_1 at different pump powers obtained from the $g^{(2)}(\tau)$ histogram fits in (a) and (b) and Figure 3a of the main manuscript. The solid blue line is a fit to a linear function.

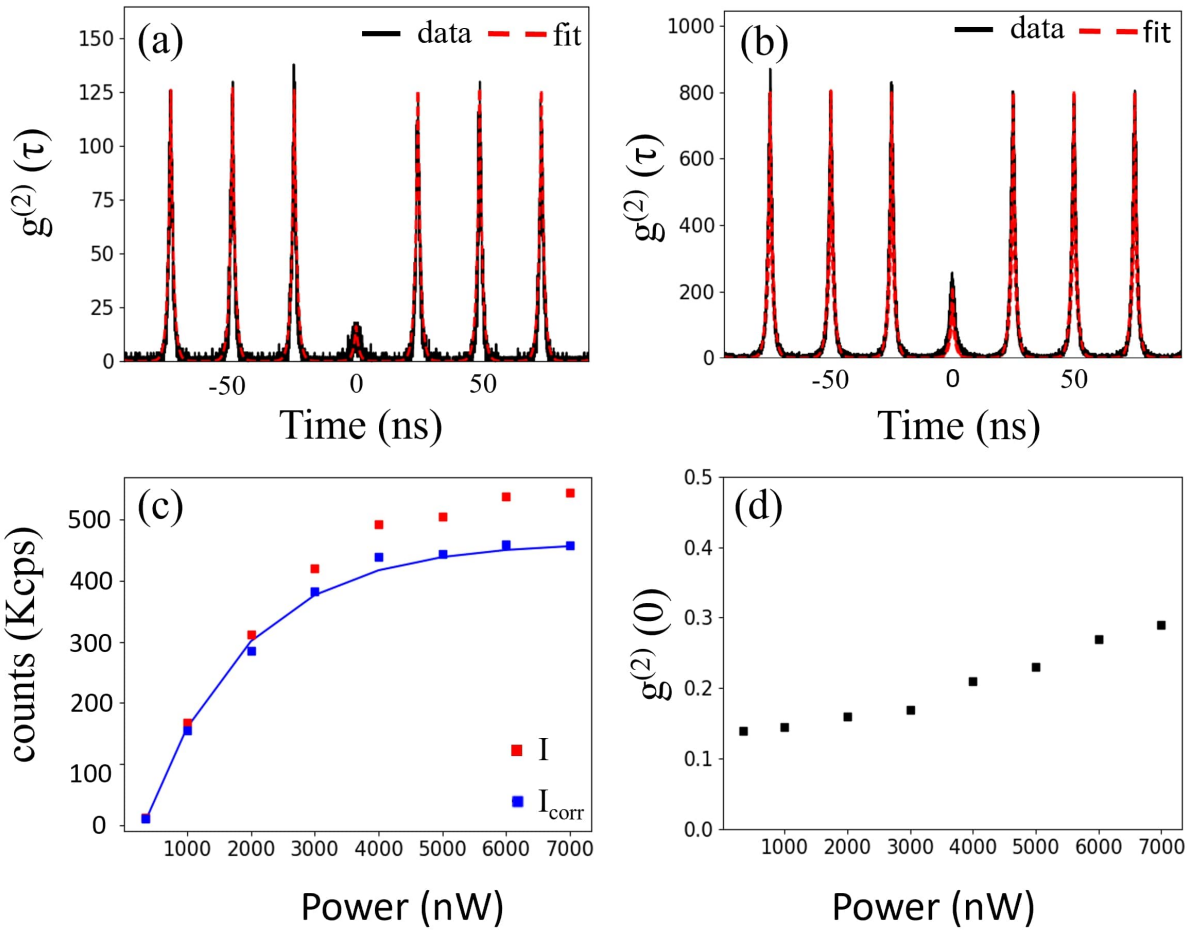


Figure A.4: (a, b) Autocorrelation histogram measurements using at 780 nm laser under above-band pulsed laser excitation with power levels of (a) 250 nW and (b) 5 μW. The black lines represent the measured data, while the red dashed lines depict curves fitted to the double-sided exponential decay function. (c) Detected count rates (red squares) and $g^{(2)}(0)$-corrected count rates (blue squares) as a function of the pump power. The blue line corresponds to a fit with fitting parameters Psat = 1.6 μW and $I_{sat} = 452 \pm 4$ Kcps. (d) $g^{(2)}(0)$ as a function of the pump power.

fitting parameters Psat = 1.6 μW and Isat = 452 ± 4 Kcps.

A.5 Photon budget and source efficiency

We conducted a comprehensive photon budget analysis to assess the source efficiency. The total end-to-end efficiency of the system was 1.13 ± 0.01%, which was determined by dividing

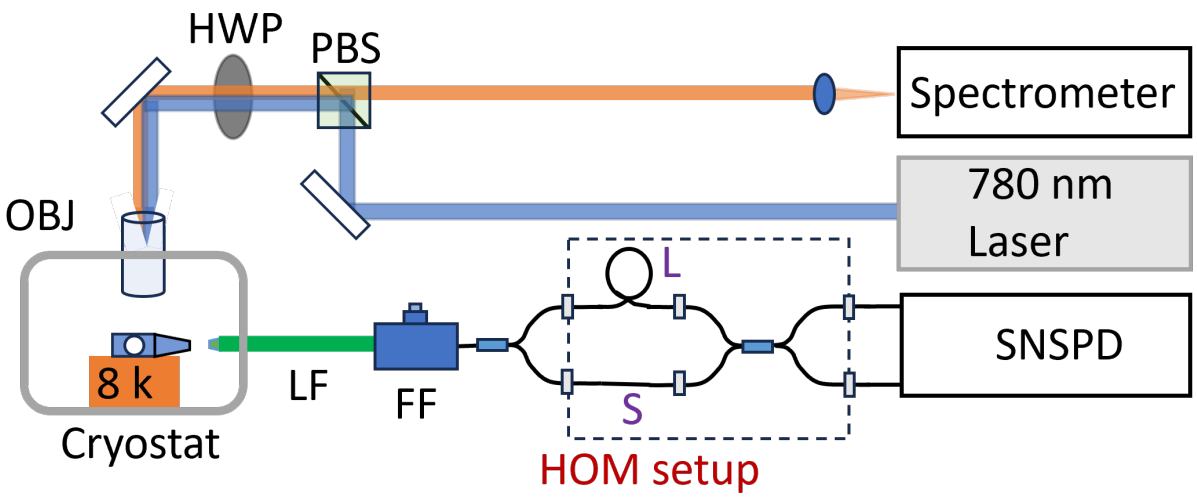


Figure A.5: Hong-Ou-Mandel interferometer setup. The components include LF: lensed fiber, FF: fiber filter, HWP: half waveplate, PBS: polarizing beam splitter, OBJ: objective lens, and SNSPD: superconducting nanowire single-photon detector. Here, L and S represent the long and short fiber paths introduced to create a time difference of 4.36 ns.

the count rate of the emitter at saturation ($I_{sat} = 452 \pm 4$ Kcps, Figure A.4c) by the laser pulse repetition rate of 40 MHz. We measured the efficiency of the individual system components and found (i) the lensed fiber coupling efficiency, η_F = 0.6, (ii) the fiber-based spectral filter transmission efficiency, η_{SF} = 0.526, (iii) the 50:50 beam splitter transmission efficiency, η_{BS} = 0.44, (iv) the fiber cable transmission efficiency, η_{FC} = 0.82, and (v) the SNSPD detection efficiency η_{SNSPD} = 0.8. Utilizing these component transmission efficiencies, the efficiency of the lensed fiber was computed as $B_{fib} = \frac{I_{sat}}{\eta_F \eta_{SF}}$ = 3.58 ± 0.03% , and the source efficiency was determined to be $B_{fib} = \frac{I_{sat}}{\eta_F \eta_{SF} \eta_{BS} \eta_{FC} \eta_{SNSPD}}$= 12.41 ± 0.09%.

A.6 Hong-Ou-Mandel interferometer setup

In the Hong-Ou-Mandel two-photon interference measurements, excitation light was introduced from the top of the sample and focused using an above-band laser emitting light at a wavelength

of 780 nm, consistent with Figure 2.3a in the main manuscript. After collection from the lensed fiber, the light underwent initial filtration using a 0.2 nm grating tunable fiber filter designed for single photon counting. Fiber-type unbalanced Mach-Zehnder interferometers were inserted at collection paths within the dashed-line boxes shown in Figure A.5. These interferometers featured a 4.36 ns time delay on one path relative to the other, effectively delaying generated single photons within the first fiber-type beam splitter before colliding at the second fiber-type beam splitter. For the Hong-Ou-Mandel measurement, a fiber-type polarization controller and polarization-maintained fibers were utilized to prepare single photons at both parallel and orthogonal polarizations, with the flexibility to interchange them independently. Single photon count rates and second-order autocorrelation measurements were conducted using a single optical fiber on the collection path. The same setup was used, excluding the dashed-line boxes in Figure A.5a, to conduct the Hanbury Brown and Twiss-type measurements and calculate the photon count rate.

Appendix B:

B.1 Nanobeam cavity design

We use 3D finite-difference time-domain (FDTD) simulations to calculate the cavity quality factor for different outcoupling mirror numbers (NR). Figure B.1 shows the quality factor for different out-coupler mirror numbers (NR) for fixed NL = 13. Increasing the NR reduces the scattering loss, and the quality factor increases and saturates at $Q = 9.60 \times 10^5$ for NR$\geq$ 13. Once we optimize the cavity quality factor for NL = NR = 13, we make the cavity one-sided by reducing the number of NR to make it partially reflective. We expect the critical coupling

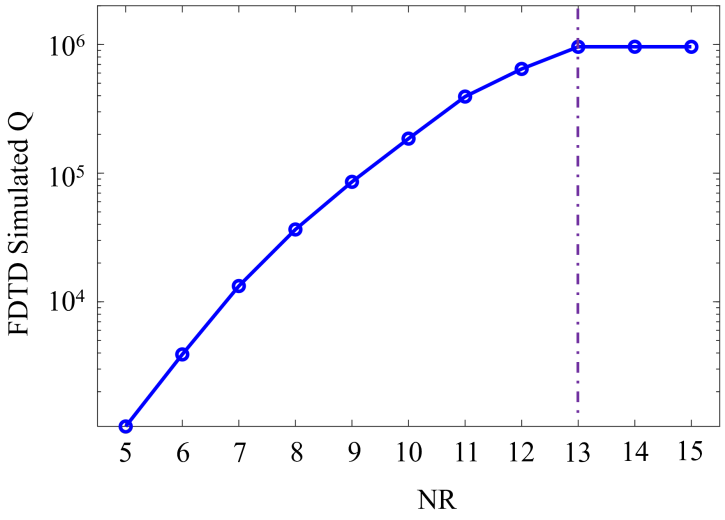


Figure B.1: FDTD calculated quality factor (Q) for different outcoupling mirrors (NR). Here, the vertical dashed line corresponds to NR = 13.

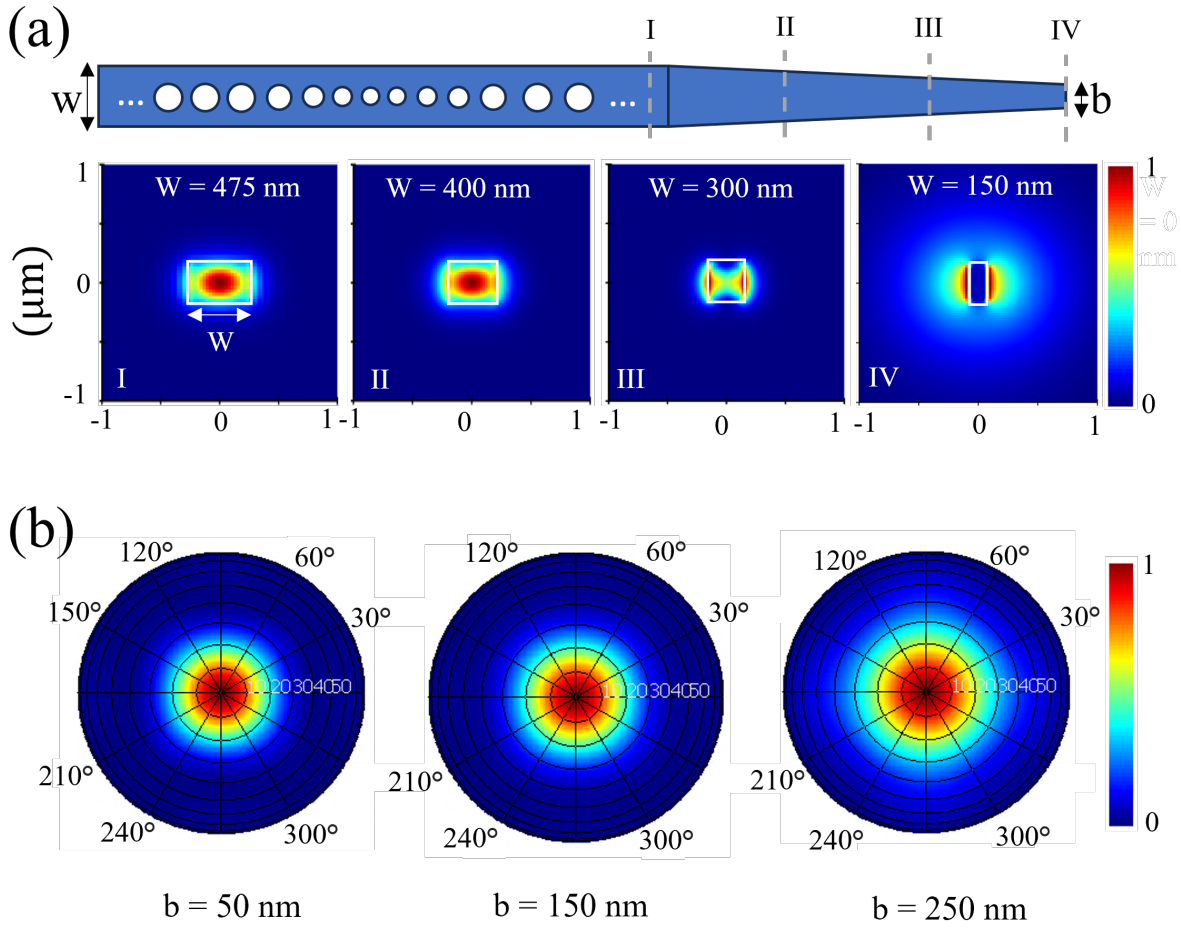


Figure B.2: FDTD calculated quality factor (Q) for different outcoupling mirrors (NR). Here, the vertical dashed line corresponds to NR = 13.

condition for the simulated cavity to be between NR = 8 and NR = 10. However, the experimental critical coupling could be for a lower NR $\leq$ 8 due to scattering and material losses.

B.2 FDTD simulation of nanobeam taper at 1300 nm

We analyze the mode profile of nanobeam taper at different positions marked in Figure B.2. We linearly reduce the taper width from W = 475 nm to b = 150 nm while the thickness of the nanobeam is fixed at 280 nm. The tapered structure is 15 μm long, expands the propagating mode, and generates directional Gaussian-shaped emission from the tapered edge [54,59]. Figure B.2(a)

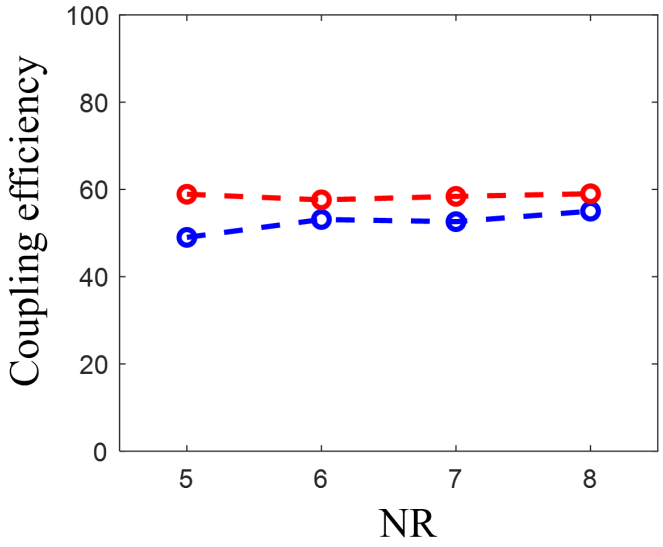


Figure B.3: Coupling efficiency as a function of the number of out-coupler mirrors (NR), ranging from 5 to 8, both before (blue circle) and after (red circle) atomic layer deposition.

depicts this expansion, showing the calculated electric field intensity ($|E|$) for different segments with widths of W = 475 nm, 400 nm, 300 nm, and 150 nm along the nanobeam taper. As the taper width decreases, the waveguide mode at W = 475 nm gradually shifts towards the outside of the taper, and at W = b = 150 nm, there is no mode confinement inside the taper. Furthermore, we present the far-field profile from the taper edge for various taper edge widths (b = 50 nm, 150 nm, and 250 nm) in Figure B.2b while keeping the taper length unchanged.

B.3 Coupling efficiency before and after ALD

We also compared the coupling efficiency before and after the atomic layer deposition process. We use the off-resonance count differences of cavities with NR = 5 to 8 to calculate coupling efficiency. We employ the same excitation power utilizing a stabilized tungsten-halogen lamp before and after 6 nm Al_2O_3 deposition. Figure B.3 illustrates the effect of 6 nm atomic

layer deposition on coupling efficiency for the nanobeam. After the atomic layer deposition, we observed an average improvement of approximately 5.9%. This enhancement can be attributed to the reduction of scattering loss in the nanobeam and taper region.

B.4 Quality factor fitting equation

To assess the cavity quality factor (Q), we employed a Lorentzian fit on the reflection spectrum of the nanobeam cavity. The Lorentz function is expressed as:

$$L(x) = \frac{1}{\pi} \frac{1/2\gamma}{((\lambda - \lambda_0) + (1/2\gamma))} \tag{B.1}$$

Here, λ_0 represents the center wavelength, and γ is the parameter specifying the linewidth at half the maximum intensity ($FWHM$). The calculation of the quality factor (Q) from the Lorentz fit is defined as $Q = \lambda_0/FWHM$.

B.5 Quality factor analysis

We utilized 3D FDTD Ansys Lumerical to simulate the cavity quality factor for different cavity hole radii to get insight into the quality factor change in the experiment. Figure B.4a shows the FDTD calculated quality factor for reducing cavity hole radius from 2 to 10 nm without atomic layer deposition. The quality factor decreases due to the cavity hole radius decreasing from the design radius (92 nm).

In Figure B.4b, we plot the experimental quality factors of the reflectance spectrum shown in Figure 3.4a for different atomic layer deposition thicknesses. Initially, the quality factor

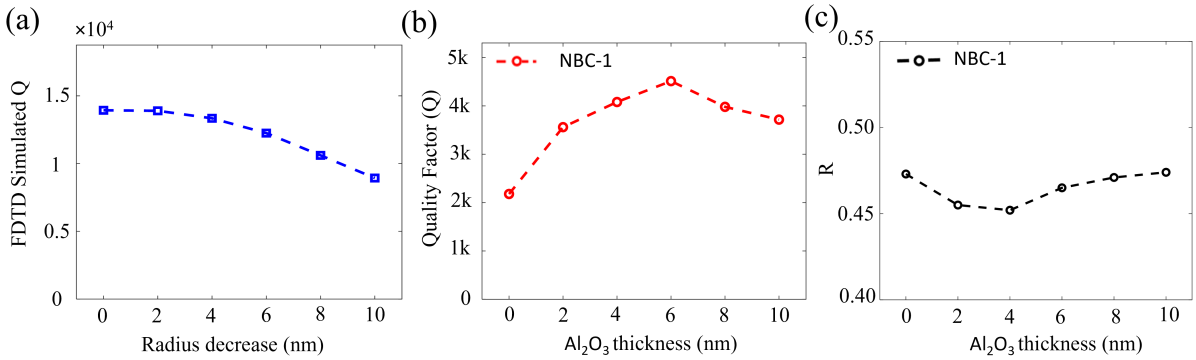


Figure B.4: (a) 3D FDTD simulated quality factors (Q) of the nanobeam cavity for cavity hole radius decrease. (b) The experimental quality factor and (c) reflection coefficient (R) for different atomic layer deposition thicknesses correspond to Figure 3.4a.

experiences an increase with the increase in atomic layer deposition due to surface passivation and a reduction in scattering loss. However, the cavity hole radius decreases with the higher thickness of atomic layer deposition, and the quality factor follows the decreasing trend shown in Figure B.4a. The quality factor undergoes a significant degradation beyond a deposition thickness of ($>$10 nm) due to further decreased cavity hole radius. In addition to the quality factor, in Figure B.4c, we plot dip variation, or the reflection coefficient (R) after normalizing the reflectance spectrum shown in Figure 3.4a.

B.6 Resonance wavelength change of nanobeam cavity

We also use 3D-FDTD to calculate wavelengths for different thicknesses of conformal atomic layer deposition [169]. In the simulation, we incrementally added 2 nm of Al_2O_3 atomic layer on all the surfaces of the nanobeam cavity and in the cavity holes, which reduces the cavity radius, and calculated the wavelength change from the cavity resonance wavelength of 1310 nm. Figure B.5a presents the 3D-FDTD calculated cavity wavelength change for different Al_2O_3 atomic layer deposition thicknesses. The wavelengths increase consistently with the increase of

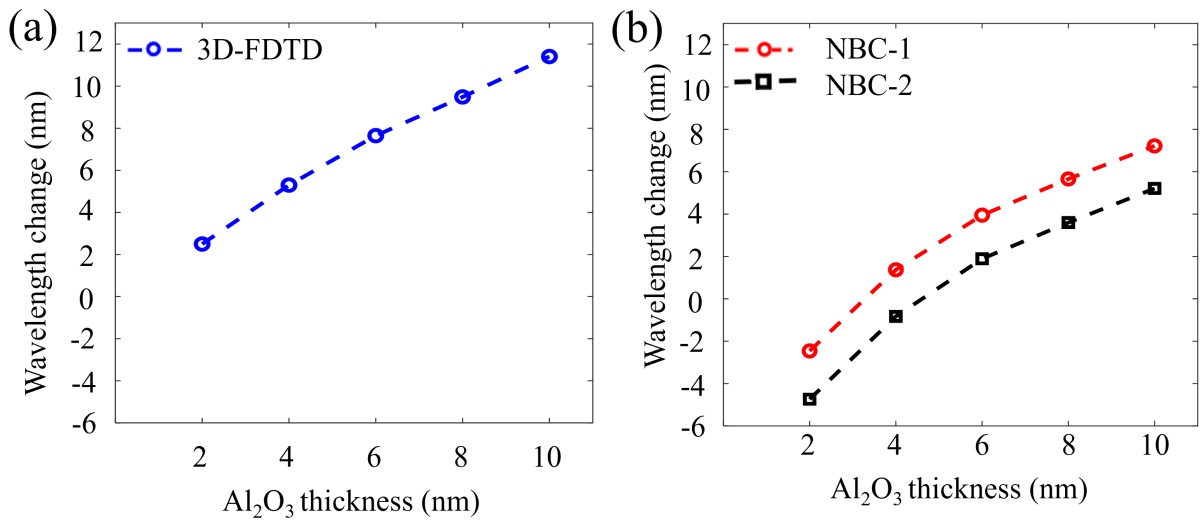


Figure B.5: Wavelength change from the cavity resonance wavelength (a) 3D-FDTD simulation of expected wavelength shifts and (b) experimental wavelength change for two different cavities for different atomic layer deposition thicknesses.

atomic layer deposition thickness. We also saw the same increasing trend for two nanobeam cavities in the experiment. Here, we note that the wavelength changes in Figure B.5b for cavity 1 (red curve) correspond to the reflectance spectra of measurement data shown in Figure 3.4a of the main manuscript. However, we found an initial wavelength drop in an experiment during the atomic layer deposition process.

To understand the experimental wavelength drop, we measured 24 nanobeam cavities before and after conditioning in an atomic layer deposition chamber at 150 °C and 5 mbar. The sample was placed for 15 minutes and unloaded before the atomic layer deposition. We found this conditioning procedure led to an average wavelength reduction of 7 ± 2.6 nm in the cavity resonance wavelength without significantly changing the quality factor. We believe the high-temperature treatment in the atomic layer deposition chamber could remove native oxide [104, 105], contributing to the observed wavelength drop.

B.7 Coupled mode theory

We assume a waveguide with input-output field amplitude S_i and S_r coupled to a single input waveguide and to radiation with lifetimes $\tau_{||}$ and $\tau_{\perp}$. In this context, frequency conservation in a linear system dictates that the field oscillates at a fixed frequency ω, expressed as $A = e^{-i\omega t}$, leading to $dA/dt = -i\omega A$

$$-i\omega A = -i\omega_0 - \frac{A}{\tau_{\perp}} - \frac{A}{\tau_{||}} - \sqrt{\frac{2}{\tau_{||}}}S_i \tag{B.2}$$

$$S_r = -S_i + \sqrt{\frac{2}{\tau_{||}}}S_i \tag{B.3}$$

Solve A from equation B.2 and substitute in Equation B.3 to solve the reflection spectrum as follows. [111]

$$R = \frac{|S_r|^2}{|S_i|^2} = \frac{(\omega - \omega_0)^2 + (\omega_0/Q_{||} - \omega_0/2Q)^2}{((\omega - \omega_0)^2 + (\omega_0/2Q)^2} \tag{B.4}$$

At resonance condition ($\omega = \omega_0$), the maximum reflection can be calculated as below from Equation B.4.

$$R(\omega_0) = \left(\frac{Q}{Q_{\perp}}\right)^2 \tag{B.5}$$

where,

$$\frac{1}{Q} = \frac{1}{Q_{\perp}} + \frac{1}{Q_{||}} \tag{B.6}$$

Initially, we compute $Q_{\perp}$, the quality factor associated with the out-of-plane decay rate for NR = 8 and assumed that the number of output-coupling mirrors has no significant impact on $Q_{\perp}$, due to its dependence on scattering and material losses. Subsequently, we determined $Q_{||}$,

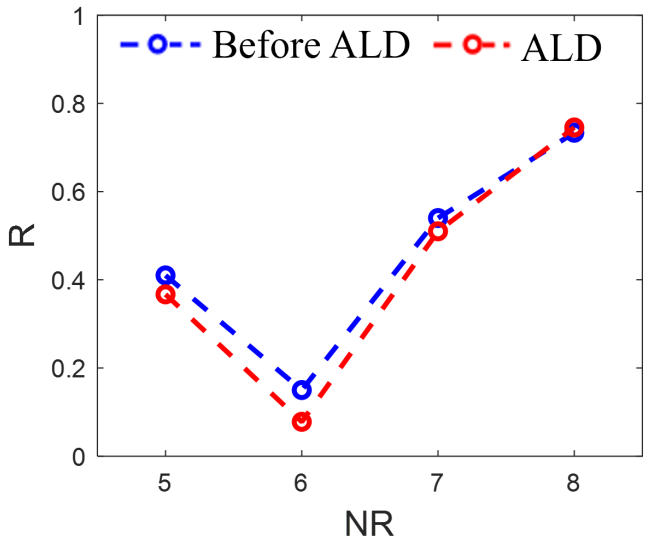


Figure B.6: The reflection coefficient of cavity at resonance as a function of the number of out-coupler holes (NR), ranging from 5 to 8, both before and after atomic layer deposition.

representing the quality factor due to the decay rate in the nanobeam, for different NR values, and measured the total quality factor Q using Equation B.6.

Appendix C:

C.1 GaAs and spacer thickness selection

Figure C.1a demonstrates the relationship between GaAs slab thickness and the relative confinement of GaAs slab and Si waveguide. The Si waveguide maintains a consistent thickness of 220 nm and a width of 580 nm throughout this analysis. This depiction emphasizes the significance of adjusting the silicon waveguide's dimensions (thickness, width) to ensure balanced confinement when incorporating GaAs of varying thicknesses.

Spacer plays a vital role in hybrid cavity design to reduce lattice mismatch between two

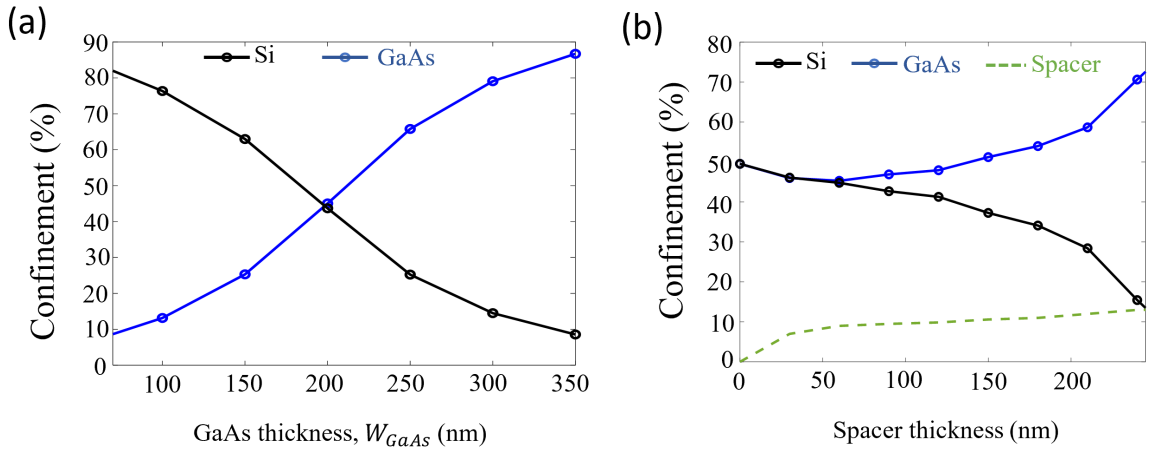


Figure C.1: (a) illustrating the relative confinement between the GaAs slab and Si waveguide for different GaAs slab thicknesses, and (b) Spacer thickness vs. confinement in GaAs slab with thickness 200 nm. Here, in both cases, the Si waveguide has a thickness of 220 nm and a width of 580 nm.

materials and efficient light coupling in Si waveguide and GaAs slab. The spacer thickness can vary widely depending on the application but cannot be arbitrarily thick. Since GaAs is a slab significantly wider than Si waveguide, the hybrid mode tends to shift to GaAs slab, as seen in Figure C.1b. So, the ideal spacer thickness can be 120 nm or less for good confinement in a Si waveguide. We choose 60 nm of spacer thickness to optimize the excellent quality factor of the hybrid cavity, but one can use any thickness as long as there is not much mode shifting in GaAs.

C.2 Purcell factor

We estimate the theoretical maximum Purcell factor of the hybrid cavity using the following equation [170].

$$F_{max} = \frac{3Q}{4\pi^2 V_m} \left(\lambda_0 / n_{eff}\right)^3 \tag{C.1}$$

Here, Q is the hybrid cavity quality factor, $Q = \lambda_0 / \Delta\lambda$, and V_m is the mode volume. Additionally, n_{eff} is the effective refractive index of the hybrid cavity, and λ_0 is the cavity resonance wavelength. We obtain F_{max} =794.17 using the FDTD calculated quality factor of $Q = 1.53 \times 10^4$, $\lambda_0 = 1516.53$ nm, and $n_{eff} = 2.60$.

C.3 Lasing Pump-Probe Simulation

The "Four-Level Two-Electron" material model is available in the FDTD (ANSYS Lumerical) Material Database, which describes the optical gain in certain materials, such as InAs quantum dots. [171] This model represents the material as a four-level atomic system with two coupled dipole oscillators, P_b (between levels 0 and 3) and P_a (between levels 1 and 2), with dephasing rates γ_b and γ_a, and angular frequencies ω_b and ω_a, respectively. To model InAs quantum dots,

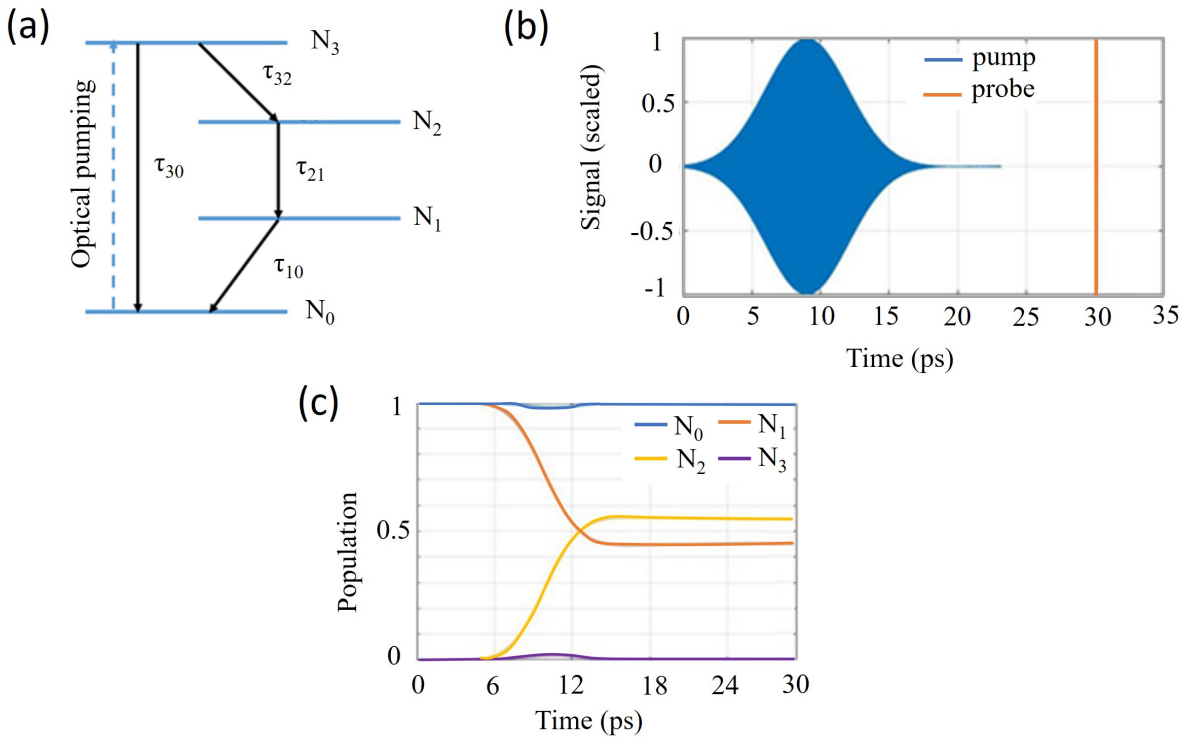


Figure C.2: (a) Four-level system with decay time constants between levels 3 to 2 and 1 to 0 of $\tau_{32} = \tau_{10} = 100$ fs, and 2 to 1 and 3 to 0 of $\tau_{21} = \tau_{30} = 300$ ps. (b) The pump and probe time signal (normalized). (c) Electron population density probability vs. time (ps) and inversion between levels 1 and 2.

we set the decay time constants as $\tau_{32} = \tau_{10} = 100$ fs and $\tau_{21} = \tau_{30} = 300$ ps, the dephasing rates as $\gamma_a = \gamma_b = 10^{13}$ Hz, and angular frequencies of $\omega_b = 2.51 \times 10^{15}$ Hz and $\omega_a = 1.24 \times 10^{15}$ Hz [137]. In addition, we set an initial population volume density of $N_1 = N_0 = 8 \times 10^{21}/m^3$, which corresponds to a planar density of $4 \times 10^{10}/cm^2$ for four layers of quantum dots at 50 nm intervals in the GaAs slab. [142]

In order to simulate lasing in FDTD, we incorporate a Gaussian pump with a pulse width of 4.5 ps, which excites the InAs/GaAs gain material for population inversion at a wavelength of 750 nm. Additionally, a broadband probe with a relatively weaker power is used to detect lasing at the hybrid cavity resonance wavelength of 1516.53 nm with a 30 ps time delay after the pump turns off. The pump pulse corresponds to the energy difference between level 3 and

level 0 ($E_3 - E_0$), as shown in Figure C.2a, [171] while the probe pulse corresponds to the energy difference between levels 2 and 1 ($E_2 - E_1$). Figure C.2b shows the hybrid cavity is pumped with a 4.5 ps pulse, centered at 9 ps, and probed with an ultra-short pulse of 30 ps. Figure C.2c plots the electron population density probability of the different levels based on the Four-Level Two-Electron model. The population in the ground state and level 3 does not change significantly. However, the population in level 2 increases while the population in level 1 decreases, with a population inversion in the metastable states (between levels 2 and 1) after 12 ps, as shown by the orange and yellow curves in Figure C.2c. [171]

Finally, in our simulation we place a frequency-domain monitor at one end of the hybrid cavity to calculate the electric field amplitude as the output field intensity and converted it into power. Therefore, by sweeping the input pump power from the other end of the hybrid cavity, we can calculate the output power and obtain a light-in vs. light-out (L-L) curve, as shown by the black data points in Figure 4.3.

C.4 Lasing rate equation

We use a standard coupled rate-equation model by G. Bjor and Y. Yamamoto [143] for a semiconductor laser with a carrier density N, cavity photon number p, spontaneous emission coupling ratio β, and laser power threshold P_{th}. The coupled rate equations are given below,

$$\frac{d}{dt}n = \frac{\eta_{in} P_{in}}{\hbar \omega V} - \frac{N}{\tau_{sp}} - \frac{N}{\tau_{nr}} - \frac{gp}{V} \tag{C.2}$$

$$\frac{d}{dt}p = -\left(\gamma - g\right)p + \frac{\beta V}{\tau_{sp}}N \tag{C.3}$$

Where P_{in} is the input power of the pump laser, η_{in} is the pumping efficiency (i.e., the fraction of the optical pump power absorbed by the gain material), V is the gain medium's volume, and τ_{sp} and τ_{nr} are the radiative and nonradiative lifetimes of the excitons, respectively.

Additionally, $g = g'(N - N_0)$ is the material gain, which is linearly proportional to the carrier density, $g' = \frac{\beta V}{\tau_{sp}}$ is a material constant, cavity photon number, $p = \frac{P_{out}}{\hbar\omega\gamma\eta_{out}}$ where P_{out} is the output power, and N_0 is the transparency carrier density of the material. The steady-state solution of Equations C.2 and C.3 is

$$P_{in} = \frac{\hbar\omega\gamma}{\beta\eta_{in}}\left[\frac{p}{1+p}(1+\zeta)(1+\beta p) - \zeta\beta p\right] \tag{C.4}$$

Here, $\zeta = N_0\beta V/\gamma\tau_{sp}$ is the cavity photon number at transparency. From Equation C.4, we can calculate the average cavity photon number and light-in vs. light-out (L-L) curves for different spontaneous emission coupling ratios (β) using a transparency carrier density of around $N = N_0 = 8 \times 10^{21}/m3$, [] as shown by the solid curves in Figure C.3 and Figure 4.3, consecutively.

C.5 Bistability theory

We compare our FDTD simulation results to the theoretical optical bistability using a semiclassical analysis based on Maxwell-Bloch equations introduced by Bonifacio and Lugiato. [157] The steady-state solution for a homogeneously broadened two-level system is given below [157, 158]

$$y = x + \frac{2Cx}{1+x^2} \tag{C.5}$$

Where x and y are the output field amplitude and input field amplitude, respectively, and

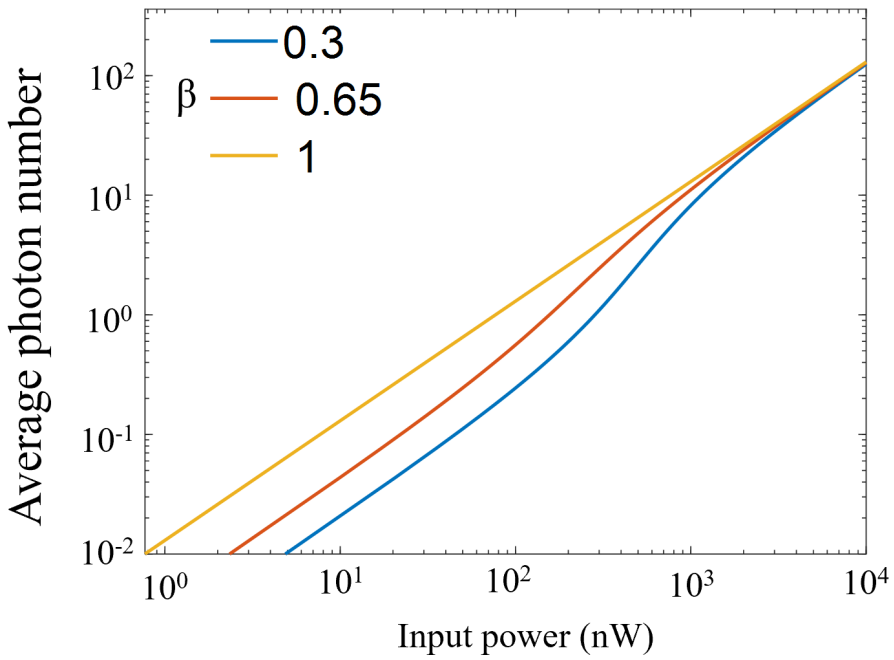


Figure C.3: Average number of photons in the cavity vs. input power for different spontaneous emission coupling ratios β = 0.3, 0.65, and 1.

the co-operativity parameter C, which is used to characterize the nonlinear behavior of the cavity, is defined as $C = \alpha L/2T$, where α is the absorption coefficient of the quantum dots in the GaAs region of the cavity, L is the length of the cavity, and T is the transmission of the hybrid cavity. We calculate the co-operativity parameter $C = 10.49$ for our hybrid cavity from the FDTD calculated absorption coefficient $\alpha = 1.47 \times 10^4 cm^{-1}$, $T = 0.86$, and $L = 12.27\mu$m.

C.6 Wavelength tuning of the hybrid Si-GaAs cavity

The first step is to tune the wavelengths of the hybrid cavity to select confinement in the silicon and GaAs region. To change the wavelength, we can have the same structure with the same width and thickness as the silicon waveguide and GaAs slab used for 1516.63 nm. The second step is to change the period and radius of the ellipsoidal holes. For example, at 1304.1 nm

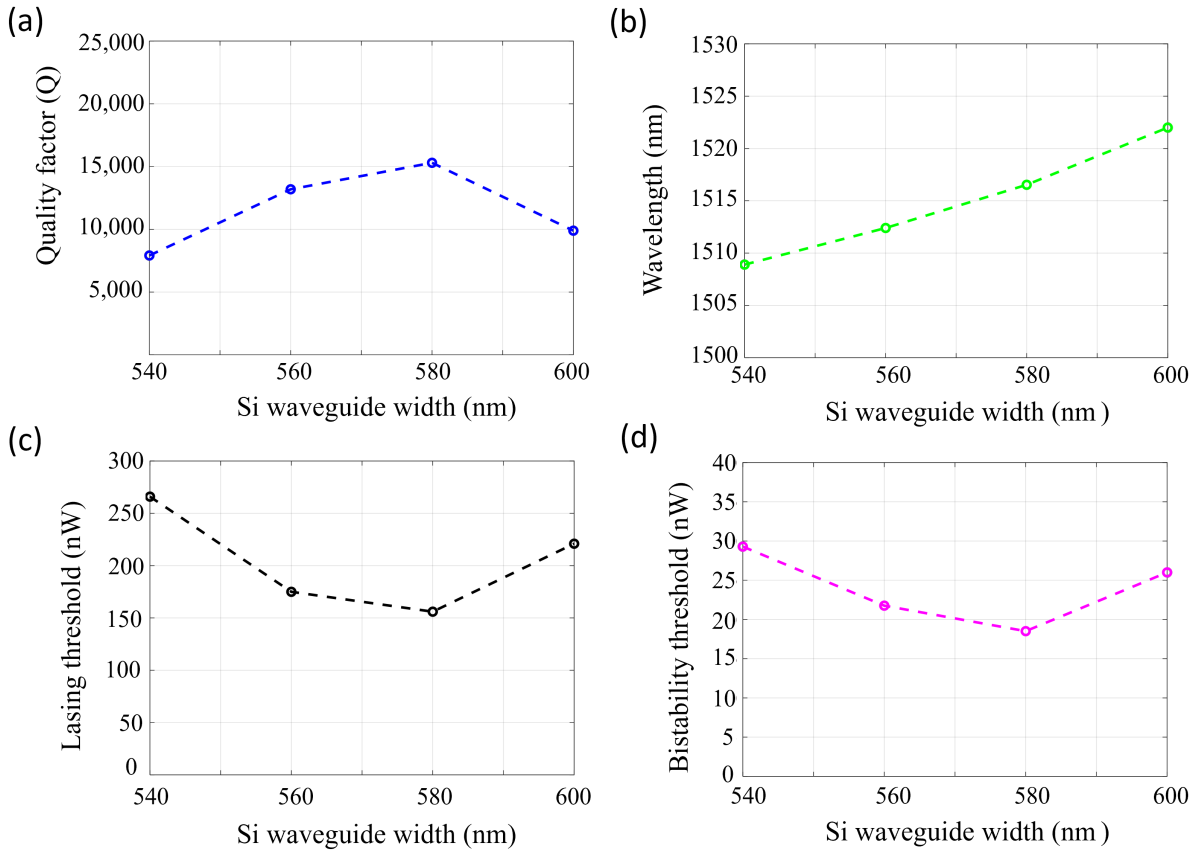


Figure C.4: (a) The quality factor, (b) Wavelength, (c) Lasing threshold power, and (b) Bistability threshold power for silicon waveguide widths of 540 nm, 560 nm, 580 nm, and 600 nm.

wavelength where the InAs/GaAs QDs typically emit the cavity design parameters are (ellipse major axis radius 135 nm and 90 nm, and period is 275 nm, five centered pairs of ellipses linearly increase from 135 nm to 145 nm and 90 nm to 97 nm, respectively) provides a quality factor of 1.97×10^4. The hybrid cavity can be wavelength-tuned as an alternative approach by uniformly scaling all relevant parameters, such as width, thickness, hole radius, and period.

C.7 Lasing and bistability performance for different device dimensions

The width of the silicon waveguide is a key factor in the hybrid cavity device because it controls the confinement within the silicon waveguide and the GaAs slab, as indicated in

Figure 1d. We've calculated the hybrid cavity's quality factors and corresponding wavelengths for various silicon waveguide widths: 540 nm, 560 nm, 580 nm, and 600 nm, as presented in Figure C.4a and C.4b, consecutively. We have also examined the threshold power required for these waveguide widths to understand the performance trends for lasing and bistability. Figures C.4c and C.4d depict the thresholds for lasing and bistability across different Si waveguide widths (W_{Si}). The performance trends highlight that the quality factor of the hybrid cavity plays the most critical role in influencing lasing and bistability performance. By adjusting the period and radius of the elliptical holes, further optimization of the hybrid cavity quality factor can lead to improved lasing and bistability implementations.

Appendix D: List of Publications and Conference Talks

J1. **Rahaman, Mohammad Habibur**, Samuel Harper, Chang-Min Lee, Kyu-Young Kim, Mustafa Atabey Buyukkaya, Victor J. Patel, Samuel D. Hawkins, Je-Hyung Kim, Sadhvikas Addamane, and Edo Waks. "Efficient, indistinguishable telecom C-band photons using a tapered nanobeam." arXiv preprint arXiv:2404.01562 (2024).

J2. Islam, Fariba, Chang-Min Lee, Samuel Harper, **Mohammad Habibur Rahaman**, Yuqi Zhao, Neelesh Kumar Vij, and Edo Waks. "Cavity-Enhanced Emission from a Silicon T Center." Nano Letters 24, no. 1 (2023): 319-325.

J3. **Rahaman, Mohammad Habibur**, Chang-Min Lee, Mustafa Atabey Buyukkaya, Samuel Harper, Fariba Islam, and Edo Waks. "Optimizing the quality factor of InP nanobeam cavities using atomic layer deposition." arXiv preprint arXiv:2312.05967 (2023).

J4. **Rahaman, Mohammad Habibur**, Chang-Min Lee, Mustafa Atabey Buyukkaya, Yuqi Zhao, and Edo Waks. "Hybrid Si-GaAs photonic crystal cavity for lasing and bistability." Optics Express 31, no. 23 (2023): 37574-37582.

C1. **Rahaman, Mohammad Habibur**, Chang-Min Lee, Mustafa Atabey Buyukkaya, Samuel Harper, Fariba Islam, and Edo Waks. "Quality factor enhancement of InP nanobeam cavities using atomic layer deposition." In Photonic and Phononic Properties of Engineered Nanostructures XIV, vol. 12896, pp. 67-68. SPIE, 2024.

C2. Islam, Fariba, Changmin Lee, Mustafa Atabey Buyukkaya, Stephanie Simmons, Daniel Higginbottom, Samuel Harper, **Mohammad Habibur Rahaman**, and Edo Waks. "High-efficiency single photon emission from a silicon T-center in a nanobeam." Bulletin of the American Physical Society (2024).

C3. **Rahaman, Habibur**, Chang-Min Lee, Mustafa Atabey Buyukkaya, Yuqi Zhao, and Edo Waks. "Low threshold lasing based on a hybrid Si/III-V cavity with quantum dots." In CLEO: Applications and Technology, pp. ATu3R-5. Optica Publishing Group, 2023.

C4. **Rahaman, Mohammad Habibur**, Mustafa Atabey Buyukkaya, Changmin Lee, Yuqi Zhao, and Edo Waks. "Low threshold optical bistability in a hybrid Si-GaAs cavity with quantum dots." In APS March Meeting Abstracts, vol. 2023, pp. Z65-005. 2023.

C5. **Rahaman, Mohammad Habibur**, Mustafa Atabey Buyukkaya, Yuqi Zhao, Chang-Min Lee, and Edo Waks. "GaAs/Si hybrid mode photonic crystal nanobeam cavity for saturable nonlinearity." In APS March Meeting Abstracts, vol. 2022, pp. T00-309. 2022.

Bibliography

[1] Rikizo Ikuta, Hiroshi Kato, Yoshiaki Kusaka, Shigehito Miki, Taro Yamashita, Hirotaka Terai, Mikio Fujiwara, Takashi Yamamoto, Masato Koashi, Masahide Sasaki, et al. High-fidelity conversion of photonic quantum information to telecommunication wavelength with superconducting single-photon detectors. *Physical Review A*, 87(1):010301, 2013.

[2] Sebastien Tanzilli, Wolfgang Tittel, Matthaeus Halder, Olivier Alibart, Pascal Baldi, Nicolas Gisin, and Hugo Zbinden. A photonic quantum information interface. *Nature*, 437(7055):116–120, 2005.

[3] Muhammad Danang Birowosuto, Hisashi Sumikura, Shinji Matsuo, Hideaki Taniyama, Peter J Van Veldhoven, Richard Nötzel, and Masaya Notomi. Fast purcell-enhanced single photon source in 1,550-nm telecom band from a resonant quantum dot-cavity coupling. *Scientific reports*, 2(1):321, 2012.

[4] Stefan W Glunz and Frank Feldmann. Sio2 surface passivation layers–a key technology for silicon solar cells. *Solar Energy Materials and Solar Cells*, 185:260–269, 2018.

[5] H Mäckel and R Lüdemann. Detailed study of the composition of hydrogenated sin x layers for high-quality silicon surface passivation. *Journal of applied physics*, 92(5):2602–2609, 2002.

[6] Francis P Zamborini and Richard M Crooks. Corrosion passivation of gold by n-alkanethiol self-assembled monolayers: effect of chain length and end group. *Langmuir*, 14(12):3279–3286, 1998.

[7] Lu Zhou, Baoxue Bo, Xingzhen Yan, Chao Wang, Yaodan Chi, and Xiaotian Yang. Brief review of surface passivation on iii-v semiconductor. *Crystals*, 8(5):226, 2018.

[8] Nahum Izhaky, Michael T Morse, Sean Koehl, Oded Cohen, Doron Rubin, Assia Barkai, Gadi Sarid, Rami Cohen, and Mario J Paniccia. Development of cmos-compatible integrated silicon photonics devices. *IEEE Journal of Selected Topics in Quantum Electronics*, 12(6):1688–1698, 2006.

[9] Zhechao Wang, Amin Abbasi, Utsav Dave, Andreas De Groote, Sulakshna Kumari, Bernadette Kunert, Clement Merckling, Marianna Pantouvaki, Yuting Shi, Bin Tian, et al. Novel light source integration approaches for silicon photonics. *Laser & Photonics Reviews*, 11(4):1700063, 2017.

[10] Yaocheng Shi, Yong Zhang, Yating Wan, Yu Yu, Yuguang Zhang, Xiao Hu, Xi Xiao, Hongnan Xu, Long Zhang, and Bingcheng Pan. Silicon photonics for high-capacity data communications. *Photonics Research*, 10(9):A106–A134, 2022.

[11] Pengfei Xu and Zhiping Zhou. Silicon-based optoelectronics for general-purpose matrix computation: a review. *Advanced Photonics*, 4(4):044001–044001, 2022.

[12] Yu Chen, Hongtao Lin, Juejun Hu, and Mo Li. Heterogeneously integrated silicon photonics for the mid-infrared and spectroscopic sensing. *ACS nano*, 8(7):6955–6961, 2014.

[13] Markus Deubel, Georg Von Freymann, Martin Wegener, Suresh Pereira, Kurt Busch, and Costas M Soukoulis. Direct laser writing of three-dimensional photonic-crystal templates for telecommunications. *Nature materials*, 3(7):444–447, 2004.

[14] Christoph Fenzl, Thomas Hirsch, and Otto S Wolfbeis. Photonic crystals for chemical sensing and biosensing. *Angewandte Chemie International Edition*, 53(13):3318–3335, 2014.

[15] Withawat Withayachumnankul, Masayuki Fujita, and Tadao Nagatsuma. Integrated silicon photonic crystals toward terahertz communications. *Advanced Optical Materials*, 6(16):1800401, 2018.

[16] Marko Lončar, Theodor Doll, Jelena Vučković, and Axel Scherer. Design and fabrication of silicon photonic crystal optical waveguides. *Journal of lightwave technology*, 18(10):1402, 2000.

[17] Lina Maigyte and Kestutis Staliunas. Spatial filtering with photonic crystals. *Applied physics reviews*, 2(1), 2015.

[18] Takasumi Tanabe, Masaya Notomi, Satoshi Mitsugi, Akihiko Shinya, and Eiichi Kuramochi. All-optical switches on a silicon chip realized using photonic crystal nanocavities. *Applied Physics Letters*, 87(15), 2005.

[19] Hatice Altug, Dirk Englund, and Jelena Vučković. Ultrafast photonic crystal nanocavity laser. *Nature physics*, 2(7):484–488, 2006.

[20] Pavel G Serafimovich and Nikolay L Kazanskiy. Optical modulator based on coupled photonic crystal cavities. *Journal of Modern Optics*, 63(13):1233–1238, 2016.

[21] Julian Münzberg, Andreas Vetter, Fabian Beutel, Wladick Hartmann, Simone Ferrari, Wolfram HP Pernice, and Carsten Rockstuhl. Superconducting nanowire single-photon detector implemented in a 2d photonic crystal cavity. *Optica*, 5(5):658–665, 2018.

[22] Qihuang Gong and Xiaoyong Hu. *Photonic crystals: principles and applications*. CRC press, 2014.

[23] Dirk Englund, Ilya Fushman, and Jelena Vuckovic. General recipe for designing photonic crystal cavities. *Optics express*, 13(16):5961–5975, 2005.

[24] Ali W Elshaari, Wolfram Pernice, Kartik Srinivasan, Oliver Benson, and Val Zwiller. Hybrid integrated quantum photonic circuits. *Nature photonics*, 14(5):285–298, 2020.

[25] AJ Trindade, B Guilhabert, EY Xie, R Ferreira, JJD McKendry, D Zhu, N Laurand, E Gu, DJ Wallis, IM Watson, et al. Heterogeneous integration of gallium nitride light-emitting diodes on diamond and silica by transfer printing. *Optics express*, 23(7):9329–9338, 2015.

[26] Sulakshna Kumari, Emanuel P Haglund, Johan S Gustavsson, Anders Larsson, Gunther Roelkens, and Roel G Baets. Vertical-cavity silicon-integrated laser with in-plane waveguide emission at 850 nm. *Laser & Photonics Reviews*, 12(2):1700206, 2018.

[27] Stijn Cuyvers, Artur Hermans, Max Kiewiet, Jeroen Goyvaerts, Gunther Roelkens, Kasper Van Gasse, Dries Van Thourhout, and Bart Kuyken. Heterogeneous integration of si photodiodes on silicon nitride for near-visible light detection. *Optics Letters*, 47(4):937–940, 2022.

[28] Yueyang Chen, Albert Ryou, Max R Friedfeld, Taylor Fryett, James Whitehead, Brandi M Cossairt, and Arka Majumdar. Deterministic positioning of colloidal quantum dots on silicon nitride nanobeam cavities. *Nano letters*, 18(10):6404–6410, 2018.

[29] Jae-Seong Park, Mingchu Tang, Siming Chen, and Huiyun Liu. Heteroepitaxial growth of iii-v semiconductors on silicon. *Crystals*, 10(12):1163, 2020.

[30] Shuyu Bao, Yue Wang, Khaw Lina, Li Zhang, Bing Wang, Wardhana Aji Sasangka, Kenneth Eng Kian Lee, Soo Jin Chua, Jurgen Michel, Eugene Fitzgerald, et al. A review of silicon-based wafer bonding processes, an approach to realize the monolithic integration of si-cmos and iii–v-on-si wafers. *Journal of Semiconductors*, 42(2):023106, 2021.

[31] Jing Zhang, Grigorij Muliuk, Joan Juvert, Sulakshna Kumari, Jeroen Goyvaerts, Bahawal Haq, Camiel Op de Beeck, Bart Kuyken, Geert Morthier, Dries Van Thourhout, et al. Iii-v-on-si photonic integrated circuits realized using micro-transfer-printing. *APL photonics*, 4(11), 2019.

[32] Sören Wengerowsky, Siddarth Koduru Joshi, Fabian Steinlechner, Hannes Hübel, and Rupert Ursin. An entanglement-based wavelength-multiplexed quantum communication network. *Nature*, 564(7735):225–228, 2018.

[33] Sebastian Zaske, Andreas Lenhard, and Christoph Becher. Efficient frequency downconversion at the single photon level from the red spectral range to the telecommunications c-band. *Optics express*, 19(13):12825–12836, 2011.

[34] Benjamin Kambs, Jan Kettler, Matthias Bock, Jonas Nils Becker, Carsten Arend, Andreas Lenhard, Simone Luca Portalupi, Michael Jetter, Peter Michler, and Christoph Becher. Low-noise quantum frequency down-conversion of indistinguishable photons. *Optics express*, 24(19):22250–22260, 2016.

[35] Xiaowei He, Nicolai F Hartmann, Xuedan Ma, Younghee Kim, Rachelle Ihly, Jeffrey L Blackburn, Weilu Gao, Junichiro Kono, Yohei Yomogida, Atsushi Hirano, et al. Tunable room-temperature single-photon emission at telecom wavelengths from sp 3 defects in carbon nanotubes. *Nature Photonics*, 11(9):577–582, 2017.

[36] Robert Sittig, Cornelius Nawrath, Sascha Kolatschek, Stephanie Bauer, Richard Schaber, Jiasheng Huang, Ponraj Vijayan, Pascal Pruy, Simone Luca Portalupi, Michael Jetter, et al. Thin-film ingaas metamorphic buffer for telecom c-band inas quantum dots and optical resonators on gaas platform. *Nanophotonics*, 11(6):1109–1116, 2022.

[37] Matthias Paul, Fabian Olbrich, Jonatan Höschele, Susanne Schreier, Jan Kettler, Simone Luca Portalupi, Michael Jetter, and Peter Michler. Single-photon emission at 1.55 μm from movpe-grown inas quantum dots on ingaas/gaas metamorphic buffers. *Applied Physics Letters*, 111(3), 2017.

[38] Cornelius Nawrath, Raphael Joos, Sascha Kolatschek, Stephanie Bauer, Pascal Pruy, Florian Hornung, Julius Fischer, Jiasheng Huang, Ponraj Vijayan, Robert Sittig, et al. Bright source of purcell-enhanced, triggered, single photons in the telecom c-band. *Advanced Quantum Technologies*, 6(11):2300111, 2023.

[39] Zhenxuan Ge, Tunghsun Chung, Yu-Ming He, Mohamed Benyoucef, and Yongheng Huo. Polarized and bright telecom c-band single-photon source from inp-based quantum dots coupled to elliptical bragg gratings. *Nano Letters*, 2024.

[40] Anna Musiał, Paweł Holewa, Paweł Wyborski, Marcin Syperek, Andrei Kors, Johann Peter Reithmaier, Grzegorz Sek, and Mohamed Benyoucef. High-purity triggered single-photon emission from symmetric single inas/inp quantum dots around the telecom c-band window. *Advanced Quantum Technologies*, 3(2):1900082, 2020.

[41] Raphael Joos, Stephanie Bauer, Christian Rupp, Sascha Kolatschek, Wolfgang Fischer, Cornelius Nawrath, Ponraj Vijayan, Robert Sittig, Michael Jetter, Simone L Portalupi, et al. Triggered telecom c-band single-photon source with high brightness, high indistinguishability and sub-ghz spectral linewidth. *arXiv preprint arXiv:2310.20647*, 2023.

[42] Paweł Holewa, Emilia Zieba-Ostój, Daniel A Vajner, Maja Wasiluk, Benedek Gaál, Aurimas Sakanas, Marek Burakowski, Paweł Mrowiński, Bartosz Krajnik, Meng Xiong, et al. Scalable quantum photonic devices emitting indistinguishable photons in the telecom c-band. *arXiv preprint arXiv:2304.02515*, 2023.

[43] Daniel A Vajner, Paweł Holewa, Emilia Zieba-Ostoj, Maja Wasiluk, Martin von Helversen, Aurimas Sakanas, Alexander Huck, Kresten Yvind, Niels Gregersen, Anna Musiał, et al.

On-demand generation of indistinguishable photons in the telecom c-band using quantum dot devices. *ACS photonics*, 2024.

[44] Toshiyuki Miyazawa, Kazuya Takemoto, Yoshiki Sakuma, Shinichi Hirose, Tatsuya Usuki, Naoki Yokoyama, Motomu Takatsu, and Yasuhiko Arakawa. Single-photon generation in the 1.55-μm optical-fiber band from an inas/inp quantum dot. *Japanese Journal of Applied Physics*, 44(5L):L620, 2005.

[45] A Musiał, M Mikulicz, P Mrowiński, A Zielińska, P Sitarek, P Wyborski, M Kuniej, JP Reithmaier, G Sek, and M Benyoucef. Inp-based single-photon sources operating at telecom c-band with increased extraction efficiency. *Applied Physics Letters*, 118(22), 2021.

[46] Paweł Holewa, Aurimas Sakanas, Ugur M Gur, Paweł Mrowinski, Alexander Huck, Bi-Ying Wang, Anna Musiał, Kresten Yvind, Niels Gregersen, Marcin Syperek, et al. Bright quantum dot single-photon emitters at telecom bands heterogeneously integrated on si. *ACS photonics*, 9(7):2273–2279, 2022.

[47] T Miyazawa, K Takemoto, Y Nambu, S Miki, T Yamashita, H Terai, M Fujiwara, M Sasaki, Y Sakuma, M Takatsu, et al. Single-photon emission at 1.5 μm from an inas/inp quantum dot with highly suppressed multi-photon emission probabilities. *Applied Physics Letters*, 109(13), 2016.

[48] L Wells, T Müller, RM Stevenson, J Skiba-Szymanska, DA Ritchie, and AJ Shields. Coherent light scattering from a telecom c-band quantum dot. *Nature Communications*, 14(1):8371, 2023.

[49] M Anderson, T Müller, J Skiba-Szymanska, AB Krysa, J Huwer, RM Stevenson, J Heffernan, DA Ritchie, and AJ Shields. Coherence in single photon emission from droplet epitaxy and stranski–krastanov quantum dots in the telecom c-band. *Applied Physics Letters*, 118(1), 2021.

[50] Andrew N Wakileh, Lingxi Yu, Doğa Dokuz, Sofiane Haffouz, Xiaohua Wu, Jean Lapointe, David B Northeast, Robin L Williams, Nir Rotenberg, Philip J Poole, et al. Single photon emission in the telecom c-band from nanowire-based quantum dots. *Applied Physics Letters*, 124(4), 2024.

[51] Andrei Kors, Johann Peter Reithmaier, and Mohamed Benyoucef. Telecom wavelength single quantum dots with very small excitonic fine-structure splitting. *Applied Physics Letters*, 112(17), 2018.

[52] M Yacob, JP Reithmaier, and M Benyoucef. Low-density inp-based quantum dots emitting around the 1.5 μm telecom wavelength range. *Applied Physics Letters*, 104(2), 2014.

[53] Richard P Leavitt and Christopher JK Richardson. Pathway to achieving circular inas quantum dots directly on (100) inp and to tuning their emission wavelengths toward 1.55 μm. *Journal of Vacuum Science & Technology B*, 33(5), 2015.

[54] Chang-Min Lee, Mustafa Atabey Buyukkaya, Samuel Harper, Shahriar Aghaeimeibodi, Christopher JK Richardson, and Edo Waks. Bright telecom-wavelength single photons based on a tapered nanobeam. *Nano letters*, 21(1):323–329, 2020.

[55] Fariba Islam, Chang-Min Lee, Samuel Harper, Mohammad Habibur Rahaman, Yuqi Zhao, Neelesh Kumar Vij, and Edo Waks. Cavity-enhanced emission from a silicon t center. *Nano Letters*, 24(1):319–325, 2023.

[56] Gabriele Bulgarini, Michael E Reimer, Maaike Bouwes Bavinck, Klaus D Jons, Dan Dalacu, Philip J Poole, Erik PAM Bakkers, and Val Zwiller. Nanowire waveguides launching single photons in a gaussian mode for ideal fiber coupling. *Nano letters*, 14(7):4102–4106, 2014.

[57] Shahriar Aghaeimeibodi, Chang-Min Lee, Mustafa Atabey Buyukkaya, Christopher JK Richardson, and Edo Waks. Large stark tuning of inas/inp quantum dots. *Applied Physics Letters*, 114(7), 2019.

[58] Mohammad Habibur Rahaman, Chang-Min Lee, Mustafa Atabey Buyukkaya, Samuel Harper, Fariba Islam, and Edo Waks. Optimizing the quality factor of inp nanobeam cavities using atomic layer deposition. *arXiv preprint arXiv:2312.05967*, 2023.

[59] Chang-Min Lee, Fariba Islam, Samuel Harper, Mustafa Atabey Buyukkaya, Daniel Higginbottom, Stephanie Simmons, and Edo Waks. High-efficiency single photon emission from a silicon t-center in a nanobeam. *ACS Photonics*, 10(11):3844–3849, 2023.

[60] I Aharonovich, Stefania Castelletto, DA Simpson, AD Greentree, and Steven Prawer. Photophysics of chromium-related diamond single-photon emitters. *Physical Review A*, 81(4):043813, 2010.

[61] Matthew Pelton, Charles Santori, Jelena Vucković, Bingyang Zhang, Glenn S Solomon, Jocelyn Plant, and Yoshihisa Yamamoto. Efficient source of single photons: a single quantum dot in a micropost microcavity. *Physical review letters*, 89(23):233602, 2002.

[62] Sebastian Unsleber, Yu-Ming He, Stefan Gerhardt, Sebastian Maier, Chao-Yang Lu, Jian-Wei Pan, Niels Gregersen, Martin Kamp, Christian Schneider, and Sven Höfling. Highly indistinguishable on-demand resonance fluorescence photons from a deterministic quantum dot micropillar device with 74% extraction efficiency. *Optics express*, 24(8):8539–8546, 2016.

[63] RB Patel, AJ Bennett, K Cooper, P Atkinson, CA Nicoll, DA Ritchie, and AJ Shields. Postselective two-photon interference from a continuous nonclassical stream of photons emitted by a quantum dot. *Physical Review Letters*, 100(20):207405, 2008.

[64] Raphaël Proux, Maria Maragkou, Emmanuel Baudin, Christophe Voisin, Philippe Roussignol, and Carole Diederichs. Measuring the photon coalescence time window in the continuous-wave regime for resonantly driven semiconductor quantum dots. *Physical Review Letters*, 114(6):067401, 2015.

[65] M Anderson, T Müller, J Huwer, J Skiba-Szymanska, AB Krysa, RM Stevenson, J Heffernan, DA Ritchie, and AJ Shields. Quantum teleportation using highly coherent emission from telecom c-band quantum dots. *npj Quantum Information*, 6(1):14, 2020.

[66] Christopher L Morrison, Markus Rambach, Zhe Xian Koong, Francesco Graffitti, Fiona Thorburn, Ajoy K Kar, Yong Ma, Suk-In Park, Jin Dong Song, Nick G Stoltz, et al. A bright source of telecom single photons based on quantum frequency conversion. *Applied Physics Letters*, 118(17), 2021.

[67] H Ollivier, SE Thomas, SC Wein, I Maillette de Buy Wenniger, N Coste, JC Loredo, N Somaschi, A Harouri, A Lemaitre, I Sagnes, et al. Hong-ou-mandel interference with imperfect single photon sources. *Physical Review Letters*, 126(6):063602, 2021.

[68] Eva Scholl, Lukas Hanschke, Lucas Schweickert, Katharina D Zeuner, Marcus Reindl, Saimon Filipe Covre da Silva, Thomas Lettner, Rinaldo Trotta, Jonathan J Finley, Kai Muller, et al. Resonance fluorescence of gaas quantum dots with near-unity photon indistinguishability. *Nano Letters*, 19(4):2404–2410, 2019.

[69] Gabija Kiršanskė, Henri Thyrrestrup, Raphaël S Daveau, Chris L Dreeßen, Tommaso Pregnolato, Leonardo Midolo, Petru Tighineanu, Alisa Javadi, Søren Stobbe, Rüdiger Schott, et al. Indistinguishable and efficient single photons from a quantum dot in a planar nanobeam waveguide. *Physical Review B*, 96(16):165306, 2017.

[70] Minho Choi, Seongmoon Jun, Kie Young Woo, Hyun Gyu Song, Hwan-Seop Yeo, Sunghan Choi, Doyoun Park, Chung-Hyun Park, and Yong-Hoon Cho. Nanoscale focus pinspot for high-purity quantum emitters via focused-ion-beam-induced luminescence quenching. *ACS nano*, 15(7):11317–11325, 2021.

[71] Hugo Larocque, Mustafa Atabey Buyukkaya, Carlos Errando-Herranz, Samuel Harper, Jacques Carolan, Chang-Min Lee, Christopher JK Richardson, Gerald L Leake, Daniel J Coleman, Michael L Fanto, et al. Tunable quantum emitters on large-scale foundry silicon photonics. *arXiv preprint arXiv:2306.06460*, 2023.

[72] Je-Hyung Kim, Shahriar Aghaeimeibodi, Christopher JK Richardson, Richard P Leavitt, Dirk Englund, and Edo Waks. Hybrid integration of solid-state quantum emitters on a silicon photonic chip. *Nano letters*, 17(12):7394–7400, 2017.

[73] Shahriar Aghaeimeibodi, Boris Desiatov, Je-Hyung Kim, Chang-Min Lee, Mustafa Atabey Buyukkaya, Aziz Karasahin, Christopher JK Richardson, Richard P Leavitt, Marko Lončar, and Edo Waks. Integration of quantum dots with lithium niobate photonics. *Applied Physics Letters*, 113(22), 2018.

[74] Serkan Ates, Imad Agha, Angelo Gulinatti, Ivan Rech, Matthew T Rakher, Antonio Badolato, and Kartik Srinivasan. Two-photon interference using background-free quantum frequency conversion of single photons emitted by an inas quantum dot. *Physical review letters*, 109(14):147405, 2012.

[75] Yiyang Gong, Bryan Ellis, Gary Shambat, Tomas Sarmiento, James S Harris, and Jelena Vučković. Nanobeam photonic crystal cavity quantum dot laser. *Optics express*, 18(9):8781–8789, 2010.

[76] Qimin Quan, Parag B Deotare, and Marko Loncar. Photonic crystal nanobeam cavity strongly coupled to the feeding waveguide. *Applied Physics Letters*, 96(20), 2010.

[77] Mustafa Atabey Buyukkaya, Chang-Min Lee, Ahmad Mansoori, Ganesh Balakrishnan, and Edo Waks. Low power optical bistability from quantum dots in a nanobeam photonic crystal cavity. *Applied Physics Letters*, 121(8), 2022.

[78] Mohammad Habibur Rahaman, Chang-Min Lee, Mustafa Atabey Buyukkaya, Yuqi Zhao, and Edo Waks. Hybrid si-gaas photonic crystal cavity for lasing and bistability. *Optics Express*, 31(23):37574–37582, 2023.

[79] Qifeng Qiao, Ji Xia, Chengkuo Lee, and Guangya Zhou. Applications of photonic crystal nanobeam cavities for sensing. *Micromachines*, 9(11):541, 2018.

[80] Yu Chen, William S Fegadolli, William M Jones, Axel Scherer, and Mo Li. Ultrasensitive gas-phase chemical sensing based on functionalized photonic crystal nanobeam cavities. *ACS nano*, 8(1):522–527, 2014.

[81] Frank Jahnke. *Quantum optics with semiconductor nanostructures*. Elsevier, 2012.

[82] Stefan T Jagsch, Noelia Vico Triviño, Frederik Lohof, Gordon Callsen, Stefan Kalinowski, Ian M Rousseau, Roy Barzel, Jean-François Carlin, Frank Jahnke, Raphaël Butté, et al. A quantum optical study of thresholdless lasing features in high-β nitride nanobeam cavities. *Nature communications*, 9(1):564, 2018.

[83] Jan Olthaus, Philip PJ Schrinner, Doris E Reiter, and Carsten Schuck. Optimal photonic crystal cavities for coupling nanoemitters to photonic integrated circuits. *Advanced Quantum Technologies*, 3(2):1900084, 2020.

[84] Daquan Yang, Xiao Liu, Xiaogang Li, Bing Duan, Aiqiang Wang, and Yunfeng Xiao. Photoic crystal nanobeam cavity devices for on-chip integrated silicon photonics. *Journal of Semiconductors*, 42(2):023103, 2021.

[85] Yacine Halioua, A Bazin, P Monnier, TJ Karle, Günther Roelkens, I Sagnes, R Raj, and F Raineri. Hybrid iii-v semiconductor/silicon nanolaser. *Optics express*, 19(10):9221–9231, 2011.

[86] Ryota Katsumi, Yasutomo Ota, Takeyoshi Tajiri, Satoshi Iwamoto, Kaur Ranbir, Johann Peter Reithmaier, Mohamed Benyoucef, and Yasuhiko Arakawa. Cmos-compatible integration of telecom band inas/inp quantum-dot single-photon sources on a si chip using transfer printing. *Applied Physics Express*, 16(1):012004, 2022.

[87] Hoon-Ki Lee, Hyung-Joong Yun, Kyu-Hwan Shim, Hyun-Gwon Park, Tae-Hoon Jang, Sung-Nam Lee, and Chel-Jong Choi. Improvement of dry etch-induced surface roughness of single crystalline β-ga2o3 using post-wet chemical treatments. *Applied Surface Science*, 506:144673, 2020.

[88] UK Chakrabarti, SJ Pearton, and F Ren. Sidewall roughness during dry etching of inp. *Semiconductor science and technology*, 6(5):408, 1991.

[89] Kazuhiro Kuruma, Yasutomo Ota, Masahiro Kakuda, Satoshi Iwamoto, and Yasuhiko Arakawa. Surface-passivated high-q gaas photonic crystal nanocavity with quantum dots. *APL Photonics*, 5(4), 2020.

[90] Shanshan Tian, Zhipeng Wei, Yongfeng Li, Haifeng Zhao, Xuan Fang, Jilong Tang, Dan Fang, Lijuan Sun, Guojun Liu, Bin Yao, et al. Surface state and optical property of sulfur passivated inp. *Materials science in semiconductor processing*, 17:33–37, 2014.

[91] Riikka L Puurunen. Surface chemistry of atomic layer deposition: A case study for the trimethylaluminum/water process. *Journal of applied physics*, 97(12), 2005.

[92] Matthieu Weber, Anne Julbe, Andre Ayral, Philippe Miele, and Mikhael Bechelany. Atomic layer deposition for membranes: basics, challenges, and opportunities. *Chemistry of Materials*, 30(21):7368–7390, 2018.

[93] Fang Zou, Yunqi Liu, Chuanlu Deng, Yanhua Dong, Shan Zhu, and Tingyun Wang. Refractive index sensitivity of nano-film coated long-period fiber gratings. *Optics express*, 23(2):1114–1124, 2015.

[94] Anguel Nikolov Wang, Jian Jim and Qihong Wu. Nano-and microlens arrays grown using atomic-layer deposition. *IEEE Photonics technology letters*, 18(24):2650–2651, 2006.

[95] Stefan Schartner, Stefan Kalchmair, Aaron Maxwell Andrews, Pavel Klang, Werner Schrenk, and Gottfried Strasser. Post-fabrication fine-tuning of photonic crystal quantum well infrared photodetectors. *Applied Physics Letters*, 94(23), 2009.

[96] Xiaodong Yang, Charlton J Chen, Chad A Husko, and Chee Wei Wong. Digital resonance tuning of high-q/ vm silicon photonic crystal nanocavities by atomic layer deposition. *Applied Physics Letters*, 91(16), 2007.

[97] Mustafa M Aslan, Nathan A Webster, Courtney L Byard, Marcelo B Pereira, Colin M Hayes, Rodrigo S Wiederkehr, and Sergio B Mendes. Low-loss optical waveguides for the near ultra-violet and visible spectral regions with al2o3 thin films from atomic layer deposition. *Thin Solid Films*, 518(17):4935–4940, 2010.

[98] Hao-Tien Cheng, Junyi Qiu, Chun-Yen Peng, Hao-Chung Kuo, Milton Feng, and Chao-Hsin Wu. 29 ghz single-mode vertical-cavity surface-emitting lasers passivated by atomic layer deposition. *Optics Express*, 30(26):47553–47566, 2022.

[99] ML Huang, YC Chang, CH Chang, YJ Lee, P Chang, J Kwo, TB Wu, and M Hong. Surface passivation of iii-v compound semiconductors using atomic-layer-deposition-grown al2o3. *Applied Physics Letters*, 87(25), 2005.

[100] Dingkun Ren, Khalifa M Azizur-Rahman, Zixuan Rong, Bor-Chau Juang, Siddharth Somasundaram, Mohammad Shahili, Alan C Farrell, Benjamin S Williams, and Diana L Huffaker. Room-temperature midwavelength infrared inassb nanowire photodetector arrays with al2o3 passivation. *Nano letters*, 19(5):2793–2802, 2019.

[101] Michael Gehl, Ricky Gibson, Joshua Hendrickson, Andrew Homyk, Antti Säynätjoki, Tapani Alasaarela, Lasse Karvonen, Ari Tervonen, Seppo Honkanen, Sander Zandbergen, et al. Effect of atomic layer deposition on the quality factor of silicon nanobeam cavities. *JOSA B*, 29(2):A55–A59, 2012.

[102] Chang-Min Lee, Mustafa Atabey Buyukkaya, Shahriar Aghaeimeibodi, Aziz Karasahin, Christopher JK Richardson, and Edo Waks. A fiber-integrated nanobeam single photon source emitting at telecom wavelengths. *Applied Physics Letters*, 114(17), 2019.

[103] Steven M George. Atomic layer deposition: an overview. *Chemical reviews*, 110(1):111–131, 2010.

[104] H Dong, B Brennan, D Zhernokletov, J Kim, CL Hinkle, and RM Wallace. In situ study of hfo2 atomic layer deposition on inp (100). *Applied Physics Letters*, 102(17), 2013.

[105] Alex J Henegar, Andrew J Cook, Phillip Dang, and Theodosia Gougousi. Native oxide transport and removal during atomic layer deposition of tio2 films on gaas (100) surfaces. *Acs Applied Materials & Interfaces*, 8(3):1667–1675, 2016.

[106] Te-Chang Chen, Tsung-Ting Wu, and Ming-Chang M Lee. An integrated operational platform for studying colloidal microsphere and microdroplet resonators. *IEEE Photonics Journal*, 9(3):1–14, 2017.

[107] Pei-Hsun Wang, Kuan-Lin Chiang, and Zong-Ren Yang. Study of microcomb threshold power with coupling scaling. *Scientific Reports*, 11(1):9935, 2021.

[108] Xiaoxiao Xue and Andrew M Weiner. Microwave photonics connected with microresonator frequency combs. *Frontiers of Optoelectronics*, 9:238–248, 2016.

[109] Ilya Fushman, Dirk Englund, and Jelena Vučković. Coupling of pbs quantum dots to photonic crystal cavities at room temperature. *Applied Physics Letters*, 87(24), 2005.

[110] Jelena Vučković and Yoshihisa Yamamoto. Photonic crystal microcavities for cavity quantum electrodynamics with a single quantum dot. *Applied Physics Letters*, 82(15):2374–2376, 2003.

[111] John D Joannopoulos, Steven G Johnson, Joshua N Winn, and Robert D Meade. Molding the flow of light. *Princet. Univ. Press. Princeton, NJ [ua]*, 2008.

[112] Jelena Vučković, Marko Lončar, Hideo Mabuchi, and Axel Scherer. Design of photonic crystal microcavities for cavity qed. *Physical Review E*, 65(1):016608, 2001.

[113] Dirk Englund, Hatice Altug, and Jelena Vučković. Low-threshold surface-passivated photonic crystal nanocavity laser. *Applied Physics Letters*, 91(7), 2007.

[114] Zhiping Zhou, Bing Yin, and Jurgen Michel. On-chip light sources for silicon photonics. *Light: Science & Applications*, 4(11):e358–e358, 2015.

[115] Minh A Tran, Duanni Huang, and John E Bowers. Tutorial on narrow linewidth tunable semiconductor lasers using si/iii-v heterogeneous integration. *APL photonics*, 4(11), 2019.

[116] Sasan Fathpour. Emerging heterogeneous integrated photonic platforms on silicon. *Nanophotonics*, 4(2):143–164, 2015.

[117] Minh A Tran, Duanni Huang, Tin Komljenovic, Jonathan Peters, Aditya Malik, and John E Bowers. Ultra-low-loss silicon waveguides for heterogeneously integrated silicon/iii-v photonics. *Applied Sciences*, 8(7):1139, 2018.

[118] Zhe Xiao, Xianshu Luo, Peng Huei Lim, Patinharekandy Prabhathan, Samson TH Silalahi, Tsung-Yang Liow, Jing Zhang, and Feng Luan. Ultra-compact low loss polarization insensitive silicon waveguide splitter. *Optics Express*, 21(14):16331–16336, 2013.

[119] Daniil S Zemtsov, Denis M Zhigunov, Sergey S Kosolobov, Anastasia K Zemtsova, Marius Puplauskis, Ivan A Pshenichnyuk, and Vladimir P Drachev. Broadband silicon grating couplers with high efficiency and a robust design. *Optics Letters*, 47(13):3339–3342, 2022.

[120] Dirk Taillaert, Peter Bienstman, and Roel Baets. Compact efficient broadband grating coupler for silicon-on-insulator waveguides. *Optics letters*, 29(23):2749–2751, 2004.

[121] Jing Zhang, Tsung-Yang Liow, Mingbin Yu, Guo-Qiang Lo, and Dim-Lee Kwong. Silicon waveguide based te mode converter. *Optics Express*, 18(24):25264–25270, 2010.

[122] AMJ Koonen, Haoshuo Chen, Henrie PA van den Boom, and Oded Raz. Silicon photonic integrated mode multiplexer and demultiplexer. *IEEE Photonics Technology Letters*, 24(21):1961–1964, 2012.

[123] Yiyang Gong, Bryan Ellis, Gary Shambat, Tomas Sarmiento, James S Harris, and Jelena Vučković. Nanobeam photonic crystal cavity quantum dot laser. *Optics express*, 18(9):8781–8789, 2010.

[124] Dieter Bimberg and Nikolai Ledentsov. Quantum dots: lasers and amplifiers. *Journal of Physics: Condensed Matter*, 15(24):R1063, 2003.

[125] Tatsurou Hiraki, Takuma Aihara, Koichi Hasebe, Koji Takeda, Takuro Fujii, Takaaki Kakitsuka, Tai Tsuchizawa, Hiroshi Fukuda, and Shinji Matsuo. Heterogeneously integrated iii–v/si mos capacitor mach–zehnder modulator. *Nature Photonics*, 11(8):482–485, 2017.

[126] Tin Komljenovic, Duanni Huang, Paolo Pintus, Minh A Tran, Michael L Davenport, and John E Bowers. Photonic integrated circuits using heterogeneous integration on silicon. *Proceedings of the IEEE*, 106(12):2246–2257, 2018.

[127] Jungmin Lee, Indra Karnadi, Jin Tae Kim, Yong-Hee Lee, and Myung-Ki Kim. Printed nanolaser on silicon. *ACS Photonics*, 4(9):2117–2123, 2017.

[128] Alexandre Bazin. *III-V Semiconductor Nanocavitieson Silicon-On-Insulator Waveguide: Laser Emission, Switching and Optical Memory*. PhD thesis, Université Paris-Diderot-Paris VII, 2013.

[129] Guillaume Crosnier, Dorian Sanchez, Sophie Bouchoule, Paul Monnier, Gregoire Beaudoin, Isabelle Sagnes, Rama Raj, and Fabrice Raineri. Hybrid indium phosphide-on-silicon nanolaser diode. *Nature Photonics*, 11(5):297–300, 2017.

[130] Alto Osada, Yasutomo Ota, Ryota Katsumi, Katsuyuki Watanabe, Satoshi Iwamoto, and Yasuhiko Arakawa. Transfer-printed quantum-dot nanolasers on a silicon photonic circuit. *Applied Physics Express*, 11(7):072002, 2018.

[131] T Mitze, M Schnarrenberger, L Zimmermann, J Bruns, F Fidorra, J Kreissl, K Janiak, S Fidorra, H Heidrich, and K Petermann. Hybrid integration of iii/v lasers on a silicon-on-insulator (soi) optical board. In *IEEE International Conference on Group IV Photonics, 2005. 2nd*, pages 210–212. IEEE, 2005.

[132] Hyundai Park, Alexander W Fang, Satoshi Kodama, and John E Bowers. Hybrid silicon evanescent laser fabricated with a silicon waveguide and iii-v offset quantum wells. *Optics Express*, 13(23):9460–9464, 2005.

[133] Alexander W Fang, Hyundai Park, Richard Jones, Oded Cohen, Mario J Paniccia, and John E Bowers. A continuous-wave hybrid algainas-silicon evanescent laser. *IEEE Photonics Technology Letters*, 18(10):1143–1145, 2006.

[134] Hyundai Park, Alexander W Fang, Oded Cohen, Richard Jones, Mario J Paniccia, and John E Bowers. A hybrid algainas–silicon evanescent amplifier. *IEEE Photonics Technology Letters*, 19(4):230–232, 2007.

[135] Liu Liu, Joris Van Campenhout, Günther Roelkens, Richard A Soref, Dries Van Thourhout, Pedro Rojo-Romeo, Philippe Regreny, Christian Seassal, Jean-Marc Fédéli, and Roel Baets. Carrier-injection-based electro-optic modulator on silicon-on-insulator with a heterogeneously integrated iii-v microdisk cavity. *Optics letters*, 33(21):2518–2520, 2008.

[136] Allen Taflove, Susan C Hagness, and Melinda Piket-May. Computational electromagnetics: the finite-difference time-domain method. *The Electrical Engineering Handbook*, 3(629-670):15, 2005.

[137] Shih-Hui Chang and Allen Taflove. Finite-difference time-domain model of lasing action in a four-level two-electron atomic system. *Optics express*, 12(16):3827–3833, 2004.

[138] Mehmet Fatih Yanik, Shanhui Fan, and Marin Soljačić. High-contrast all-optical bistable switching in photonic crystal microcavities. *Applied Physics Letters*, 83(14):2739–2741, 2003.

[139] Parag B Deotare, Murray W McCutcheon, Ian W Frank, Mughees Khan, and Marko Lončar. High quality factor photonic crystal nanobeam cavities. *Applied Physics Letters*, 94(12), 2009.

[140] Takuto Yamaguchi, Yasutomo Ota, Ryota Katsumi, Katsuyuki Watanabe, Satomi Ishida, Alto Osada, Yasuhiko Arakawa, and Satoshi Iwamoto. Gaas valley photonic crystal

waveguide with light-emitting inas quantum dots. *Applied Physics Express*, 12(6):062005, 2019.

[141] Matthew Pelton. Modified spontaneous emission in nanophotonic structures. *Nature Photonics*, 9(7):427–435, 2015.

[142] Katsuaki Tanabe, Masahiro Nomura, Denis Guimard, Satoshi Iwamoto, and Yasuhiko Arakawa. Room temperature continuous wave operation of inas/gaas quantum dot photonic crystal nanocavity laser on silicon substrate. *Optics express*, 17(9):7036–7042, 2009.

[143] Gunnar Bjork and Yoshihisa Yamamoto. Analysis of semiconductor microcavity lasers using rate equations. *IEEE Journal of Quantum Electronics*, 27(11):2386–2396, 1991.

[144] Zhili Yang, Matthew Pelton, Igor Fedin, Dmitri V Talapin, and Edo Waks. A room temperature continuous-wave nanolaser using colloidal quantum wells. *Nature communications*, 8(1):143, 2017.

[145] Sanfeng Wu, Sonia Buckley, John R Schaibley, Liefeng Feng, Jiaqiang Yan, David G Mandrus, Fariba Hatami, Wang Yao, Jelena Vučković, Arka Majumdar, et al. Monolayer semiconductor nanocavity lasers with ultralow thresholds. *nature*, 520(7545):69–72, 2015.

[146] Andy Brown, Amitabh Joshi, and Min Xiao. Controlled steady-state switching in optical bistability. *Applied physics letters*, 83(7):1301–1303, 2003.

[147] Takasumi Tanabe, Masaya Notomi, Satoshi Mitsugi, Akihiko Shinya, and Eiichi Kuramochi. Fast bistable all-optical switch and memory on a silicon photonic crystal on-chip. *Optics letters*, 30(19):2575–2577, 2005.

[148] Qianfan Xu and Michal Lipson. All-optical logic based on silicon micro-ring resonators. *Optics express*, 15(3):924–929, 2007.

[149] RM Fleming, CH Seager, DV Lang, E Bielejec, and JM Campbell. Defect-driven gain bistability in neutron damaged, silicon bipolar transistors. *Applied physics letters*, 90(17), 2007.

[150] Deepak Sridharan and Edo Waks. All-optical switch using quantum-dot saturable absorbers in a dbr microcavity. *IEEE Journal of Quantum Electronics*, 47(1):31–39, 2010.

[151] Yuqi Zhao, Hamidreza Chalabi, and Edo Waks. Low power threshold, ultrathin optical limiter based on a nonlinear zone plate. *Optics Express*, 29(21):33144–33154, 2021.

[152] Denis Guimard, Masao Nishioka, Shiro Tsukamoto, and Yasuhiko Arakawa. High density inas/ gaas quantum dots with enhanced photoluminescence intensity using antimony surfactant-mediated metal organic chemical vapor deposition. *Applied physics letters*, 89(18), 2006.

[153] H Fujita, K Yamamoto, J Ohta, Y Eguchi, and K Yamaguchi. In-plane quantum-dot superlattices of inas on gaassb/gaas (001) for intermediate band solar-cells. In *2011 37th IEEE Photovoltaic Specialists Conference*, pages 002612–002614. IEEE, 2011.

[154] CH Lin, HS Lin, CC Huang, SK Su, Sheng-Di Lin, Kien-Wen Sun, CP Lee, YK Liu, MD Yang, and JL Shen. Temperature dependence of time-resolved photoluminescence spectroscopy in inas/gaas quantum ring. *Applied Physics Letters*, 94(18), 2009.

[155] Paola Borri, W Langbein, Jesper Mørk, Jørn Märcher Hvam, F Heinrichsdorff, M-H Mao, and Dieter Bimberg. Dephasing in inas/gaas quantum dots. *Physical Review B*, 60(11):7784, 1999.

[156] Xiaolei Wang, Houqiang Jiang, Junxue Chen, Pei Wang, Yonghua Lu, and Hai Ming. Optical bistability effect in plasmonic racetrack resonator with high extinction ratio. *Optics express*, 19(20):19415–19421, 2011.

[157] R Bonifacio and LA Lugiato. Optical bistability and cooperative effects in resonance fluorescence. *Physical Review A*, 18(3):1129, 1978.

[158] Hyatt Gibbs. *Optical bistability: controlling light with light*. Elsevier, 2012.

[159] Laurent-Daniel Haret, Takasumi Tanabe, Eiichi Kuramochi, and Masaya Notomi. Extremely low power optical bistability in silicon demonstrated using 1d photonic crystal nanocavity. *Optics express*, 17(23):21108–21117, 2009.

[160] Masaya Notomi, Akihiko Shinya, Satoshi Mitsugi, Goh Kira, Eiichi Kuramochi, and Takasumi Tanabe. Optical bistable switching action of si high-q photonic-crystal nanocavities. *Optics express*, 13(7):2678–2687, 2005.

[161] Yong Zhang, Danping Li, Cheng Zeng, Yu Shi, Zengzhi Huang, Jinzhong Yu, and Jinsong Xia. Ultralow power nonlinear response in an si photonic crystal nanocavity. *IEEE Photonics Journal*, 5(4):6601409–6601409, 2013.

[162] Vilson R Almeida and Michal Lipson. Optical bistability on a silicon chip. *Optics letters*, 29(20):2387–2389, 2004.

[163] Peng Sun and Ronald M Reano. Low-power optical bistability in a free-standing silicon ring resonator. *Optics letters*, 35(8):1124–1126, 2010.

[164] Je-Hyung Kim, Shahriar Aghaeimeibodi, Jacques Carolan, Dirk Englund, and Edo Waks. Hybrid integration methods for on-chip quantum photonics. *Optica*, 7(4):291–308, 2020.

[165] Jongseung Yoon, Sung-Min Lee, Dongseok Kang, Matthew A Meitl, Christopher A Bower, and John A Rogers. Heterogeneously integrated optoelectronic devices enabled by micro-transfer printing. *Advanced Optical Materials*, 3(10):1313–1335, 2015.

[166] Mohammad Habibur Rahaman, Samuel Harper, Chang-Min Lee, Kyu-Young Kim, Mustafa Atabey Buyukkaya, Victor J Patel, Samuel D Hawkins, Je-Hyung Kim, Sadhvikas Addamane, and Edo Waks. Efficient, indistinguishable telecom c-band photons using a tapered nanobeam. *arXiv preprint arXiv:2404.01562*, 2024.

[167] Mohammad Habibur Rahaman, Chang-Min Lee, Mustafa Atabey Buyukkaya, Samuel Harper, Fariba Islam, and Edo Waks. Quality factor enhancement of inp nanobeam cavities using atomic layer deposition. In *Photonic and Phononic Properties of Engineered Nanostructures XIV*, volume 12896, pages 67–68. SPIE, 2024.

[168] Habibur Rahaman, Chang-Min Lee, Mustafa Atabey Buyukkaya, Yuqi Zhao, and Edo Waks. Low threshold lasing based on a hybrid si/iii-v cavity with quantum dots. In *CLEO: Applications and Technology*, pages ATu3R–5. Optica Publishing Group, 2023.

[169] S Kiravittaya, HS Lee, L Balet, LH Li, M Francardi, A Gerardino, A Fiore, A Rastelli, and OG Schmidt. Tuning optical modes in slab photonic crystal by atomic layer deposition and laser-assisted oxidation. *Journal of Applied Physics*, 109(5), 2011.

[170] Dirk Englund, David Fattal, Edo Waks, Glenn Solomon, Bingyang Zhang, Toshihiro Nakaoka, Yasuhiko Arakawa, Yoshihisa Yamamoto, and Jelena Vučković. Controlling the spontaneous emission rate of single quantum dots in a two-dimensional photonic crystal. *Physical review letters*, 95(1):013904, 2005.

[171] ” (n.d.). “Lumerical Inc. (see example “pump probe simulation using 4-level 2-electron material”).